

# Characterizing the Fast Radio Burst Population with the CHIME Telescope

Pragya Chawla

McGill Space Institute & Department of Physics  
McGill University  
Montreal, Quebec, Canada

December 15, 2021

A thesis submitted to McGill University in partial fulfilment of the  
requirements of the degree of Doctor of Philosophy

©2021 Pragya Chawla

# Abstract

Fast radio bursts (FRBs) are millisecond-duration radio transients of unknown origin. As these bursts are detectable at cosmological distances, they can be used to study the ionized plasma in the intergalactic medium. In order to harness the potential of FRBs as cosmological probes, it is important to develop a detailed understanding of the FRB population. This thesis aims to further our current understanding of two distinct aspects of the population, namely, source environments and activity levels, using the results of the CHIME/FRB project.

The Canadian Hydrogen Intensity Mapping Experiment (CHIME) is a transit telescope operating in the frequency range of 400-800 MHz. The CHIME/FRB project searches for FRBs in real time over the instantaneous field of view of CHIME ( $\sim 250$  sq. deg.). As the telescope observes the full northern sky every day, the FRB detection pipeline can both discover new sources and monitor the ones which are known to repeat. The first CHIME/FRB catalog consists of 474 non-repeating sources and 61 bursts from 18 repeating sources. These bursts are well suited for population studies as they have been detected with a uniform selection function.

We present algorithms to determine the on-sky exposure and sensitivity variations for the CHIME/FRB system. Using these algorithms, we generate full-sky maps of the total exposure during periods of nominal sensitivity. The estimated exposure can be used to characterize activity levels for known FRB sources. We demonstrate this using a study which uses the exposure information to validate the discovery of a periodic modulation in the activity of the repeating FRB source, FRB 20180916B.

---

We then present a multi-band observation campaign of FRB 20180916B with the CHIME/FRB system, the Green Bank telescope (GBT) and the Low Frequency Array (LOFAR). We report on the detection of seven bursts in the frequency range of 300-400 MHz with the GBT. Knowing that the circumburst environment is optically thin to free-free absorption at 300 MHz, we find evidence against the association of a hyper-compact HII region or a young supernova remnant with the source. We also characterize the frequency dependence of burst activity and place constraints on the scattering properties of the source environment.

Finally, we report on a Monte-Carlo based population synthesis study of two propagation effects, namely, dispersion and scattering, in the first CHIME/FRB catalog. We simulate intrinsic properties and propagation effects for a variety of FRB population models and compare the simulated distributions of dispersion measures and scattering timescales with the corresponding distributions from the CHIME/FRB catalog. Our simulations confirm the results of previous studies which suggested that the interstellar medium of the host galaxy alone cannot explain the observed scattering timescales of FRBs. We conclude that either FRBs inhabit environments with more extreme scattering properties than those inferred for Galactic pulsars, or that the circumgalactic media of intervening galaxies is a source of intense scattering.

# Résumé

Les sursauts radio rapides (FRBs, de l'anglais fast radio bursts) sont des événements transitoires qui ne durent que quelques millisecondes et dont l'origine est inconnue. Les FRBs sont si brillants qu'ils sont détectés à des distances cosmologiques, et ainsi ils peuvent être utilisés pour étudier le plasma ionisé dans le milieu intergalactique. Pour bénéficier du potentiel des FRBs comme sondes cosmologiques, il est important d'acquérir une compréhension approfondie et détaillée de la population qu'ils représentent. Se basant sur les découvertes faites par le projet CHIME/FRB, cette thèse vise à approfondir nos connaissances en ce qui concerne deux aspects distincts de la population, soit l'environnement des sources de FRBs et leurs niveaux d'activités.

L'Expérience canadienne de cartographie de l'intensité de l'hydrogène (CHIME, de l'anglais Canadian Hydrogen Intensity Mapping Experiment) est un télescope stationnaire qui observe dans la gamme de fréquences 400-800 MHz. Le projet CHIME/FRB cherche en temps réel des sursauts dans le champ de vision instantané de CHIME ( $\sim 250$  degrés carrés). Puisque le télescope observe l'intégralité du ciel nordique à tous les jours, le pipeline de détection de FRBs peut à la fois découvrir de nouvelles sources et surveiller celles produisant des sursauts de façon répétitive. Le premier catalogue de CHIME/FRB comprend 474 sources n'ayant émis qu'un seul sursaut ponctuel (sources non-répétitives) et 61 sursauts provenant de 18 sources répétitives. Ces FRBs conviennent très bien aux études de population puisqu'ils ont été détectés par un système de sélection uniforme.

Nous présentons des algorithmes développés dans le but de déterminer le niveau d'exposition du ciel et les variations en sensibilité du système CHIME/FRB. À l'aide de ces

algorithmes, nous produisons des cartes du ciel pour l'exposition totale pendant les périodes de sensibilité nominale. Les valeurs estimées d'exposition peuvent ensuite être utilisées pour caractériser le niveau d'activité des sources connues de FRBs, ce que nous démontrons par l'entremise d'une étude où l'exposition est utilisée pour valider la découverte d'une modulation périodique dans le niveau d'activité de la source répétitive FRB 20180916B.

Ensuite, nous présentons les résultats d'une campagne d'observations multispectrales avec le système CHIME/FRB, le Green Bank Telescope (GBT), et le Low Frequency Array (LOFAR). Dans cette thèse, nous faisons rapport sur sept sursauts détectés avec le GBT dans la bande de fréquences 300 à 400 MHz. Cette détection nous indique que l'environnement local de la source est transparent à l'absorption libre-libre à une fréquence de 300 MHz. Par conséquent, nos résultats démontrent que cette source n'est pas associée à une région H II hyper compacte, ni avec un jeune rémanent de supernova. Nous caractérisons la dépendance spectrale de l'activité de la source et établissons des limites quant aux propriétés de diffusion de l'environnement.

En terminant, nous présentons une synthèse de population basée sur une méthode Monte-Carlo et réalisée avec les FRBs constituant le premier catalogue de CHIME/FRB. Cette synthèse vise spécifiquement l'étude de deux effets de propagations de l'émission radio des FRBs: la dispersion et la diffusion des ondes. Nous simulons les propriétés intrinsèques et les effets de propagations pour divers modèles de population de FRBs et comparons les distributions des mesures de dispersion et des temps de diffusion simulés à celles observées dans le catalogue de CHIME/FRB. Confirmant les résultats d'études précédentes, nos simulations suggèrent que le milieu interstellaire dans les galaxies hôtes ne peut être l'unique contributeur de la diffusion des ondes que l'on observe chez les FRBs. Nous concluons donc que les environnements locaux des sources de FRBs sont propices à des conditions de diffusion plus extrêmes que ceux des pulsars galactiques, ou bien que les milieux intergalactiques dans lesquels les FRBs se propagent sont de fortes sources de

diffusion.

## Acknowledgements

First and foremost, I thank my supervisor, Vicky Kaspi, for her support, encouragement and guidance over the past several years. In working with her, I have learned how to think critically and creatively and for that I am truly grateful.

I thank members of the CHIME/FRB collaboration for providing many constructive comments which have greatly improved the analyses presented in this thesis. I am especially thankful to Chitrang Patel, Shiny Brar and Davor Cubranic for answering my many questions about the technical aspects of the CHIME/FRB system. Thanks also go out to my fellow graduate students, Alex Josephy, Ziggy Pleunis, Bridget Andersen and Marcus Merryfield, for helping me navigate the labyrinth that the CHIME/FRB project was in its initial years. I have greatly enjoyed our many conversations and brainstorming sessions. I also thank Emmanuel Fonseca and Shriharsh Tendulkar for their advice, both scientific and professional, throughout my time as a graduate student.

I would like to acknowledge the financial support of the Fonds de recherche du Québec and the Mitacs Globalink program. I also thank Locke Spencer for taking me on as a Mitacs Globalink intern during my undergraduate years. That opportunity opened many doors for me, for which I am truly thankful.

I am grateful to Matt Dobbs and David Hanna for being a part of my supervisory committee and keeping in touch with my research over the past four years. I also thank Émilie Parent for translating my thesis abstract.

The past four years have been a challenging time for me and friends, both in Montréal and beyond, have been a constant source of support. I am especially thankful to Shruti,

Shreya, Bryce, Émilie and Shalu, for helping me navigate difficult situations and uplifting my spirits. Finally, I thank my family for cheering me on from the other side of the world. Mumma and Deedee, this would not have been possible without you.

# Preface

## Contribution to Original Knowledge and Contribution of Authors

Chapter 1 summarizes the literature on fast radio bursts that is relevant for this thesis. Chapter 2 describes the CHIME telescope and the CHIME/FRB system. Being a member of the CHIME/FRB collaboration, I helped with the construction of the telescope, particularly the assembly and the installation of the computing nodes. I was also responsible for monitoring the data quality for the CHIME/FRB system.

The rest of the chapters report on original results regarding the local environments and activity levels of FRBs. The author contributions for these chapters are described below.

- **Chapter 3 – Determining the Sky Exposure for the CHIME/FRB System**

This chapter presents the algorithms developed to evaluate the exposure and sensitivity variations for the CHIME/FRB system. I developed and implemented these algorithms, based on discussions with members of the CHIME/FRB collaboration. The algorithm for characterizing the sensitivity variations was first presented in [Josephy et al. \(2019\)](#).

These algorithms utilize two Python scripts developed by other members of the collaboration. These scripts query the database for beam metrics and properties of single pulses from Galactic pulsars. The scripts were written by Dr. Shriharsh Tendulkar and Dr. Ziggy Pleunis, respectively.

I have used the techniques presented in this chapter to determine the exposure and repetition rate for CHIME-detected FRBs. The results have been presented in several

published papers. To illustrate the use of these techniques, results from two of these papers are included in this chapter:

- CHIME/FRB Collaboration, Amiri, M., Andersen, B. C., et al. 2020, Periodic activity from a fast radio burst source, *Nature*, 582, 351
- CHIME/FRB Collaboration, Amiri, M., Andersen, B. C., et al. 2021, The First CHIME/FRB Fast Radio Burst Catalog, arXiv e-prints, arXiv:2106.04352 (Submitted to the *Astrophysical Journal Supplement Series*)

- **Chapter 4 – Detection of FRB 180916.J0158+65 Down to Frequencies of 300 MHz**

This chapter reports on observations of FRB 180916.J0158+65 with CHIME, GBT and LOFAR. The contents of this chapter originally appeared in the following paper published in the *Astrophysical Journal Letters*:

**Chawla, P.**, Andersen, B. C., Bhardwaj, M., Fonseca, E., Josephy, A., Kaspi, V. M., Michilli, D., Pleunis, Z., Bandura, K. M., Bassa, C. G., Boyle, P. J., Brar, C., Cassanelli, T., Cubranic, D., Dobbs, M., Dong, F. Q., Gaensler, B. M., Good, D. C., Hessels, J. W. T., Landecker, T. L., Leung, C., Li, D. Z., Lin, H.-H., Masui, K., Mckinven, R., Mena-Parra, J., Merryfield, M., Meyers, B. W., Naidu, A., Ng, C., Patel, C., Rafiei-Ravandi, M., Rahman, M., Sanghavi, P., Scholz, P., Shin, K., Smith, K. M., Stairs, I. H., Tendulkar, S. P., & Vanderlinde, K. 2020, Detection of Repeating FRB 180916.J0158+65 Down to Frequencies of 300 MHz, *The Astrophysical Journal Letters*, 896, L41

The author contributions are as follows. I proposed for, conducted and analyzed the GBT observations, with assistance from Dr. Victoria Kaspi, Dr. Emmanuel Fonseca and Dr. Daniele Michilli. Dr. Ziggy Pleunis proposed for and analyzed the LOFAR observations, with assistance from Dr. Jason Hessels and Dr. Cees Bassa. Dr. Pleunis also performed the analysis to determine the drift rate for one of the GBT

bursts and wrote the text in §4.2.3 and §4.3.2. Dr. Fonseca determined the burst widths and scattering timescales and contributed to the text in §4.3.1. Dr. Michilli determined the polarization properties of the bursts and authored the text in §4.3.3. Bridget Andersen performed the Fourier domain acceleration search for rotational periodicity and contributed to the text in §4.3.4. Alexander Josephy determined the fluence completeness thresholds and wrote the text in §4.3.5. Mohit Bhardwaj derived the constraints on the proposed models of FRBs and authored the text in §4.4.4.

I performed all the other analysis and wrote the rest of the manuscript. Dr. Kaspi contributed significantly to the interpretation of the results and provided guidance throughout the research and writing process. All other co-authors are members of the CHIME/FRB collaboration who provided feedback on the analysis and the paper draft.

- **Chapter 5 – Modelling Dispersion and Scattering in the First CHIME/FRB Catalog**

This chapter reports on a population synthesis study of dispersion and scattering in the first CHIME/FRB catalog. The contents of this chapter are part of a manuscript which has been submitted to the *Astrophysical Journal*:

**Chawla, P.**, Kaspi, V. M., Ransom, S. M., Bhardwaj, M., Boyle, P. J., Breitman, D., Cassanelli, T., Cubranic, D., Dong, F. Q., Fonseca, E., Gaensler, B. M., Giri, U., Josephy, A., Kaczmarek, J. F., Leung, C., Masui, K. W., Mena-Parra, J., Merryfield, M., Michilli, D., Münchmeyer, M., Ng, C., Patel, C., Pearlman, A. B., Petroff, E., Pleunis, Z., Rahman, M., Sanghavi, P., Shin, K., Smith, K. M., Stairs, I., & Tendulkar, S. P. 2021, Modeling Fast Radio Burst Dispersion and Scattering Properties in the First CHIME/FRB Catalog, arXiv e-prints, arXiv:2107.10858

I performed all of the analyses presented in this work and authored the manuscript.

---

The population synthesis simulations were designed based on discussions with Dr. Victoria Kaspi, Dr. Scott Ransom and members of the CHIME/FRB dispersion working group. The rest of the co-authors provided feedback on the intermediate results and the manuscript. Moreover, the analyses in this paper is based on the burst parameters reported in the first CHIME/FRB catalog. All co-authors are members of the CHIME/FRB collaboration who were involved in the effort to determine the parameters.

---

# Contents

<b>1</b>	<b>Introduction</b>	<b>1</b>
1.1	A Brief History . . . . .	2
1.2	Propagation Effects . . . . .	4
1.2.1	Dispersion . . . . .	4
1.2.2	Scattering . . . . .	6
1.2.3	Faraday Rotation . . . . .	9
1.3	Intrinsic Properties . . . . .	10
1.3.1	Brightness . . . . .	10
1.3.2	Spectro-Temporal & Polarimetric Properties . . . . .	11
1.3.3	Ensemble Spectrum . . . . .	12
1.3.4	Repetition and Periodicity . . . . .	14
1.3.5	Host Galaxies & Local Environments . . . . .	15
1.4	Progenitor Models . . . . .	16
1.4.1	Isolated Neutron Stars . . . . .	17
1.4.2	Compact Object Mergers . . . . .	18
1.4.3	Other Models . . . . .	19
1.5	Outline of Thesis . . . . .	20
<b>2</b>	<b>The CHIME/FRB Project</b>	<b>21</b>
2.1	The CHIME Telescope . . . . .	23
2.1.1	Science Goals . . . . .	24

---

2.1.2	Analog Signal Chain . . . . .	25
2.1.3	Correlator . . . . .	26
2.1.4	Beam-forming . . . . .	26
2.1.5	Up-channelization . . . . .	28
2.2	CHIME/FRB Detection Pipeline . . . . .	29
2.2.1	L1: Dedispersion and Event Identification . . . . .	30
2.2.2	L2/L3: Multi-beam Grouping and Event Classification . . . . .	33
2.2.3	L4: Action Implementation and Event Archiving . . . . .	35
2.2.4	Synthetic Signal Injection . . . . .	36
2.3	The First CHIME/FRB Catalog . . . . .	37
<b>3</b>	<b>Determining the Sky Exposure for the CHIME/FRB System</b>	<b>40</b>
3.1	Exposure Definition . . . . .	41
3.2	Pipeline Metrics . . . . .	43
3.3	Sensitivity Variations . . . . .	45
3.3.1	Criteria for Pulsar Selection . . . . .	46
3.3.2	Estimation of RMS Noise . . . . .	47
3.3.3	Excision of Low Sensitivity Periods . . . . .	50
3.4	Full-sky Exposure Maps . . . . .	51
3.5	Source Exposures . . . . .	53
3.6	FRB Repetition Rates . . . . .	57
3.6.1	FRB 20180916B . . . . .	57
<b>4</b>	<b>Detection of FRB 180916.J0158+65 Down to Frequencies of 300 MHz</b>	<b>61</b>
4.1	Introduction . . . . .	61
4.2	Observations . . . . .	63
4.2.1	Green Bank Telescope . . . . .	63
4.2.2	CHIME/FRB Instrument . . . . .	65

---

4.2.3	Low-Frequency Array (LOFAR) . . . . .	67
4.3	Analysis . . . . .	68
4.3.1	Determination of Burst Properties . . . . .	68
4.3.2	Drift Rate Measurement for Burst 191219C . . . . .	71
4.3.3	Polarization Properties . . . . .	73
4.3.4	Periodicity Search . . . . .	76
4.3.5	Determination of System Sensitivity . . . . .	77
4.4	Discussion . . . . .	80
4.4.1	Scattering Times . . . . .	81
4.4.2	Phase Dependence of Source Activity . . . . .	82
4.4.3	Frequency Dependence of Source Activity . . . . .	82
4.4.4	Constraints on Proposed Models . . . . .	85
4.5	Conclusions . . . . .	87
<b>5</b>	<b>Modelling Dispersion and Scattering in the First CHIME/FRB Catalog</b>	<b>89</b>
5.1	Introduction . . . . .	89
5.2	Observations . . . . .	91
5.3	Modelling Intrinsic Properties . . . . .	93
5.3.1	Redshift . . . . .	93
5.3.2	Energy . . . . .	95
5.3.3	Sky Location . . . . .	97
5.4	Modelling Propagation Effects . . . . .	98
5.4.1	Milky Way . . . . .	101
5.4.2	Intergalactic Medium . . . . .	101
5.4.3	Host Galaxy . . . . .	102
5.4.4	Circumburst Environment . . . . .	108
5.4.5	Intervening Galaxies . . . . .	109
5.5	Simulation Procedure . . . . .	111

---

5.6	Results and Discussion . . . . .	114
5.6.1	Varying Assumed Parameters . . . . .	116
5.6.2	Circumburst Environment . . . . .	120
5.6.3	Intervening Galaxies . . . . .	121
5.6.4	Host Galaxies . . . . .	123
5.6.5	Progenitor Models . . . . .	125
5.7	Summary and Conclusions . . . . .	127
<b>6</b>	<b>Conclusions</b>	<b>129</b>

# List of Figures

1.1	Dynamic spectrum of the first FRB detection . . . . .	3
1.2	Dynamic spectrum of a scatter-broadened pulse from FRB 20110220A . . . . .	7
1.3	Distribution of FRB fluences and extragalactic dispersion measures . . . . .	11
2.1	The Green Bank telescope . . . . .	22
2.2	The CHIME telescope . . . . .	24
2.3	Sky positions of CHIME/FRB synthesized beams . . . . .	28
2.4	Schematic of the CHIME/FRB detection pipeline . . . . .	30
2.5	Sky distribution for the first CHIME/FRB catalog . . . . .	37
2.6	Dynamic spectra for FRBs in the first CHIME/FRB catalog . . . . .	38
3.1	Exposure as a function of distance from the beam centre . . . . .	42
3.2	Primary beam response and transit paths for circumpolar sources . . . . .	44
3.3	Daily variation in the RMS noise for the CHIME/FRB system . . . . .	50
3.4	Sky area in celestial coordinates observed by the synthesized beams . . . . .	52
3.5	Full-sky exposure maps for the first CHIME/FRB catalog . . . . .	54
3.6	Localization region and exposure timeline for FRB 20180923C . . . . .	55
3.7	Source exposures in the first CHIME/FRB catalog . . . . .	56
3.8	Timeline of CHIME/FRB's daily exposure to FRB 20180916B . . . . .	58
4.1	Exposure of LOFAR, GBT and CHIME/FRB to FRB 20180916B . . . . .	64
4.2	Dynamic spectra of bursts from FRB 20180916B detected with the GBT . . . . .	70

---

4.3	Polarization properties of the GBT-detected bursts from FRB 20180916B . . .	75
4.4	Burst fluences and completeness limits for LOFAR, GBT, and CHIME/FRB	78
5.1	Probability density function of source redshift for different population models	94
5.2	Inferred isotropic-equivalent energy for Catalog 1 events . . . . .	96
5.3	Probability density function for simulated burst declinations . . . . .	98
5.4	Simulated DMs and scattering times for different host galaxy types . . . . .	104
5.5	Simulated DMs and scattering measures for local environments . . . . .	110
5.6	Simulated DMs and scattering times for the favoured population model . . .	117
5.7	CDF of the scattering time distribution for Catalog 1 and the favoured model	118
5.8	Contribution of different media to the simulated DMs and scattering times .	119
5.9	Scattering time distribution for population models with Milky Way and host galaxy ISM as dominant scattering sources . . . . .	120
5.10	CDF of simulated DMs and scattering times for a short GRB-like spatial distribution . . . . .	122
5.11	CDF of simulated DMs and scattering times for different progenitor models .	126

# Chapter 1

## Introduction

Fast radio bursts (FRBs) are astrophysical transients which were serendipitously discovered in 2007 and have been the subject of extensive study ever since. They are radio pulses of  $\mu\text{s}$  to ms duration, which are dispersed as they propagate through cold, ionized plasma. The level of dispersion observed for FRBs greatly exceeds that expected from the Milky Way implying that these bursts originate outside the Galaxy. Identification of host galaxies for several FRBs has confirmed this inference and established that these bursts are occurring at cosmological distances.

The estimated all-sky FRB rate is  $\sim 10^3$  per day above the sensitivity threshold of existing radio telescopes (see, e.g., [Lawrence et al. 2017](#); [Bhandari et al. 2018](#)). The origin of such a large population of bursts is still a mystery and dozens of theoretical models have been proposed to explain their emission (see §1.4). Even without knowledge of their progenitors, the ubiquity of these bursts has enabled their use as probes of magnetized plasma in the intergalactic medium (see [Cordes & Chatterjee 2019](#); [Petroff et al. 2019](#) for recent reviews). Additionally, FRBs have the potential to probe large scale structure and constrain cosmological parameters once a large sample ( $\sim 10000$  bursts) is detected (see, e.g., [Macquart et al. 2015](#); [Masui & Sigurdson 2015](#); [Walters et al. 2018](#)). In order to harness the potential of FRBs as cosmological probes, it is important to develop a detailed understanding of the FRB population. Research efforts over the past decade and a half

aimed in this direction are summarized in the following section.

## 1.1 A Brief History

Dedicated searches for millisecond pulses at radio frequencies started in the years following the discovery of pulsars by Jocelyn Bell Burnell in 1967 (Hewish et al., 1968). Pulsars are highly magnetized, rapidly rotating neutron stars that emit beamed pulses of electromagnetic radiation at regular intervals. As the emission beam of the neutron star sweeps across our line of sight once per rotation, the pulsed emission is modulated at the rotation period of the star. About three thousand pulsars have been detected in our Galaxy with spin periods ranging from 1.4 ms to tens of seconds<sup>1</sup> (Manchester et al., 2005).

Radio pulsars can be detected above the noise level of a telescope by integrating the signal from consecutive faint pulses. Alternately, they can be detected by the emission of a single pulse which is significantly brighter than the average. In order to detect a pulsar using either of these techniques, it is generally necessary to account for dispersion. Dispersion is a frequency-dependent delay caused by the interstellar medium (ISM) and characterized by the dispersion measure (DM). The DM is the integrated column density of free electrons along the line of sight in the intervening medium and is described in detail in §1.2.1. Since the DM for a pulsar is not known a priori, searches are conducted at different trial DMs. Prior to the discovery of the first FRB, most pulsar surveys limited the range of trial DMs to the maximum expected for the Milky Way.

The first FRB was discovered in a search for single pulses from pulsars in the Magellanic Clouds using the 64-m diameter Parkes radio telescope (Lorimer et al., 2007). While the maximum DM expected from the Milky Way along the line of sight to this FRB was 25 pc cm<sup>-3</sup>, the search was conducted up to a DM of 500 pc cm<sup>-3</sup>. The burst, shown in Figure 1.1, was detected at a DM of 375 pc cm<sup>-3</sup>. Exploring the parameter space for dispersion resulted in the discovery of this FRB as well as the subsequent detection of five FRBs in other pulsar

---

<sup>1</sup><https://www.atnf.csiro.au/research/pulsar/psrcat/>; accessed in November 2021

surveys conducted with the Parkes telescope (Keane et al., 2012; Thornton et al., 2013).

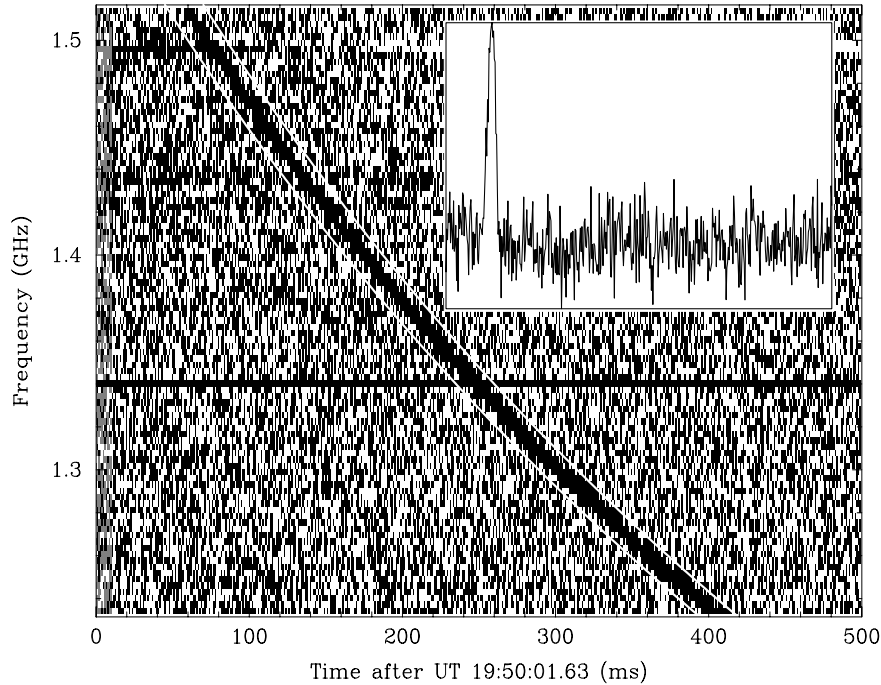


**Figure 1.1:** Dynamic spectrum of the first FRB detection (FRB 20010724A) showing intensity as a function of frequency and time. The burst is dispersed with the higher frequency radio waves arriving earlier than their low-frequency counterparts due to propagation in cold, ionized plasma. The white curves bracketing the pulse show the expected delay for a DM of  $375 \text{ pc cm}^{-3}$ . The inset shows the time series obtained after correcting for the dispersive delay and summing the signal in all frequency channels. Figure from Lorimer et al. (2007).

Despite detection of these five FRBs, there was some skepticism regarding the celestial nature of this phenomenon. Since all the sources were detected with the same telescope, there were concerns that FRBs were a source of terrestrial radio interference (Kulkarni et al., 2014). However, subsequent detections with the Arecibo telescope and the Green Bank telescope confirmed the astronomical origin of these bursts (Spitler et al., 2014; Masui et al., 2015). The FRB discovered with the Arecibo telescope, FRB 20121102A, was the first source which was observed to repeat (Spitler et al., 2016). The repetition enabled follow-up observations of the source which resulted in sub-arcsecond localization and identification of the host galaxy. The host galaxy was observed to have a redshift of  $z = 0.19$  confirming that FRBs are located at cosmological distances (Chatterjee et al., 2017; Tendulkar et al., 2017).

In the decade following the discovery of the first FRB, 30 more sources were discovered. The low detection rate was primarily due to the relatively small field-of-view (FOV) of the radio telescopes operational at the time. However, the detection rate has greatly increased in recent years as several telescopes with a larger FOV and dedicated time for FRB searches have come online. These include the Australian SKA Pathfinder (ASKAP; [Macquart et al. 2010](#)), the UTMOST instrument on the Molonglo telescope ([Caleb et al., 2016](#)) and the Canadian Hydrogen Intensity Mapping Experiment telescope (CHIME; see Chapter 2). A total of 612 FRB sources have been detected to date<sup>2</sup>. The following sections summarize our current understanding of the intrinsic properties and propagation effects observed for the known FRB population.

## 1.2 Propagation Effects

As an FRB signal traverses the circumburst medium, the ISM of the host galaxy, the intergalactic medium and the Milky Way ISM, the signal properties could change due to interactions with intervening plasma. It is essential to study these propagation effects in order to infer the intrinsic properties of FRBs. Additionally, such studies are of paramount importance in enabling the use of FRBs as probes of intervening plasma. The three major propagation effects, namely, dispersion, scattering and Faraday rotation, are presented in the following subsections. The effects are described in detail in [Lorimer & Kramer \(2004\)](#).

### 1.2.1 Dispersion

As previously described in §1.1, dispersion is the phenomenon by which high frequency radio waves propagating through cold, ionized plasma are detected earlier than their low-frequency counterparts. The delay, illustrated in Figure 1.1, can be attributed to the

---

<sup>2</sup><https://www.wis-tns.org>; accessed in November 2021

frequency-dependent refractive index of the plasma,

$$\mu = \sqrt{1 - \left(\frac{\nu_p}{\nu}\right)^2}. \quad (1.1)$$

Here  $\nu$  is the frequency of the radio waves and the plasma frequency is,

$$\nu_p = \sqrt{\frac{e^2 n_e}{\pi m_e}}, \quad (1.2)$$

where  $n_e$  is the electron number density and  $e$  and  $m_e$  are the charge and mass of the electron, respectively. The frequency dependence of  $\mu$  causes the group velocity,  $v_g = \mu c$ , to vary with frequency. This introduces a delay with respect to a signal at infinite frequency,

$$t_{\text{DM}} = \frac{e^2}{2\pi m_e c} \frac{\int_0^d n_e dl}{\nu^2}, \quad (1.3)$$

where  $d$  is the distance to the FRB and the integral of the free electron density along the line of sight is the DM in units of  $\text{pc cm}^{-3}$ . A pulse with a given DM would exhibit a total delay over the telescope bandwidth of

$$\Delta t_{\text{DM}} \sim 4.15 \times 10^6 \text{ms} \times \text{DM} \times (\nu_{\text{low}}^{-2} - \nu_{\text{high}}^{-2}), \quad (1.4)$$

where  $\nu_{\text{low}}$  and  $\nu_{\text{high}}$  are the lowest and highest observing frequencies expressed in MHz. It is necessary to correct for this delay in order to detect a pulse in the time series obtained by integrating over all observing frequencies. This process is called dedispersion and is described in Chapter 2.

Although dispersion makes searching for FRBs computationally intensive, it permits estimation of FRB distances. The DM of an FRB includes contribution from all intervening

media that FRB signals propagate through, as shown by the following equation,

$$DM_{\text{FRB}} = DM_{\text{MW}} + DM_{\text{IGM}}(z) + \frac{DM_{\text{Host}}}{(1+z)} + \frac{DM_{\text{Local}}}{(1+z)}, \quad (1.5)$$

where ‘MW’, ‘IGM’, ‘Host’ and ‘Local’ stand for the Milky Way, the intergalactic medium, the host galaxy and the local environment of the FRB source, respectively. The factor of  $(1+z)$  scales the rest-frame DM contribution of the host galaxy and the local environment to the observer’s frame of reference (Ioka, 2003). The DM contribution of the Milky Way along any line of sight can be ascertained using models of electron density in the Galaxy (Cordes & Lazio, 2002; Yao et al., 2017). These models are calibrated using Galactic pulsars with precise distance measurements. Although the contribution of the host galaxy and the local environment is uncertain, the maximum possible redshift can be estimated for any FRB source by attributing the DM in excess of the Galactic contribution to the IGM. This estimate is based on the Macquart relation, which relates  $DM_{\text{IGM}}$  to source redshift ( $DM_{\text{IGM}} \sim 900z \text{ pc cm}^{-3}$ ). While the relation was initially derived theoretically assuming a fully ionized and homogeneous IGM (Ioka, 2003; Inoue, 2004), it has now been observationally constrained using FRBs with independent redshift measurements (Macquart et al., 2020).

FRBs with measured redshifts can also be used to estimate the DM for the host galaxy using Equation 1.5. Host DMs have been constrained to be  $< 200 \text{ pc cm}^{-3}$  for the 14 localized FRBs (Heintz et al. 2020 and references therein). The constraint reported here includes contributions from the interstellar medium and halo of the host galaxy and the local environment of the FRB source. The expected contribution of each of these media will be discussed in Chapter 5.

### 1.2.2 Scattering

FRB pulse profiles exhibit exponential tails, as shown in Figure 1.2, due to a phenomenon called scattering which is also observed in Galactic pulsars. Rays from an FRB are scattered

by inhomogeneities in the intervening medium and thus have slightly different path lengths. They arrive at different times at the telescope resulting in the broadening of an intrinsically sharp pulse. The amount of scattering is parameterized by the time constant,  $\tau$ , of a one-sided exponential function fit to the pulse.

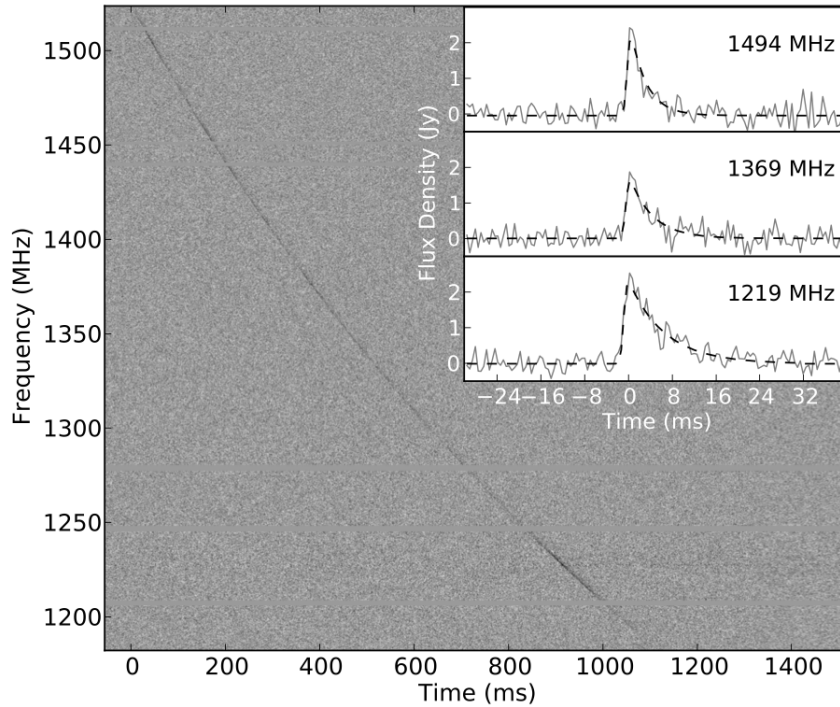


**Figure 1.2:** Dynamic spectrum of FRB 20110220A showing the dispersed pulse. The inset shows the dedispersed time series at different frequencies. The pulse exhibits a scattering tail which becomes broader at lower frequencies. The best-fit model to each time series (shown by the black dashed curve) corresponds to an exponential function, the timescale for which has a power-law index of  $-4$  for the frequency dependence. Figure from [Thornton et al. \(2013\)](#).

The observation of scattering can be explained using the model proposed by [Scheuer \(1968\)](#). In the model, turbulent plasma causing the scattering is assumed to be concentrated in a thin screen midway between the Earth and the source instead of being spread along the entire propagation path. The model predicts that the scattering timescale,  $\tau$ , increases at lower frequencies and is proportional to  $\nu^{-4}$ . The inferred value of the power-law index for FRBs with measured scattering times<sup>3</sup> is consistent with  $-4$  ([Petroff et al., 2016](#)). This

<sup>3</sup><https://frbcat.org>; accessed in November 2021

frequency dependence implies that FRBs with large scattering times are harder to detect at low frequencies as temporal broadening dilutes the signal.

About 30% of FRBs exhibit measurable scattering i.e. the scattering time is greater than the intrinsic pulse width (Cordes & Chatterjee, 2019). Most of these FRBs have scattering times greater than the Galactic expectation along the line of sight. While the IGM contributes significantly to FRB DMs, theoretical models suggest that it is not a significant source of FRB scattering (Macquart & Koay, 2013). The present lack of an observed correlation between FRB DMs and scattering times also suggests that the IGM does not significantly contribute to both the quantities (Katz, 2016a; Cordes et al., 2016; Qiu et al., 2020).

This leaves the host galaxy and/or the local environment of the FRB as being the dominant sources of scattering. The local environment is mildly favoured due to the observation of high scattering times for a few FRBs located in the outskirts of their host galaxies where the ISM is not expected to be very turbulent (Day et al., 2020). Alternately, Vedantham & Phinney (2019) have proposed that scattering could originate in the circumgalactic media of intervening galaxies. The origin of FRB scattering is explored in greater detail in Chapter 5.

A closely related phenomenon to scattering is scintillation, which was first observed for Galactic pulsars by Lyne & Rickett (1968) and is similar to optical ‘twinkling’ of stars due to turbulence in the Earth’s atmosphere. FRBs can scintillate since they are perceived as point sources by an observer on Earth due to their cosmological distances. Scintillation is caused by inhomogeneities in the intervening medium modulating the phase of radio waves emitted by an FRB. Signals with different phases form an interference pattern at the location of the observer, causing the intensity of FRB emission to fluctuate at different timescales and bandwidths. The thin screen model of the ISM proposed by Scheuer (1968) stipulates that the intensity fluctuations are correlated over a bandwidth  $\Delta\nu_d \propto \nu^4$ , which is referred to as the scintillation bandwidth. The scintillation bandwidth has been measured for a few FRBs

(see, e.g., Masui et al. 2015; Marcote et al. 2020) and has been found to be consistent with the Galactic expectation along the line of sight. These observations have also constrained the Galactic contribution to FRB scattering as  $\tau \sim 1/\Delta\nu_d$ .

### 1.2.3 Faraday Rotation

An FRB signal also interacts with the intervening magnetized plasma. The component of the magnetic field parallel to the direction of wave propagation ( $B_{\parallel}$ ) causes the left and right-hand circularly polarized radio waves to have different phase velocities. This phenomenon is called Faraday rotation and results in a change in the polarization position angle (PPA),

$$\Delta\Psi = \frac{c^2}{\nu^2}\text{RM}, \quad (1.6)$$

which is measured in radians. The rotation measure (RM) is defined as,

$$\text{RM} = \frac{e^3}{2\pi m_e^2 c^4} \int_0^d n_e B_{\parallel} dl, \quad (1.7)$$

with units of  $\text{rad m}^{-2}$ . Since the PPA varies with frequency, the RM can be estimated from FRB observations by measuring the PPA at different frequencies. Interpreting the measured RM is non-trivial as it includes contributions of all media along the line of sight. As the RM can be positive or negative based on the magnetic field direction, contributions from different regions may cancel each other out.

The measured RMs<sup>4</sup> of most FRBs range from 10 to a few hundred  $\text{rad m}^{-2}$  (Petroff et al., 2016). An exception is the repeating FRB, FRB 20121102A, with an RM of  $\sim 10^5$   $\text{rad m}^{-2}$  (Michilli et al., 2018), observed to be decreasing by  $\sim 15\%$  per year (Hilmarsson et al., 2021). The large and variable RM suggests that the FRB inhabits an extreme magneto-ionic environment since the RM contribution of the Milky Way and IGM along the line of sight are both estimated to be  $< 10^2$   $\text{rad m}^{-2}$ . RMs of similar magnitude have only been observed

<sup>4</sup><https://frbcat.org>; accessed in November 2021

in the vicinity of super-massive black holes such as the one at the centre of the Milky Way (Sgr A\*).

## 1.3 Intrinsic Properties

Intrinsic properties of FRBs are difficult to infer from observations due to the aforementioned propagation effects. Additionally, observational biases of different telescopes could result in detection of FRBs with intrinsic properties that are not representative of the entire population. Nevertheless, studies have been conducted to infer properties of the population based on the detected FRB sample. Results from these studies are summarized in the following subsections and associated propagation effects are indicated wherever relevant.

### 1.3.1 Brightness

The brightness of an FRB is measured in terms of its flux density ( $S$ ) and fluence ( $F$ ). While the flux density corresponds to the peak intensity of the burst, the fluence is the integrated flux over the burst width. The flux density is measured in Jansky (Jy;  $10^{-26}$  W m<sup>-2</sup> Hz<sup>-1</sup>) and the fluence is measured in units of Jy ms. The observed fluences for FRBs are shown in Figure 1.3. Although distances to most FRBs are unknown, the measured fluence can be used to constrain the intrinsic energy of the burst by estimating a maximum possible distance. This is done by attributing the entire extragalactic DM of the burst to the IGM, as described in §1.2.1. The upper limits on the inferred isotropic burst energy range from  $10^{38}$  to  $10^{43}$  erg, as shown in Figure 1.3. For each FRB, the upper limit is derived assuming that emission is restricted to the observing bandwidth of the detection instrument.

There also exists a relationship between the extragalactic DM and fluence of FRBs, which was first observed by [Shannon et al. \(2018\)](#). The relationship is demonstrated in Figure 1.3 with low-DM bursts having higher fluences than their high-DM counterparts.

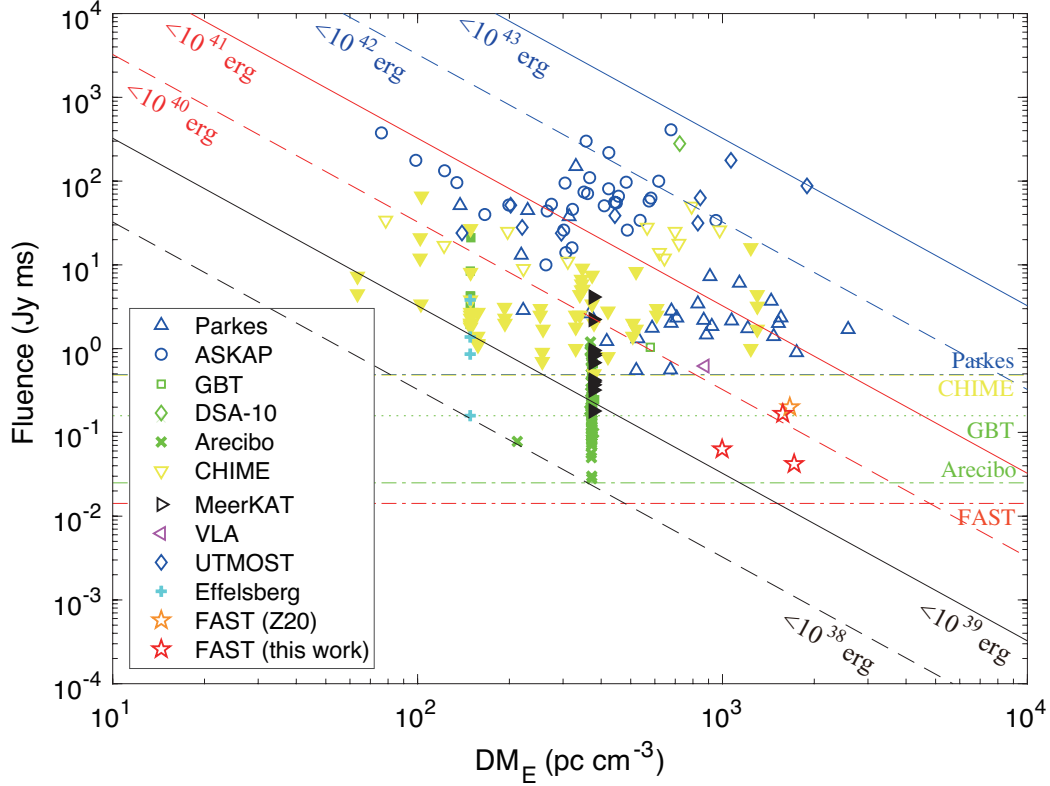


**Figure 1.3:** Distribution of FRB fluences and extragalactic DMs ( $DM_E$ ). Bursts detected with different telescopes are represented by different symbols with the filled symbols showing the repeating FRBs. The horizontal lines indicate telescope sensitivities. Lines of constant isotropic burst energies are also plotted. For most sources, the indicated energies are upper limits as they are estimated based on the maximum possible distance for each source. The measured fluences for FRBs discovered with CHIME are lower limits implying that the inferred energies for these sources could be higher than the indicated values. Figure from [Niu et al. \(2021a\)](#).

The relationship confirms that the extragalactic DM is a proxy for distance, albeit a noisy one since there exists significant scatter in the fluences of bursts with similar DMs.

### 1.3.2 Spectro-Temporal & Polarimetric Properties

Measured FRB pulse widths range from  $80 \mu\text{s}$  to  $34 \text{ ms}$  ([Petroff et al., 2016](#)). The lower end of this range can be explained by most FRB surveys recording intensity data with a sampling time of  $\sim 100 \mu\text{s}$  or more. However, observations of known FRBs with higher time resolution have resulted in detection of narrower bursts with widths as low as  $3 \mu\text{s}$

(Nimmo et al., 2021), constraining the size of the emission region to be less than 1 km (see §1.4). The constraint is less stringent if the emitting region is moving towards the observer at relativistic speeds.

Another sub-population of FRBs which was not detected in initial surveys were bursts with narrow-band emission. Emission in the initial sample was detected across the receiver bandwidth of  $\sim 300$  MHz. However, the recently detected sample of repeating FRBs exhibits narrow-band emission with bandwidths ranging from 60 to 200 MHz (Hessels et al., 2019; CHIME/FRB Collaboration et al., 2019a; Kumar et al., 2021).

Another phenomenon that has been observed particularly in repeating FRBs is sub-burst drifting (Hessels et al., 2019; CHIME/FRB Collaboration et al., 2019a). Some FRBs are comprised of multiple sub-bursts which drift downwards in frequency as time progresses. The drift rate, obtained by fitting a linear slope to the centre frequencies of the sub-bursts, has been measured to be as high as a few hundred MHz  $\text{ms}^{-1}$  and increases with observing frequency (Josephy et al., 2019). It is as yet unknown whether the drifts are caused by the emission mechanism or are a propagation effect.

Repeating and non-repeating FRB sources also differ in terms of their polarimetric properties. Most repeating sources show nearly 100% linear polarization, negligible circular polarization and a flat PPA during and between bursts (Michilli et al., 2018; Nimmo et al., 2021). On the other hand, non-repeating sources exhibit more diverse polarimetric properties (see, e.g. Day et al. 2020). It is as yet unclear whether the difference in polarization properties for repeating and non-repeating sources is due to differing emission mechanisms, progenitors and/or local environments.

### 1.3.3 Ensemble Spectrum

In the decade following the discovery of the first FRB, most FRBs were detected at gigahertz frequencies. In 2018, the CHIME telescope started operating in the frequency range of 400–800 MHz and showed that FRB emission is detectable down to 400 MHz (CHIME/FRB

Collaboration et al., 2019b). However, non-detections with surveys conducted at frequencies ranging from 100 to 400 MHz suggest an apparent dearth of FRBs at low frequencies (e.g., Karastergiou et al. 2015, Chawla et al. 2017).

The dearth could be explained by a positive intrinsic spectral index for FRBs ( $\alpha$ ;  $S_\nu \propto \nu^\alpha$ ), as was suggested by Karastergiou et al. (2015). While a power-law model is not an accurate descriptor of narrow-band bursts, it is used in this context to describe the average spectrum for the FRB population. They concluded that  $\alpha > +0.1$  by comparing the upper limit on the FRB rate at 145 MHz with the 1.4-GHz detection rate. It could also be that most FRBs are rendered undetectable at low frequencies due to scattering, which has a frequency dependence of  $\nu^{-4}$ . Chawla et al. (2017) account for the deleterious effect of scattering on burst detection and find that the non-detection of FRBs with the GBNCC survey at 350 MHz still favours a relatively flat spectrum ( $\alpha > -0.3$ ).

The aforementioned constraints are in tension with the average spectral index observed for 23 ASKAP FRBs,  $\alpha = -1.5^{+0.2}_{-0.3}$ . These disparate indices can be reconciled if the non-detection at low frequencies is due to a spectral turnover. Such a turnover is possible if FRBs inhabit dense, ionized environments such as a supernova remnant and processes such as free-free absorption or induced Compton scattering play a role. The optical depth to these phenomena increases at lower frequencies and can render the low-frequency emission undetectable (Ravi & Loeb, 2019).

Despite the observed reduction in FRB rate at low frequencies, targeted searches for low-frequency emission from repeating FRB sources can be fruitful, especially if some of these sources inhabit less dense environments compared to the rest of the population. Follow-up observations at 350 MHz of one such source, FRB 20180916B, are presented in Chapter 4.

### 1.3.4 Repetition and Periodicity

Of the 612 FRBs known to date, 24 have been observed to repeat<sup>5</sup> allowing cataclysmic progenitor models to be ruled out for these sources (see §1.4). Other FRBs have been followed up for hundreds of hours with no repeat bursts being detected (see, e.g., [Shannon et al. 2018](#)). It could be that all FRBs repeat but with vastly different repetition rates. This hypothesis is supported by the volumetric occurrence rate of potential cataclysmic progenitors being significantly lower than that inferred for non-repeating FRBs ([Ravi, 2019](#)), suggesting that a large fraction of the one-off FRBs must originate from repeating sources. The result is contingent on the assumption that non-repeating sources are associated with cataclysmic progenitors.

Burst widths of repeating FRBs are found to be larger, on average, than those of non-repeating sources ([Scholz et al., 2016](#); [CHIME/FRB Collaboration et al., 2019a](#); [Fonseca et al., 2020](#)). This observation suggests that repeating and non-repeating sources have different emission mechanisms and/or local environments. However, it is as yet unclear whether repeating FRBs have a different progenitor than the so-far non-repeating sources.

More recently, two repeating FRBs have been observed to exhibit periodic activity. The first of these sources, FRB 20180916B, exhibits modulation in its activity at a 16.35 day period with a 5-day long activity window ([CHIME/FRB Collaboration et al., 2020a](#)). Following this discovery, a periodicity of  $\sim 160$  days was detected in the activity of the first repeating FRB, FRB 20121102A, with an activity window spanning 60% of the period ([Rajwade et al., 2020b](#); [Cruces et al., 2021](#)). Progenitor models with sporadic emission of pulses can be ruled out for these sources with models involving orbital motion or precession at the detected periods being favoured (see §1.4).

---

<sup>5</sup><https://wis-tns.org>; accessed in November 2021

### 1.3.5 Host Galaxies & Local Environments

Identification of FRB host galaxies is crucial to understand FRB progenitors. Once a host galaxy is identified, the redshift can be determined which provides an estimate of burst energetics. Additionally, global properties of the host galaxy, such as the star formation rate and stellar mass, can lend support to or rule out certain progenitor models. As an example, if FRBs were giant pulses from young neutron stars, then one would expect their host galaxies to have a high star formation rate.

Most existing radio telescopes provide positional uncertainties of the order of arcminutes. In general, such a localization region contains many galaxies prohibiting conclusive identification of the host. However, host galaxies have been identified for 20 FRBs<sup>6</sup> (Heintz et al., 2020), including eight repeating sources. These FRBs were observed with long-baseline interferometers which provide sub-arcsecond localizations. The closest of these FRBs is located in the M81 galaxy (Bhardwaj et al., 2021; Kirsten et al., 2021) and the farthest at a redshift of 0.66 (Ravi et al., 2019).

Two repeating FRB sources have been localized to star-forming dwarf galaxies (Tendulkar et al., 2017; Niu et al., 2021b). The rest of the localized sample includes spiral and elliptical hosts spanning the entire parameter space occupied by  $z < 0.5$  galaxies in terms of their colour, masses and star formation rate (Heintz et al., 2020). More host galaxy associations are required to draw definitive conclusions about the entire population and ascertain whether the hosts of repeating and non-repeating FRBs have different properties.

Localizations of the order of 100 milli-arcseconds can help determine where an FRB is located within its host galaxy. The first repeating FRB, FRB 20121102A, was found to be associated with a persistent, compact ( $< 0.7$  pc) radio source (Chatterjee et al., 2017). The constraint on the source size and the inferred brightness temperature ( $T \sim 10^7$  K) favours two progenitor models, namely, a young neutron star energizing a supernova remnant or a low-luminosity active galactic nucleus (Marcote et al., 2017). On the other hand, several

---

<sup>6</sup><https://frbhosts.org>; accessed in November 2021

ASKAP FRBs are located in the outskirts of their host galaxies which disfavours progenitor models involving active galactic nuclei (Bhandari et al., 2020). A larger sample of localized FRBs can thus reveal the progenitors of FRBs through detailed characterization of their local environments.

## 1.4 Progenitor Models

Over 50 models have been proposed to explain the FRB phenomenon with most of them invoking neutron stars or black holes as progenitors. Compact objects are favoured as progenitors since the observed pulse widths ( $w$ ) constrain the size of the emission region to be less than  $cw$  so as to not violate causality. For a pulse of millisecond duration, this corresponds to a maximum size of 300 km. The size of the emission region could be larger if emission is being caused by relativistic plasma.

We explore the proposed models in detail in the following subsections<sup>7</sup>. Any proposed model must be able to explain the observed all-sky FRB rate and the inferred isotropic energy output, ranging from  $10^{38}$  to  $10^{43}$  erg (see Figure 1.3). Additionally, the associated emission mechanism should be coherent. This constraint is based on the brightness temperature of FRBs,  $T_B$ , which is the thermodynamic temperature of a black body emitting radiation of equivalent intensity,

$$I_\nu = \frac{2\nu^2 k T_B}{c^2}. \quad (1.8)$$

Here  $k$  is the Boltzmann constant and  $I_\nu$  is the peak flux density per unit solid angle. The inferred brightness temperature for a ms-duration fiducial burst detected with a peak flux density of 1 Jy at a frequency of 1 GHz is  $\sim 10^{35}$  K, assuming a distance of 1 Gpc. Such a high brightness temperature rules out any incoherent mechanism implying that FRBs must emit coherent radiation.

---

<sup>7</sup>A summary of the proposed models is available at <https://frbtheorycat.org> (Platts et al., 2019)

### 1.4.1 Isolated Neutron Stars

#### Pulsars

Rotationally-powered neutron stars, such as the Crab pulsar, can explain the inferred energy output of FRBs only if they are located at distances  $< 100$  Mpc (see, e.g., [Connor et al. 2016](#); [Lyutikov et al. 2016](#)). [Cordes & Wasserman \(2016\)](#) propose that pulsar giant pulses of nanosecond duration can superpose incoherently and generate FRBs of millisecond duration. However, in order to be detectable at gigaparsec distances, these giant pulses must be emitted by young neutron stars with millisecond-rotation periods having high magnetic fields and large magnetospheric energy available for an outburst. [Cordes & Wasserman \(2016\)](#) stipulate that the observed FRB rate can be matched only if multiple bursts are detected from each neutron star. If FRBs are produced by young pulsars, then the DM and RM evolution of the supernova ejecta around these sources could be detectable with follow-up observations of repeating FRBs ([Piro & Gaensler, 2018](#)).

#### Magnetars

Magnetars are neutron stars with strong magnetic fields ranging from  $10^{14}$  to  $10^{15}$  G ([Duncan & Thompson, 1992](#)). The recent detection of an energetic ( $10^{34}$  erg), millisecond-duration radio burst from the Galactic magnetar SGR 1935+2154 suggests that magnetars could be producing at least some fraction of the FRB population ([Bochenek et al., 2020](#); [CHIME/FRB Collaboration et al., 2020b](#)).

[Popov & Postnov \(2013\)](#) proposed that FRBs could be associated with hyper-flares in the magnetospheres of extragalactic magnetars. The model was further developed by [Lyubarsky \(2014\)](#) who suggested that FRBs could be powered by synchrotron maser emission from the relativistic shock formed by the interaction of the magnetized flare ejecta with the surrounding nebula. Since then, several models have been proposed invoking magnetar flares as the source of FRBs albeit involving different emission mechanisms (see,

e.g., [Katz 2016b](#); [Beloborodov 2017](#)).

[Metzger et al. \(2017\)](#) concluded that the repeat bursts of FRB 20121102A can be generated by flares from a young magnetar with a millisecond-rotation period powering a decades-old supernova remnant. The observation of the persistent radio source associated with this FRB and the large but decreasing RM of the repeat bursts can also be explained by this model ([Margalit & Metzger, 2018](#)).

Following the discovery of a 16.35-day modulation in the activity of FRB 20180916B, it was suggested that magnetars can precess freely with a period of hours to weeks ([Levin et al., 2020](#); [Zanazzi & Lai, 2020](#)). Anisotropic flaring activity of the magnetar combined with the precession can modulate the burst rate on these timescales.

Alternately, the modulation in burst activity could be due to the rotation of the magnetar. Although known Galactic magnetars<sup>8</sup> ([Olausen & Kaspi, 2014](#)) have rotational periods  $< 12$  s, [Beniamini et al. \(2020\)](#) suggest that particle winds, giant flares or supernova fallback accretion can transfer angular momentum away from a magnetar, resulting in periods ranging from  $10^4$  to  $10^6$  s. While precession or rotation can potentially explain the periodicity of FRB 20180916B, the 160-day period observed for FRB 20121102A is difficult to reconcile with either of these models ([Rajwade et al., 2020b](#)).

### 1.4.2 Compact Object Mergers

It has been suggested that the merger of two neutron stars (NS) can produce FRB-like emission either through an electromagnetic precursor wind ([Lyutikov, 2013](#)) or at the time of coalescence ([Totani, 2013](#)). In the latter model, the magnetic fields of the neutron stars synchronize with the binary rotation, generating coherent emission by magnetic braking. Potential counterparts include a short GRB and/or a gravitational wave signal.

Binary white dwarf (WD) mergers have also been proposed as a source of FRBs by [Kashiyama et al. \(2013\)](#) wherein the polar region of the rapidly rotating, magnetized WD

---

<sup>8</sup><http://www.physics.mcgill.ca/~pulsar/magnetar/main.html>

formed after the merger is the source of coherent emission. The model predicts that some FRBs could be observed simultaneously with a type Ia supernova. Proposed progenitors also include binary black hole (BH) mergers (Zhang, 2016) and NS-BH mergers (Mingarelli et al., 2015). While the FRB rate is consistent with the binary NS-merger rate (Totani, 2013), the other merger models can only explain a small fraction of the FRB population ( $< 5\%$ ).

### 1.4.3 Other Models

Interaction between two compact objects, as opposed to a merger, has also been proposed as a source of FRB emission. For example, Gu et al. (2016) argue that accretion of material from a white dwarf onto a neutron star can produce repeating FRBs. Repeated interactions between a neutron star and an asteroid belt can potentially produce FRB-like emission (Geng & Huang, 2015; Dai et al., 2016). This model can also explain the periodicity observed for repeating FRBs as bursts would be produced at a particular orbital phase. Periodic FRB emission can be explained by another interaction model, a neutron star interacting with the wind of its stellar companion, the opacity for which varies with orbital phase (Lyutikov et al., 2020). Alternately, Sridhar et al. (2021) propose that FRBs in X-ray binary systems could be powered by flares from accreting neutron stars or black holes. In these models, the periodicity of the emission is attributed to the precession of the accretion funnel, along which the FRB emission is beamed.

There are models which invoke more exotic progenitors than those described above. These progenitors include neutral or superconducting cosmic strings (Vachaspati, 2008; Brandenberger et al., 2017), axion stars interacting with neutron stars or black holes (Raby, 2016; Iwazaki, 2017) or stars comprised of strange quarks (Zhang et al., 2018).

## 1.5 Outline of Thesis

This thesis aims to further our current understanding of the FRB population using the CHIME/FRB project, which has now detected hundreds of FRBs ([CHIME/FRB Collaboration et al., 2021a](#)). Chapter 2 describes the CHIME telescope and the CHIME/FRB real-time detection pipeline. Chapter 3 discusses algorithms developed to evaluate the sky exposure of the CHIME/FRB system and outlines the use of the estimated exposure in determining FRB repetition rates. Chapter 4 reports on follow-up observations of FRB 20180916B and discusses the properties inferred for its circumburst environment based on these observations. Chapter 5 reports on a population synthesis study of dispersion and scattering in the first CHIME/FRB catalog and the resulting constraints on FRB progenitor models and circumburst environments. Chapter 6 summarizes the conclusions of each chapter and details prospects for future research.

## Chapter 2

### The CHIME/FRB Project

Prior to 2016, most FRB searches were conducted using single-dish telescopes such as Parkes (64 m in diameter), Arecibo (300 m) and the Green Bank telescope (100 m), which is shown in Figure 2.1. The reflective surface of the dish directs radio waves from the sky towards a receiver which is mounted at the focal point. The response of the receiver is similar to a diffraction pattern, with the central maximum referred to as the main beam of the telescope. The full width at half maximum (FWHM) of the main beam is approximately equal to the diffraction limit for the telescope,

$$\theta = 1.22 \frac{\lambda}{D}. \quad (2.1)$$

Here  $D$  is the dish diameter and  $\lambda$  is the observing wavelength.

There are two disadvantages to using single-dish telescopes for FRB searches, with the first being low detection rates. As an example, the single-dish telescope with the highest FRB yield, the Parkes telescope, has a beam FWHM of 0.23 deg (Burke-Spolaor & Bannister, 2014). Since the telescope is equipped with a 13-beam receiver, the total FOV is 0.6 sq. deg. Despite the all-sky FRB rate being  $1.7_{-0.9}^{+1.5} \times 10^3$  per day above the Parkes sensitivity threshold (Bhandari et al., 2018), the FOV results in a relatively low detection rate of  $\sim 0.2$  bursts per day. Moreover, most single-dish telescopes have a limited time dedicated to FRB searching, resulting in the actual detection rate being significantly lower than the above estimate.

Another disadvantage of single-dish telescopes is the large uncertainty in the position of

the FRBs discovered with these instruments. The localization uncertainty is comparable to the beam FWHM, which prevents conclusive identification of the host galaxy. Telescopes with larger diameters can provide higher angular resolution. However, there are logistical constraints associated with constructing larger dishes.



**Figure 2.1:** The Robert C. Byrd Green Bank telescope located in West Virginia, USA. It is the largest steerable radio telescope in the world, with the reflecting dish having a diameter of 100 m. The telescope can operate at frequencies ranging from 290 MHz to 116 GHz using receivers which are sensitive to different frequency ranges. The off-axis support arm houses these receivers. Image credit: National Radio Astronomy Observatory.

An alternate approach to constructing large single-dish telescopes is to coherently combine the signals from several receivers using interferometry. Interferometric radio telescopes which are being used to conduct FRB searches include CHIME, ASKAP, UTMOST and the Low-Frequency Array (LOFAR; [van Haarlem et al. 2013](#)). The designs of these instruments vary. As an example, ASKAP is made up of 36 dishes, each equipped with a phased array feed comprising of 188 receivers. On the other hand, CHIME consists of four cylindrical paraboloids with 256 antennas located on the focal line of each cylinder.

Signals from different elements of an interferometric array are combined in the correlator of the telescope in a process that requires large computational resources. Time delays are

applied to the output of each array element in order to sum the signals in phase. This allows the telescope to point at a particular sky location by correcting for the geometric delay between different antennas.

Interferometers generally provide better localization than single-dish telescopes. This is because their angular resolution is not determined by the size of a single dish, but by the maximum separation between two constituent antennas or dishes. The FOV of interferometers is instead dictated by the diameter of the reflecting surface associated with an array element. The FOV can thus be larger than that of single-dish telescopes with comparable localization capabilities. The following sections will describe one particular interferometric telescope, the CHIME telescope. CHIME has a large instantaneous FOV of  $\sim 250$  sq. deg., resulting in a detection rate of  $\sim 2.5$  FRBs per day ([CHIME/FRB Collaboration et al., 2021a](#)).

## 2.1 The CHIME Telescope

The Canadian Hydrogen Intensity Mapping Experiment (CHIME) telescope is located on the grounds of the Dominion Radio Astrophysical Observatory (DRAO) in British Columbia, Canada. The telescope has four  $20\text{-m} \times 100\text{-m}$  cylindrical paraboloid reflectors oriented in the north-south (N-S) direction. The cylinders have a total collecting area of  $8000\text{ m}^2$  and a focal length of 5 m. The focal line of each cylinder is populated by 256 antennas, which are sensitive in the frequency range of 400–800 MHz. The telescope is shown in Figure 2.2.

The telescope has no moving parts and can only observe a strip of sky transiting directly overhead. The FOV extends  $\sim 120^\circ$  in the N-S direction and  $1.3^\circ$ – $2.5^\circ$  (depending on the frequency) in the east-west (E-W) direction. As the Earth rotates, different sky locations transit across the FOV. This results in CHIME being able to observe the entire sky with declination,  $\delta > -10^\circ$ , every day.



**Figure 2.2:** The CHIME telescope located in British Columbia, Canada. It is a transit telescope comprising of four  $20\text{-m} \times 100\text{-m}$  cylindrical paraboloid reflectors. Incoming radio waves are directed towards the focal line of each cylinder, which is populated by 256 dual-polarization feeds. The feeds are sensitive in the frequency range of 400–800 MHz. In contrast with the smooth aluminum panels used for the GBT, the reflecting surface for CHIME is made of galvanized steel mesh. This is because CHIME is sensitive to lower radio frequencies for which the antenna efficiency is not affected by greater surface irregularities. Image credit: CHIME Collaboration.

### 2.1.1 Science Goals

The original design goal for CHIME is to observe the 21-cm (1420 MHz) emission from neutral hydrogen gas located in the redshift range  $0.8 < z < 2.5$ . The emission will be redshifted and can thus be observed in the CHIME band (400–800 MHz). The experiment will map the baryon acoustic oscillation (BAO) features in the neutral hydrogen emission, enabling a measurement of the expansion history of the universe (Newburgh et al., 2014). Since dark energy is expected to dominate the energy density of the universe in the aforementioned redshift range, the experiment can constrain the equation of state of dark energy.

Another key science goal is to perform high-cadence observations of Galactic pulsars. The CHIME/Pulsar system observes 400–500 known pulsars each day (CHIME/Pulsar Collaboration et al., 2021). The pulse arrival times determined from these observations can help understand the rotational history of pulsars using a technique called pulsar timing.

Observed deviations from predicted arrival times can enable measurement of changes in the internal properties of the neutron star (see, e.g., [Espinoza et al. 2011](#)) and observation of general relativistic effects (see, e.g., [Demorest et al. 2010](#)).

Timing observations of an array of millisecond pulsars with stable rotation periods, known as a pulsar timing array, can potentially detect low-frequency gravitational waves (GWs; see, e.g., [Perera et al. 2019](#)). CHIME/Pulsar timing observations will be combined with data from the North American Nanohertz Observatory for Gravitational Waves (NANOGrav; [Ransom et al. 2019](#)) to aid in the search for GWs produced by super-massive black hole binaries ([Arzoumanian et al., 2020](#)).

The third science goal, which is the subject of this thesis, is searching for FRBs. The large FOV and the high up-time ( $\sim 70\%$  for the first year of operations; [CHIME/FRB Collaboration et al. 2021a](#)) make it an ideal instrument to detect and characterize the FRB population. The CHIME/FRB detection pipeline is discussed in detail in §2.2.

### 2.1.2 Analog Signal Chain

CHIME observes the sky using 1024 cloverleaf-shaped feeds ([Deng & Campbell-Wilson, 2017](#)), which measure the variations in the electric field of the incoming waves and convert them into voltage signals. The feeds are placed 30.48 cm apart along 80 m of the focal line of each cylinder. Each feed is sensitive to two linear polarizations, resulting in a total of 2048 input signals for the telescope. The signals are amplified using low-noise amplifiers (LNAs) attached to each feed. The noise for the LNAs is  $< 35$  K across the majority of the band ([Bandura et al., 2014](#)).

After amplification, the signals are sent to the receiver huts using a network of coaxial cables. The telescope has two receiver huts which are located between each pair of cylinders. Signals from two cylinders are amplified and bandpass-filtered (400–800 MHz) in each receiver hut. The huts also provide liquid cooling and shield the F-engine electronics from radio frequency interference (RFI). The F-engine is responsible for digitization and

frequency channelization of the input signals and is described in the following subsection.

### 2.1.3 Correlator

The 2048 input signals are correlated with each other using a correlator of hybrid FX design. The signals are digitized and channelized in the F-engine, following which they are spatially correlated in the X-engine. The F-engine uses 128 “ICE” motherboards (Bandura et al., 2016a,b), each of which contain custom-designed field programmable gate arrays (FPGAs). The analog voltage signals are first digitized and then channelized into 1024 frequency bins using a polyphase filter bank (see, e.g., Price 2016). At this stage, complex gain and phase corrections are applied to each frequency channel. The frequency and time resolution of the channelized data are 390 kHz and 2.56  $\mu$ s, respectively.

The channelized data are re-organized before being sent to the X-engine, which is a GPU cluster with 256 nodes (Denman et al., 2020). The re-organization ensures that the data for a single frequency channel from all 2048 digitized inputs are processed by the same GPU node. Each node performs the spatial correlation for four frequency channels. The spatial correlation produces visibilities, which are required for the intensity mapping experiment. However, the CHIME/FRB project requires spatially localized beams which can be individually searched for FRBs. The beam-forming process for the CHIME/FRB system is performed by the GPU nodes of the X-engine (see §2.1.4). The X-engine also has a memory buffer which stores 35.5 s of baseband (raw-voltage) data from all 2048 inputs. As of December 2018, the buffered data can be saved to disk upon detection of a candidate FRB event (see §2.2.3). A detailed description of the baseband recording system is presented elsewhere (Michilli et al., 2021).

### 2.1.4 Beam-forming

An incoherent beam can be formed by adding the signals for all antennas without applying any phase offsets. While the incoherent beam FOV is equivalent to that for the primary

beam of an individual antenna ( $\sim 250$  sq. deg.), the sensitivity is proportional to  $\sqrt{N}$ , where  $N$  is the total number of antennas. In order to determine the position of an FRB within this FOV, it is essential to tile the primary beam with multiple beams formed by coherently adding the signals from all antennas. The sensitivity for the coherent case is proportional to the number of antennas.

Phase offsets must be applied to the signals from each antenna in order to add them coherently. These offsets compensate for the differences in light travel time between the feeds and vary based on the sky position that is being observed. However, additional phase delays and amplitude variations can be introduced due to the analog-signal chain or the F-engine electronics. The amplitude ( $A$ ) and phase ( $\phi$ ) variations are expressed as the complex gain,  $G = Ae^{-i\phi}$ . The complex gain is determined by performing an amplitude and phase calibration for all frequency channels and polarizations corresponding to each antenna prior to beam-forming. Complex gains are evaluated once every sidereal day using transits of one of the following bright effective point sources: Cas A, Cyg A, Vir A and Tau A (Trotter et al., 2017).

The beam-forming process for the CHIME/FRB system is described in detail by Ng et al. (2017). In summary, a fast Fourier transform (FFT) algorithm (see, e.g., Tegmark & Zaldarriaga 2009; Masui et al. 2017) is used to form 256 beams in the N-S direction. Four columns of beams are formed in the E-W direction via exact phasing, resulting in a total of 1024 beams. In the N-S direction, the beams are evenly spaced in  $\sin \theta$ , where  $\theta$  is the zenith angle. The beam spacing in the E-W direction is a tunable parameter, as is the N-S extent of the beams.

In the pre-commissioning phase of the CHIME/FRB project (2018 July 25 – 2018 August 27), beams were formed from horizon to horizon ( $\theta = -90^\circ$  to  $\theta = +90^\circ$ ) with an E-W spacing of  $0.1^\circ$ . This configuration was not ideal due to the reduced primary beam response and RFI contamination for the beams located close to the horizon. Therefore, at the end of the pre-commissioning period, the N-S extent was modified to  $\theta = -60^\circ$  to  $+60^\circ$ . Additionally,

the E-W spacing was set to  $0.4^\circ$  to reduce the overlap between beams and increase the overall sky coverage. The configuration of the synthesized beams has not been changed since. The relative locations of the beams and their extents are shown in Figure 2.3. The beam FWHM in the E-W direction ranges from  $0.25^\circ$  at 800 MHz to  $0.5^\circ$  at 400 MHz. The aspect ratio (E-W versus N-S) varies from 1:1 at zenith to 1:2 at  $\theta = \pm 60^\circ$ .

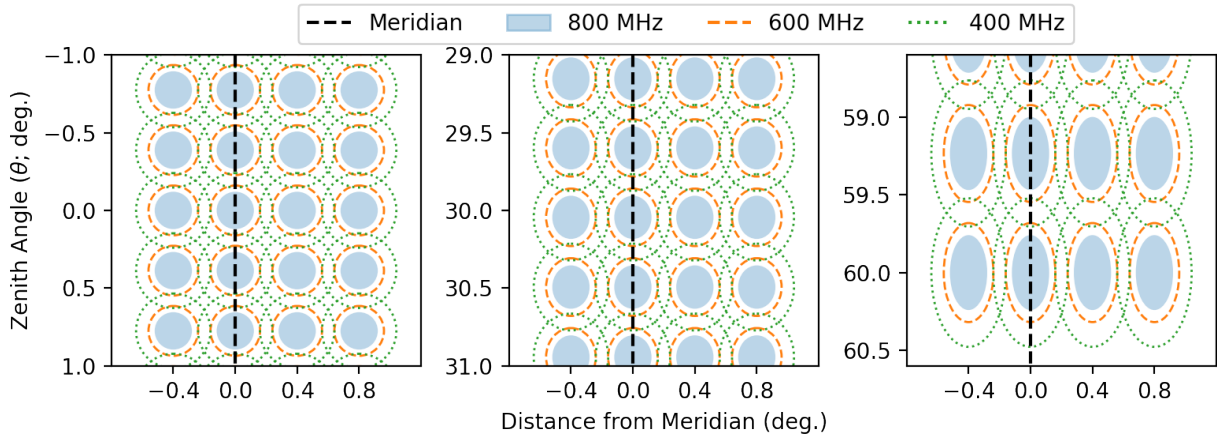


**Figure 2.3:** Sky positions for a subset of the synthesized beams of the CHIME/FRB system. An FFT algorithm forms 256 beams in the N-S direction with four beams in the E-W direction formed by exact phasing (see §2.1.4). The beams are spaced evenly in  $\sin \theta$ , where  $\theta$  is the zenith angle. Beams extend from  $\theta = -60^\circ$  to  $\theta = +60^\circ$  and are spaced by  $0.4^\circ$  in the E-W direction. The three panels show beams located at different zenith angles. The ellipses indicate the half-power widths of the beams at different frequencies, as indicated in the legend. The beams are wider at lower frequencies with substantial overlap at a frequency of 400 MHz. Additionally, the beams are more elongated closer to the horizon, as shown in the rightmost panel. The location and extent of the beams are computed using the CHIME/FRB beam model (CHIME/FRB Collaboration et al., 2021a).

### 2.1.5 Up-channelization

The X-engine receives data channelized into 1024 frequency bins, each 390 kHz in width. The dedispersion process in the CHIME/FRB detection pipeline has to correct for the delay of these frequency channels with respect to each other. However, each channel will retain a residual delay due to its finite bandwidth, which is known as dispersive smearing. The

dispersive delay across a frequency channel of width  $\Delta\nu_{\text{chan}}$  is given by,

$$t_{\text{chan}} \simeq 8.3 \times 10^6 \text{ ms} \times \text{DM} \times \Delta\nu_{\text{chan}} \times \nu^{-3}, \quad (2.2)$$

with the frequencies expressed in MHz (Lorimer & Kramer, 2004). For a burst at a fiducial DM of  $1000 \text{ pc cm}^{-3}$  detected at a frequency of 600 MHz,  $t_{\text{chan}} \sim 15 \text{ ms}$  for a channel width of 390 kHz. Therefore, a spectral resolution of 390 kHz is not ideal for detecting bursts with widths  $< 15 \text{ ms}$  as intrachannel smearing would dilute the burst signal in time.

To mitigate the effect of dispersive smearing, an FFT up-channelization is performed before the data are processed by the CHIME/FRB detection pipeline (Ng et al., 2017). Voltage samples for 128 successive time bins ( $\Delta t = 2.56 \mu\text{s}$ ) are summed and Fourier-transformed. The square of the magnitude of the resulting spectrum is downsampled by a factor of 8, following which three successive downsampled transforms are averaged together. Lastly, the two orthogonal polarizations are summed, producing Stokes I data for each synthesized beam. The frequency and time resolution of this data are 24.4 kHz and 0.983 ms, respectively.

## 2.2 CHIME/FRB Detection Pipeline

The CHIME/FRB system includes a real-time software pipeline which searches for dispersed astrophysical events. While the pipeline is designed to detect FRBs, single pulses from pulsars and RFI can also be detected. The pipeline has five different stages, named L0 through L4. The beam-forming and up-channelization operations described in §2.1.4 and §2.1.5 are collectively referred to as the L0 stage. L1 performs RFI excision, dedispersion and identifies candidate events in each synthesized beam. The L2 and L3 stages combine the detection information for events detected in multiple beams and classify the events. L4 stores the detection information for all events in a database and implements different actions based on the event classification.

A schematic of the detection pipeline is shown in Figure 2.4 while a brief summary of the operations performed at each stage is presented in the following subsections. Further details are presented in [CHIME/FRB Collaboration et al. \(2018\)](#).

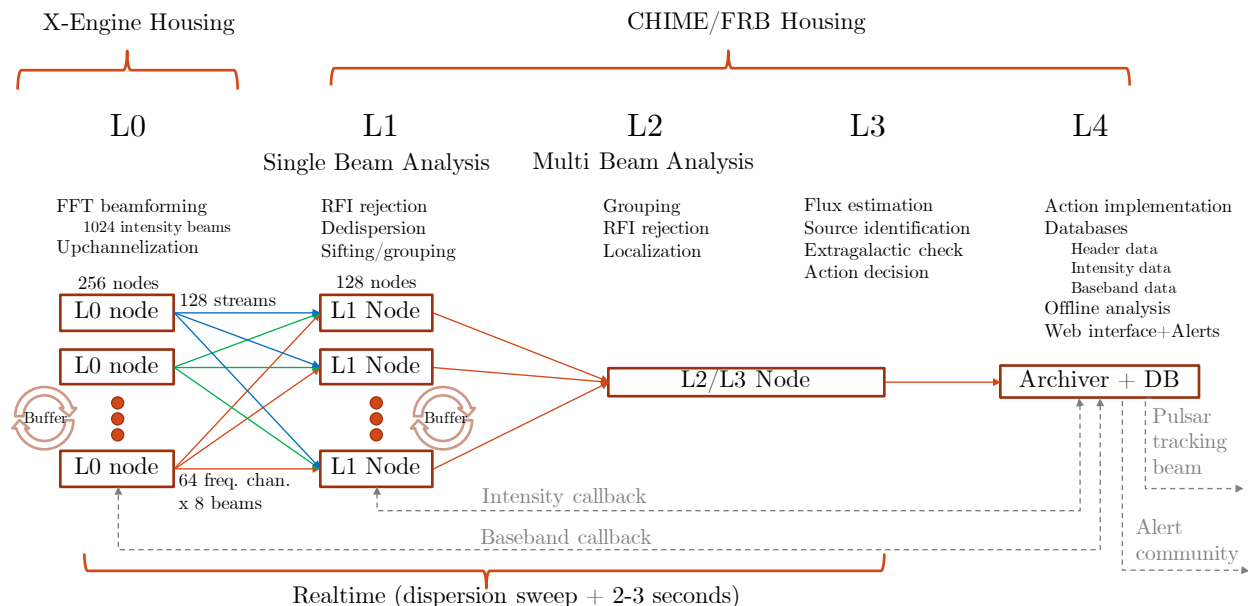


**Figure 2.4:** Schematic of the CHIME/FRB detection pipeline, which is described in detail in §2.2. L0 performs the beam-forming and up-channelization with each node processing data for four frequency channels. L1 performs RFI excision and dedispersion with each node processing data for eight synthesized beams. The L2 and L3 stages group events detected in multiple beams and classify these events. L4 performs different actions based on the event classification such as storing events in databases and initiating data callbacks. Data are continuously buffered by the L0 and L1 stages for baseband and intensity data callback, respectively. Figure from [CHIME/FRB Collaboration et al. \(2018\)](#).

### 2.2.1 L1: Dedispersion and Event Identification

The L1 pipeline runs on a dedicated cluster with 128 CPU nodes. Each node performs RFI cleaning and dedispersion on channelized intensity data for eight synthesized beams. A ‘telescoping’ ring buffer has also been implemented for each node, which stores a few minutes worth of data at any time. The data can be saved to disk if a candidate FRB event is detected (see §2.2.3). The telescoping feature of the buffer entails successive downsampling of the data as time progresses. The downsampling ensures that the full dispersive sweep for

high-DM events can be captured.

While the observatory is located in an area where use of any unshielded electronic devices is prohibited, some broad-band and narrow-band RFI signals can still contaminate the recorded data, resulting in reduced sensitivity to FRBs. RFI excision is performed in several stages of the CHIME/FRB pipeline with the `rf_pipelines`<sup>1</sup> module included in the L1 stage for this purpose. The module performs a series of detrending and clipping operations. The former operations remove any constant or linear trends in the data while the latter identify frequency channels or time samples with above-average intensity, replacing them with the mean intensity or a constant user-defined value. The operations are written in C++ and assembly language to reduce computational overhead and achieve real-time processing. Additionally, the entire algorithm has been trained on data from the CHIME Pathfinder telescope (Bandura et al., 2014), which is also located at DRAO and observes a similar RFI environment.

Following RFI excision, the data streams from all synthesized beams need to be dedispersed (see §1.2.1). There are two techniques for dedispersion, namely, coherent and incoherent. The process of incoherent dedispersion (see, e.g., Lorimer & Kramer 2004) involves applying frequency-dependent time delays to channelized intensity data,  $I(t, \nu)$ . On the other hand, a frequency-dependent phase shift is applied to the Fourier transform of the raw voltage signal during coherent dedispersion (Hankins & Rickett, 1975). A coherently-dedispersed signal retains the instrumental time resolution as opposed to the dispersive smearing seen in the case of incoherent dedispersion (see §2.1.5). However, coherent dedispersion requires the DM of the source to be known a priori in order to compute the phase shift.

Since a search for FRBs has to be conducted at different trial DMs, the detection pipeline uses the incoherent dedispersion technique. L1 performs dedispersion using `bonsai` (Smith et al., in prep.), which implements the tree dedispersion algorithm (see, e.g., Taylor 1974;

---

<sup>1</sup>[https://github.com/kmsmith137/rf\\_pipelines](https://github.com/kmsmith137/rf_pipelines)

Zackay & Ofek 2017). The algorithm performs a dedispersion transform converting  $I(t, \nu)$  to  $I(t, \text{DM})$  by summing over all possible dispersion sweeps along the frequency axis. For neighbouring DM trials, summation of the same set of frequency bins could be required. The algorithm is efficient in that it performs each unique set of summations once. The computational cost for tree dedispersion is  $N_\nu N_t \log_2 N_\nu$ , as compared to  $N_\nu N_t N_{\text{DM}}$  for brute-force incoherent dedispersion, where  $N_\nu$ ,  $N_t$  and  $N_{\text{DM}}$  are the number of frequency, time and DM bins, respectively (Zackay & Ofek, 2017).

The search uses multiple dedispersion trees, with successively lower time resolution. The temporal downsampling for the high-DM trees reduces computational complexity. This does not affect the search sensitivity as dispersive smearing effectively reduces the time resolution for these trees. The search is conducted up to a maximum DM of  $13000 \text{ pc cm}^{-3}$ . Additionally, we search over two different spectral indices,  $-3$  and  $+3$ . This increases our sensitivity to narrow-band bursts with emission at either edge of the band. The other two parameters that the search is performed over are arrival times and intrinsic widths, up to a maximum width of  $\sim 60 \text{ ms}$  (Pleunis, 2020).

The code produces a four-dimensional array of S/N values, which shows how the S/N varies for different trial DMs, arrival times, spectral indices and intrinsic widths. This grid is then “coarse-grained” in time and DM, i.e. the time and DM bins are downsampled with the maximum S/N in the downsampled bins being used for further operations. The algorithm finds local maxima in a region spanning  $10 \text{ pc cm}^{-3}$  in DM and  $0.25 \text{ s}$  in time. If any of these peaks has a S/N above the threshold of  $8\sigma$ , then it is classified as an L1 event and processed further. Information about an L1 event is stored in a data structure called the “L1 header”. The header includes the DM of the event, S/N, arrival time and central coordinates of the beam in which the event was detected.

### 2.2.2 L2/L3: Multi-beam Grouping and Event Classification

The L1 headers from all synthesized beams are streamed to a single node which runs the L2 and L3 processes. Bright events can be detected in multiple beams and these detections need to be grouped together. The L2 stage groups the L1 events detected in different beams, improving the measurement of burst properties in the process. Once L1 headers have been received from all beams for a single time chunk, grouping is done using a clustering algorithm, DBSCAN (Ester et al., 1996). L1 events are grouped together only if their DMs, arrival times and sky positions are consistent within user-defined thresholds. The position threshold allows grouping of events detected in neighbouring beams. The thresholds in DM and time are based on the sizes of the coarse-grained bins used at the L1 stage. Information about grouped L1 events is saved together as an L2 event.

Both L1 and L2 events are assigned an RFI grade using machine learning-based classifiers. The probability of an L1 event being caused by RFI is estimated by studying the variation in burst S/N for different DM trials. The S/N of an astrophysical event is highest at the optimal DM but is reduced above or below the optimal DM due to dispersive smearing. In comparison, an RFI event is detected with similar S/Ns in several DM trials. Once grades have been assigned to L1 events, the L2 event is classified as either being RFI or astrophysical. Among other parameters, this classification is based on the event DM, maximum S/N, the RFI grade of the constituent L1 events and the level of activity (number of candidates detected) in all synthesized beams at the time of detection. Beam activity is an important factor as we expect RFI events to be detected in multiple beams. Events classified as RFI are stored in the L4 database (see §2.2.3) without any further processing.

The pipeline refines the sky position for the L2 events which are deemed to be astrophysical. Although the constituent L1 events have the central coordinates of the detection beam recorded as the sky position, this position can be refined further if an event is detected in multiple beams. This is done by comparing the detection S/Ns for all beams with the expectation from the beam model. The expected relative S/Ns as a function of

sky position, spectral index ( $-3$  and  $3$ ) and burst S/N are stored in a pre-computed look-up table. The L2 events with the updated sky positions are sent to the L3 stage for further processing.

The L3 process identifies which of the astrophysical events are extragalactic. This is a necessary step as single pulses can be detected from known or previously undiscovered pulsars and rotating radio transients<sup>2</sup> (RRATs) in the Galaxy. FRBs need to be distinguished from pulsars and RRATs in real time as the processing-related actions triggered by the pipeline would be different for each class of sources. As an example, the pipeline stores intensity data to disk for extragalactic events. However, detection of a pulse from a Galactic pulsar would not necessitate such an action.

The sky position and DM of each event is compared with those of known pulsars<sup>3</sup> (Manchester et al., 2005), RRATs<sup>4</sup> and FRBs<sup>5</sup> (Petroff et al., 2016). An event is classified as known if its position is consistent with that of any known source within measurement uncertainties. The discoveries made by the CHIME/FRB system are also added to the database of known sources to enable identification of repeating FRBs.

The events which cannot be associated with any known source are classified based on their DM. The event DM is compared with the maximum Galactic DM along the line-of-sight predicted based on two electron density models: NE2001 (Cordes & Lazio, 2002) and YMW16 (Yao et al., 2017). Based on this comparison, the event is classified as “Extragalactic”, “Ambiguous” or “Galactic”. Uncertainties in the measured and predicted DMs are taken into account while performing the comparison.

The L3 stage also determines which action should be triggered by L4 based on the event classification. These actions include storing the event in the database, saving intensity and baseband data for the event to disk or sending an alert through the Virtual Observatory Events (VOEvent) framework (Petroff et al., 2017) to enable multi-wavelength follow-up

---

<sup>2</sup>Rotating radio transients are neutron stars that sporadically emit single pulses (McLaughlin et al., 2006).

<sup>3</sup><https://www.atnf.csiro.au/research/pulsar/psrcat/>

<sup>4</sup>RRATalog; <http://astro.phys.wvu.edu/rratalog/>

<sup>5</sup><https://www.frbcat.org>; <https://www.wis-tns.org>

observations.

### 2.2.3 L4: Action Implementation and Event Archiving

The L4 stage implements the actions determined by L3 for each event. Firstly, L4 hosts a database which saves the information for all events (RFI and astrophysical) and assigns each event a unique ID. The database uses the Python Django framework<sup>6</sup> with the constituent tables including the L1 headers and the refined parameters based on multi-beam detections (L2 event). The locations of different data products associated with each event are also available in this database.

The L4 stage also requests baseband and intensity data from the memory buffers at the L0 and L1 stages, respectively. Data dumps are triggered only for astrophysical events above a user-defined S/N threshold. This is because the high data rate of the CHIME/FRB system prohibits saving all recorded data to disk. The threshold S/N to trigger intensity and baseband dumps varies between 8 to 10, based on the RFI environment. Despite RFI excision algorithms being employed at several stages of the pipeline, some RFI events can still be classified as astrophysical, with their intensity and/or baseband data written to disk. During months of intense RFI activity, the threshold S/N is increased in order to reduce false positives and keep the data rate manageable.

A web interface allows members of the CHIME/FRB collaboration to access the L4 database and classify the candidate FRBs as RFI or astrophysical based on their dynamic spectra. The intensity data then undergo offline processing to improve the real-time estimates of different burst properties such as DM, width and fluence. The recorded baseband data are used to analyze burst polarization properties (CHIME/FRB Collaboration et al., 2019a), obtain precise localization regions (Bhardwaj et al., 2021) and perform high-time resolution studies (CHIME/FRB Collaboration et al., 2021b).

---

<sup>6</sup><https://www.djangoproject.com/>

### 2.2.4 Synthetic Signal Injection

The injection system simulates FRB signals and can be run in parallel with the CHIME/FRB detection pipeline. Synthetic signals are injected in the real-time data stream and are processed by the different pipeline stages (L1–L4) in the same manner as astrophysical signals. This is done to ascertain the detection biases against bursts with different properties. Determining the CHIME/FRB selection function is important to study the intrinsic distributions for different properties of the FRB population.

The injection system is described in detail by [CHIME/FRB Collaboration et al. \(2021a\)](#). In summary, synthetic signals are generated with the temporal and spectral resolution of the CHIME/FRB system using the `simpulse`<sup>7</sup> library. The properties of the simulated signals, such as DM, pulse width, spectral index and scattering timescale, are each drawn from an initial probability density function which samples the full parameter space. Instrumental effects such as dispersive smearing and the spectral structure introduced due to the response of the primary and synthesized beams are also simulated.

The injection is carried out by one of the 128 L1 nodes, which duplicates data from four randomly-chosen beams adjacent in the N-S direction. The simulated pulses are injected into the duplicated data for the beam in which the event is predicted to be detected with the maximum S/N (based on the beam model). The duplicated data pass through the L1 and L2/L3 stages, at which point the detection parameters are stored in the injection database. The detection S/Ns can then be used to ascertain the detection probability for bursts with given parameters. The selection function for the first catalog of bursts detected with the CHIME/FRB system was determined using the recovered S/Ns for  $\sim 10^5$  injected events ([CHIME/FRB Collaboration et al., 2021a](#)).

---

<sup>7</sup><https://github.com/kmsmith137/simpulse>

## 2.3 The First CHIME/FRB Catalog

The CHIME/FRB real-time pipeline has detected 535 FRBs in its first year of operations (2018 July 25–2019 July 1). These bursts are included in the first CHIME/FRB catalog (CHIME/FRB Collaboration et al., 2021a), hereafter referred to as “Catalog 1”. The catalog includes 474 so-far non-repeating sources and 61 bursts from 18 previously reported repeating sources. The sky distribution of these bursts is shown in Figure 2.5 and the dynamic spectra are shown in Figure 2.6.

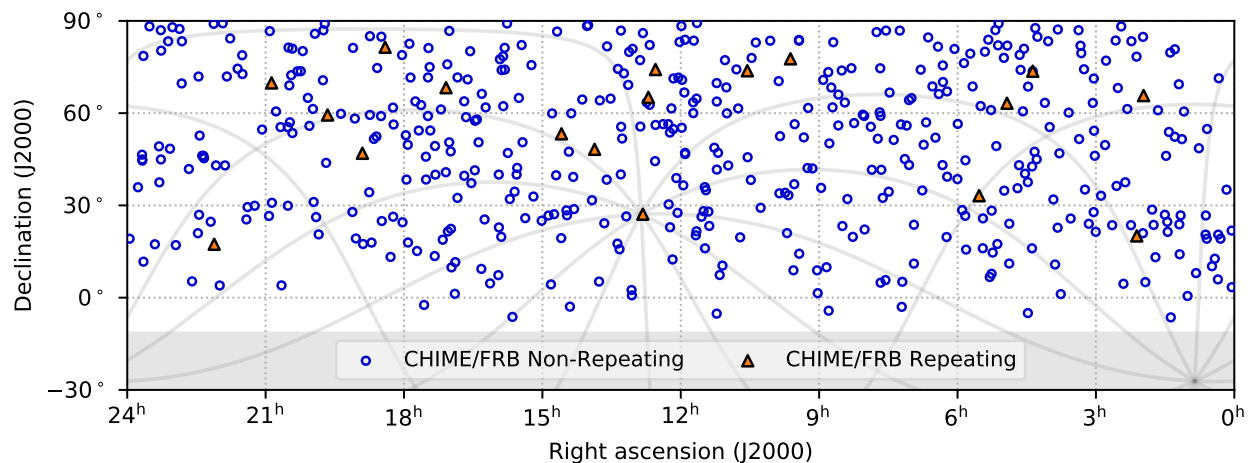


**Figure 2.5:** Sky distribution of 474 so-far non-repeating FRBs and 18 repeating sources included in the first CHIME/FRB catalog. The grey shaded region ( $\delta < -10^\circ$ ) is not observable by the current synthesized beam configuration for the CHIME/FRB system. Lines of constant Galactic longitude and the Galactic plane are plotted in grey. The sources appear to be uniformly distributed as the sky exposure is relatively uniform in the Mercator projection of equatorial coordinates. Figure from CHIME/FRB Collaboration et al. (2021a).

Prior to the release of this catalog,  $\sim 100$  FRBs were known<sup>8</sup>. These FRBs were detected with several different telescopes and/or surveys having distinct selection functions. The CHIME/FRB catalog is thus the largest sample of FRBs detected using the same detection pipeline. Additionally, the catalog selection biases have been inferred using the synthetic signal injection system (see §2.2.4).

The catalog includes distributions of different burst properties, which are derived from

<sup>8</sup><https://www.wis-tns.org>; accessed in August 2021

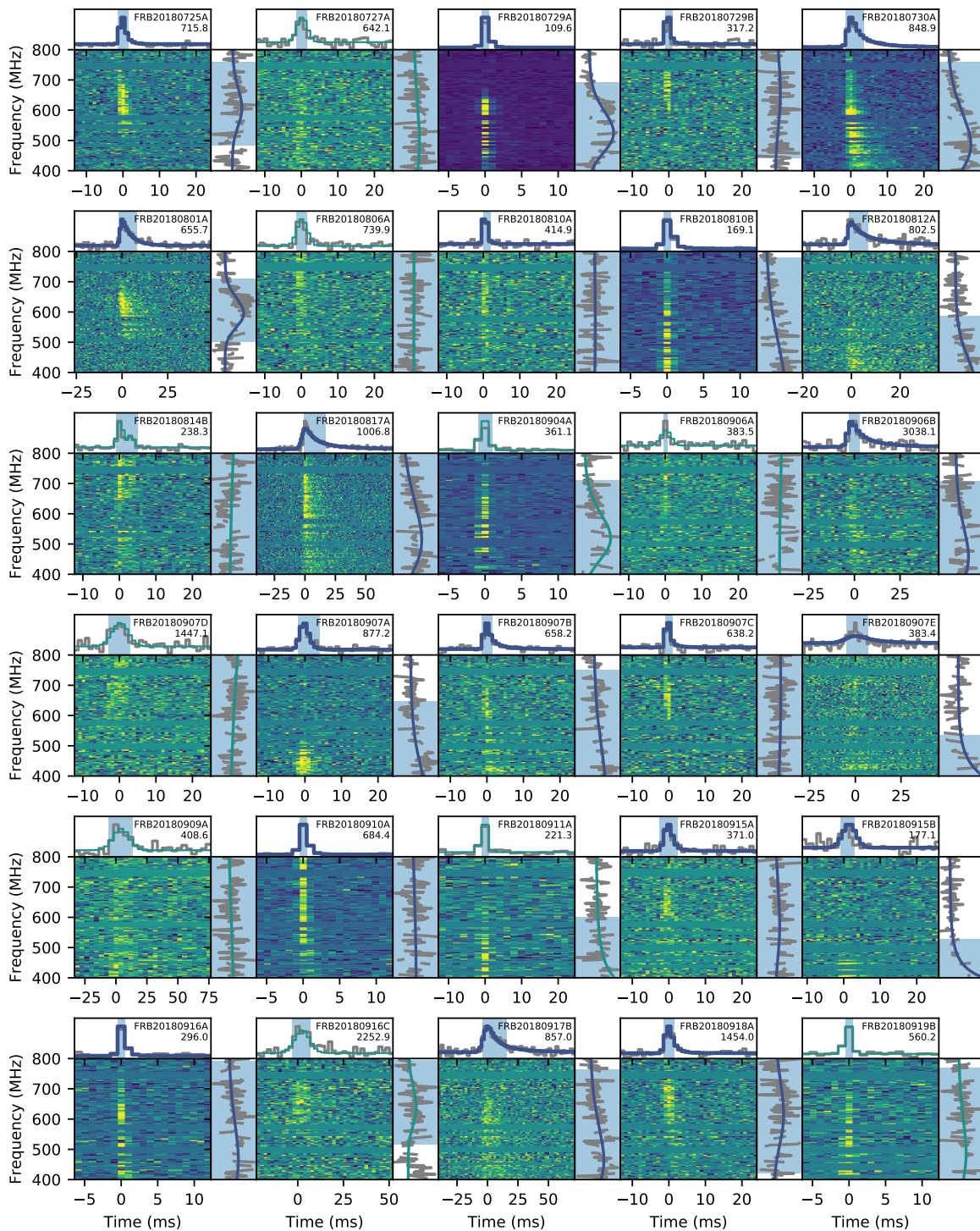


**Figure 2.6:** Dynamic spectra (“waterfall plots”) for a subset of FRBs included in the first CHIME/FRB catalog. The band-averaged time series is plotted on the top of each dynamic spectrum, with the on-pulse spectrum plotted on the right. The blue shaded regions show burst widths and emission bandwidths. The best-fit models are overlaid on the time series and the on-pulse spectra. The models are plotted in blue if the detection of scattering is significant and in green if the scattering is not significant. The best-fit DM for each burst is shown in the top right corner, in units of  $\text{pc cm}^{-3}$ . Figure from [CHIME/FRB Collaboration et al. \(2021a\)](#).

the intensity data recorded for all bursts. Combining the observed distributions with the selection function has enabled determination of the true cosmic distributions for different burst properties. A population synthesis study of the intrinsic distributions of FRB DMs and scattering times is presented in Chapter 5. The catalog also includes information about the overall sky exposure. The algorithms and techniques developed to evaluate the exposure and associated sensitivity variations are discussed in the next chapter.

## Chapter 3

# Determining the Sky Exposure for the CHIME/FRB System

The CHIME telescope observes a strip of sky located along the meridian, covering an area of  $\sim 250$  sq. deg. Due to the rotation of the Earth, the entire sky north of declination,  $\delta \sim -10^\circ$ , transits across this strip over the course of each day. The transit time increases with declination, with the highest exposure to the North Celestial Pole (NCP;  $\delta = 90^\circ$ ). The exposure also depends on where the transit path for a sky location intersects the synthesized beams, with increased exposure for sources whose transit paths cross the beam centres (see §3.1).

Determining the exposure as a function of sky location is essential to meet several science goals of the CHIME/FRB instrument. The first of these goals is the measurement of the all-sky FRB rate, including searches for any variation in the rate with Galactic latitude and observing frequency. Secondly, the daily-cadence observations conducted by the CHIME/FRB system have enabled discovery of repeating FRB sources ([CHIME/FRB Collaboration et al., 2019a,c](#); [Fonseca et al., 2020](#)). In order to characterize the varying activity levels of these repeaters, exposure as a function of both sky location and time is required. Thirdly, determination of the exposure will aid searches for coincident FRB-like emission from sources detected at other wavelengths. As an example, no FRBs were

detected by the CHIME/FRB system at the time of detection of four gamma-ray bursts from SGR 1935+2154 (CHIME/FRB Collaboration et al., 2020b; Curtin, 2021). In order to constrain the radio flux of the magnetar based on these non-detections, it is vital to ascertain whether the CHIME/FRB system was operating nominally at the time of detection of the gamma-ray burst and whether the burst position was in the FOV.

As described in Chapter 2, the CHIME/FRB system relies on the operation of several computing nodes, which run different stages of the pipeline. Determination of the sky exposure requires metrics to be recorded for all computing nodes. These metrics are described in §3.2. Even if all computing nodes are operational at a given time, the pipeline could have reduced sensitivity to FRBs. Some of the potential causes of a loss in sensitivity include contamination from RFI signals, the unavailability of daily gain calibration and a reduction in the number of online X-engine nodes, resulting in missing frequency channels. The daily sensitivity variations are characterized using observations of Galactic pulsars with the CHIME/FRB system, as discussed in §3.3.

The metrics which characterize the system up-time and sensitivity are combined with the CHIME/FRB beam model to generate full-sky exposure maps (see §3.4). These maps are used to evaluate the exposure for the FRB sources in Catalog 1 (see §3.5). To illustrate how the evaluated exposures can be used to characterize FRB repetition rates, a study of the periodic FRB source, FRB 20180916B, is presented in §3.6.

## 3.1 Exposure Definition

In order to compute the exposure, it is necessary to define the synthesized beam area within which a source is considered to be detectable. We define this as the FWHM region at the central observing frequency for CHIME (600 MHz). The synthesized beam FWHM for an FFT telescope in which antennas are arranged in a rectangular grid of length  $l$  is equivalent to that for a single dish with diameter,  $l/0.87$  (Tegmark & Zaldarriaga, 2009). We set

$l = 80$  m as that section of the focal line of each cylinder is outfitted with antennas. The FWHM in the E-W direction,  $\text{FWHM}_{\text{E-W}} = 0.32^\circ$ , as calculated using Equation 2.1 by setting  $D = 80 \text{ m}/0.87$ . The FWHM in the N-S direction varies between beams (see §2.1.4) and is evaluated by dividing  $\text{FWHM}_{\text{E-W}}$  by the cosine of the zenith angle.

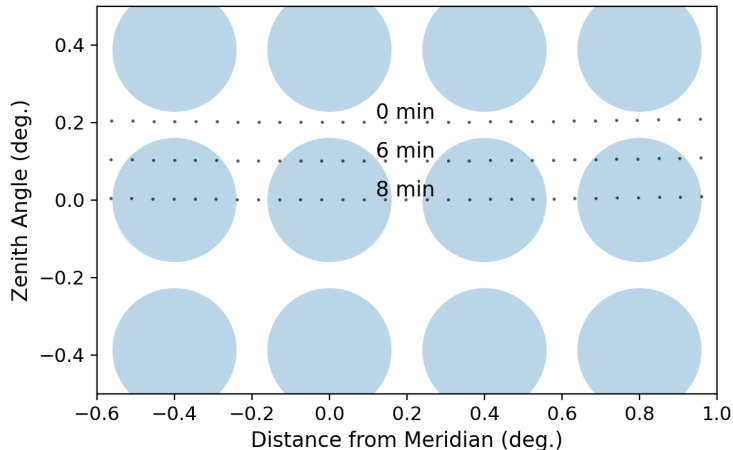


**Figure 3.1:** Transit paths across a subset of the synthesized beams of the CHIME/FRB system. The blue shaded ellipses show the FWHM region of the synthesized beams at 600 MHz. The grey dots trace the transit paths at three different zenith angles (and declinations). A zenith angle of  $0^\circ$  corresponds to  $\delta = 49.32^\circ$ , i.e. the geographic latitude for the CHIME site. The daily exposure within the FWHM region of the four E-W beams is indicated above each transit path. The exposure decreases with increasing distance from the beam centre and reduces to zero for locations which transit between beams.

Since the CHIME/FRB system operates  $24 \times 7$ , the exposure does not vary significantly with right ascension (RA). However, the daily exposure varies with declination as,

$$\Delta t_{\text{transit}}(\delta) = \frac{4 \text{ FWHM}_{\text{E-W}}}{\cos \delta \times 360^\circ} \times 24 \text{ hours.} \quad (3.1)$$

Here  $\text{FWHM}_{\text{E-W}}$  is scaled by  $\cos \delta$  to reflect the beam extent in celestial coordinates while the factor of 4 accounts for the number of synthesized beams in a row. Equation 3.1 is valid for a sky location transiting across the beam centres. Due to the elliptical beam shape, the transit path within the FWHM region shortens with increasing distance from the beam

centre, thereby resulting in reduced exposure (see Figure 3.1). The exposure for a location which transits between two beams is zero as the FWHM regions of the synthesized beams do not have any overlap at a frequency of 600 MHz. We note that a burst can be detected even if its location is outside the FWHM region. Since we have reduced sensitivity to such locations, we do not consider a source as being detectable outside the FWHM region while calculating the exposure.

Sky locations with  $\delta > +70^\circ$  have twice the exposure computed using Equation 3.1 due to their circumpolar nature. Their daily transit path intersects the telescope primary beam twice, as shown in Figure 3.2. The two transits are hereafter referred to as the upper and lower transits, as they occur above and below the NCP, respectively. We report the exposures for these transits separately as the primary and synthesized beam response can vary significantly between the two. The variation in the primary beam response is shown in Figure 3.2.

## 3.2 Pipeline Metrics

Equation 3.1 provides an estimate of the daily exposure for the ideal scenario in which the CHIME/FRB system is operational 100% of the time. In reality, the observations are occasionally interrupted by software upgrades, maintenance activities, power outages and thermal shutdowns. For any sky location, only the fraction of the transit duration for which the real-time pipeline is fully operational is included in the exposure. The pipeline is defined as being fully operational if the L1 nodes which process data for the four E-W beams corresponding to the transit are online. The L2/L3 and L4 stages should also be operating nominally with intensity data being written to disk. The pipeline downtime is estimated by recording metrics for the different stages.

As described in §2.2.1, each L1 node is designated to process data for eight synthesized beams which are adjacent to each other in the N-S direction. It is possible that one of these

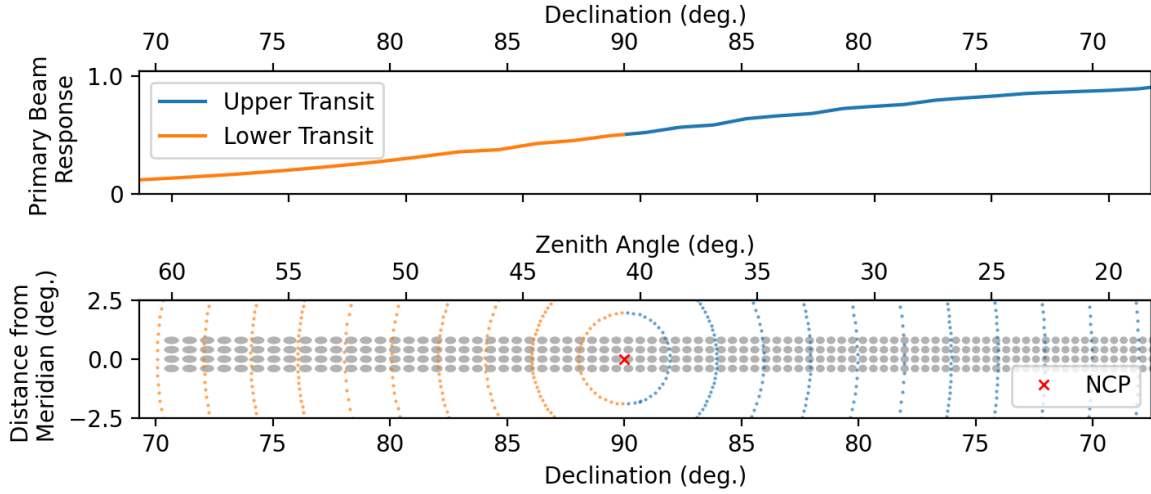


**Figure 3.2:** Primary beam response and transit paths for sources circumpolar for the current synthesized beam configuration of the CHIME/FRB system. The top panel shows the primary beam response along the meridian averaged over all frequency channels and normalized to the response at a zenith angle of  $0^\circ$ . The response is derived by fitting a model describing the cross-talk between feeds to observations of 37 bright point sources (CHIME/FRB Collaboration et al., 2021a). For the same declination, the response can differ significantly between the upper and lower transits. The blue and orange dots in the bottom panel trace the upper and lower transit paths, respectively, for different declinations. The grey shaded ellipses show the beam FWHM regions at 600 MHz.

nodes is offline while the rest of the system is operating nominally. In this scenario, the exposure for sky locations transiting across the beams processed by this node will be equal to 75% of the transit duration. Therefore, metrics need to be recorded separately for each synthesized beam.

The state (on/off) of all synthesized beams is recorded at the time of detection of each event, regardless of its classification (astrophysical or RFI). The state is recorded at a cadence of a few minutes as that is the maximum temporal separation between consecutive events. The information is stored with a timestamp in the L4 database (see §2.2.3). We have developed a Python suite for exposure determination, which includes a script that queries the L4 database to determine the downtime for different beams.

The L2/L3 and L4 stages run on separate computing nodes. We manually monitor the two nodes every few hours to check if they are running nominally. In order to prevent

overestimation of the exposure due to human errors, automated checks are also performed. Firstly, a Python script fetches timestamps of astrophysical and RFI events ( $S/N > 7.5$ ) from the L4 database. If no event is detected within a three-hour interval, the L2/L3 stage is assumed to be offline. Another script checks whether callback data are saved to disk for all events which fit the callback criteria (see §2.2.3). If the callback data for an event are not available, then the L4 stage is assumed to be offline from the time of detection of the event to that of a subsequent event for which callback data are available. While this criteria is overly conservative, it does not result in a significant underestimation of the exposure. Even after adopting this criteria, the downtime of the L4 stage amounted to  $< 2\%$  of the total exposure during the first year of operations.

### 3.3 Sensitivity Variations

Although the daily exposure to a sky location remains constant (provided all computing nodes are operating nominally), the sensitivity can vary on a day-to-day basis. The variation could arise due to the lack of an optimal gain calibration. The calibration is performed once every sidereal day during the transit of a bright point source such as Cyg A (see §2.1.4). A bad calibration could be the result of the calibrator data being heavily contaminated by RFI. Alternately, if the system is offline during the calibrator transit, then the calibration from the previous day is used, which might be non-optimal.

Other factors that could result in reduced sensitivity include missing frequency channels and inefficiencies in the search pipeline. As an example, the L2/L3 stage can misclassify some astrophysical events if the RFI activity is significantly higher than usual. The number of frequency channels which are excised by the L1 RFI masking routine (§2.2.1) could also increase during times of high RFI activity. A variation in the number of online L0 nodes can also cause the number of recorded frequency channels to vary as each node processes 64 channels (of a total of 16384).

It is difficult to accurately model the magnitude of the variation in sensitivity due to each of the aforementioned effects. While the sensitivity can be estimated using the visibilities produced by the X-engine (see §2.1.3), such an estimate would only account for the variation due to offline L0 nodes and unavailability of an optimal gain calibration. Since the visibilities are recorded at a cadence of  $\sim 20$  s (CHIME/FRB Collaboration et al., 2018), they are not sensitive to RFI signals of millisecond duration which negatively impact the detection efficiency of the FRB search pipeline.

Another way to characterize the sensitivity variations is to inject synthetic signals into the real-time pipeline and monitor their detection statistics. As described in §2.2.4, a signal injection system has been implemented with the first sample of simulated pulses injected in August 2020 (CHIME/FRB Collaboration et al., 2021a). However, the system does not yet perform injections throughout the observations.

In the absence of continuous injections, we estimate the sensitivity variations using single pulses from Galactic pulsars which are detected by the same real-time detection pipeline as the FRB sample. The method is described in the following subsections. While we developed this method to ascertain the daily sensitivity variations at the location of FRB 20121102A (Joseph et al., 2019), we subsequently used it for 17 repeating FRBs (CHIME/FRB Collaboration et al., 2019a; Fonseca et al., 2020) and all the sources in Catalog 1. Since we use the catalog sources to illustrate the exposure determination process in this chapter, the sensitivity variations are also determined for the Catalog 1 period in this section.

### 3.3.1 Criteria for Pulsar Selection

The pipeline can detect events with DMs  $> 15$  pc cm<sup>-3</sup>, which results in pulses from 200 – 250 known pulsars being detected every day. These pulses are automatically associated with the known pulsars based on their DM and sky location (see §2.2.2). Querying the L4 database with the pulsar name produces a list of detections with their timestamps, inferred

sky locations, detection S/Ns, widths and several other measured parameters.

We identify pulsars which are robustly detected by the CHIME/FRB system on  $>20\%$  of the days in the Catalog 1 period (2018 July 25–2019 July 1). Since the pipeline can occasionally misidentify RFI pulses as originating from a known pulsar, we classify a pulsar detection as robust if at least five  $S/N > 8$  pulses are detected during the daily transit in consideration. We only include pulses detected within the FWHM of the synthesized beams at 600 MHz. This criterion ensures that the sensitivity estimate based on the pulsar detections is valid for the region used for the exposure calculation. We find that 106 known pulsars match these criteria.

### 3.3.2 Estimation of RMS Noise

The RMS radiometer noise for an observing bandwidth of  $\Delta\nu$  is given by the following expression (see, e.g., [Lorimer & Kramer 2004](#)),

$$\Delta S_{\text{sys}} = \frac{T_{\text{sys}}}{G\sqrt{n_p t_{\text{samp}} \Delta\nu}}, \quad (3.2)$$

where  $G$  is the telescope gain (expressed in K/Jy),  $n_p$  is the number of summed polarizations,  $t_{\text{samp}}$  is the sampling time and  $T_{\text{sys}}$  is the system temperature. The system temperature is defined as,

$$T_{\text{sys}} = T_{\text{rec}} + T_{\text{sky}} + T_{\text{spill}} + T_{\text{atm}}, \quad (3.3)$$

where  $T_{\text{rec}}$  is the receiver temperature,  $T_{\text{sky}}$  is the sky temperature,  $T_{\text{spill}}$  is the spillover noise contribution from the ground and  $T_{\text{atm}}$  is due to the emission from the Earth's atmosphere. The radiometer equation ([Cordes & McLaughlin, 2003](#)) which relates the observed S/N and

the peak flux density,  $S$ , of a pulse can be expressed in terms of the RMS noise as,

$$S = \frac{S/N T_{\text{sys}}}{G w_i} \sqrt{\frac{w_b}{n_p \Delta \nu}} \quad (3.4)$$

$$= \frac{S/N}{w_i} \Delta S_{\text{sys}} \sqrt{t_{\text{samp}}} \sqrt{w_b}, \quad (3.5)$$

where  $w_i$  is the intrinsic pulse width. The pulse width can be broadened due to instrumental and propagation effects and is defined as,

$$w_b = \sqrt{w_i^2 + t_{\text{samp}}^2 + t_{\text{chan}}^2 + \tau^2}, \quad (3.6)$$

where  $t_{\text{chan}}$  is the intrachannel dispersive smearing (see §2.1.5) and  $\tau$  is the scattering time.

In order to determine the RMS noise using Equation 3.4, a pulse with known flux density must be detected by the real-time pipeline. Although the mean flux density of the selected pulsars is available in the ATNF Pulsar Catalogue<sup>1</sup>, the flux density of their single pulses can exhibit significant variations. These variations can be stochastic in nature or arise due to propagation effects such as scintillation (§1.2.2) and phenomena such as mode-changing or nulling (see, e.g., [Backer 1970](#)). The magnitude of the variations ranges from 5 – 100% ([Burke-Spolaor et al., 2012](#)), hinting at the possibility that the CHIME/FRB system is only detecting the tail of the flux density distribution of each pulsar. Therefore, the catalogued fluxes might not be representative of the average flux of the single pulses detected with the CHIME/FRB system, prohibiting an estimate of the absolute RMS noise using Equation 3.4.

Although it is not possible to determine the absolute RMS noise, we can estimate the relative RMS noise. The method relies on the assumption that the average flux density of the pulses which are detected by the CHIME/FRB system does not change with time. We

<sup>1</sup><https://www.atnf.csiro.au/research/pulsar/psrcat/>

derive an expression for the RMS noise by rearranging the terms in Equation 3.4,

$$\Delta S_{\text{sys}} = \underbrace{\left\{ \frac{w_i}{S/N\sqrt{w_b}} \right\}_{\text{median}}}_{\text{Quality Factor}} \frac{S_{\text{median}}}{\sqrt{t_{\text{samp}}}}. \quad (3.7)$$

Assuming that the median flux density of the CHIME/FRB-detected pulses for each pulsar,  $S_{\text{median}}$ , is stable in time, the variation in the RMS noise would be proportional to the variation in the quality factor.

We start by estimating the daily quality factors for each of the 106 pulsars. We compute  $w_i/(S/N\sqrt{w_b})$  for each pulse which meets the criteria listed in §3.3.1. Since the pipeline does not measure the intrinsic pulse width, we set  $w_i = w_b$  while evaluating the aforementioned factor. As we are only interested in the relative RMS noise, this assumption should not affect our results as long as the broadened width is equal to the intrinsic width multiplied by a constant factor. This is well motivated as the two width components,  $t_{\text{samp}}$  and  $t_{\text{chan}}$ , are constant, and the scattering time is not expected to change significantly between detections for most pulsars.

For each pulsar, the quality factor is equal to the median of  $w_i/(S/N\sqrt{w_b})$  for all pulses detected during the daily transit. We normalize the daily quality factors by dividing them by the median over all days on which the pulsar was detected. To ensure that the estimate of the quality factor is largely unaffected by the assumption of a constant median flux for each pulsar, we average over the quality factors for all pulsars detected on each sidereal day for which the system was operating with the same gain calibration. While the median flux for a single pulsar could vary on a day-to-day basis, these variations would not be correlated across a large sample of pulsars. Therefore, the average daily quality factor provides a robust measurement of the relative RMS noise.

While averaging, we choose a sidereal day over a UTC day in order to be sensitive to the variation in the RMS noise due to the changing gain calibration. We perform a weighted average with the weights being equivalent to the standard deviation of  $w_i/(S/N\sqrt{w_b})$  for

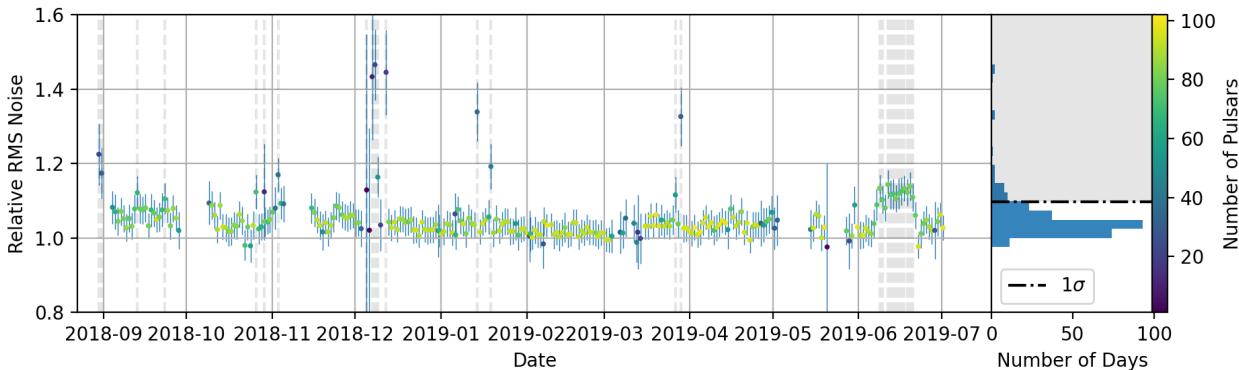


**Figure 3.3:** Daily variation in the RMS noise for the CHIME/FRB system during the Catalog 1 period. The plotted RMS noise is the weighted average of the measurements from a sample of 106 pulsars detected using the real-time pipeline. No measurements are available for days with zero exposure. The number of pulsars used for the noise estimate for each sidereal day is indicated by the coloured markers. Days for which the RMS noise exceeds the median by more than  $1\sigma$  are excised from the total exposure and are indicated by the grey dashed lines. A histogram of the estimated RMS noise values is shown in the right panel. The black line indicates the  $1\sigma$  threshold above which a day is classified as having low sensitivity and excised from the exposure.

each pulsar. This ensures that the pulsars which have less variation in their detected S/Ns and are thus better predictors of the sensitivity dominate the resulting estimate. The error on the weighted mean accounts for the scatter in the detected S/Ns for each pulsar as well as the variation in the measurements from different pulsars. The inferred relative RMS noise and the associated uncertainties are shown in Figure 3.3.

### 3.3.3 Excision of Low Sensitivity Periods

The CHIME/FRB system is less sensitive to FRBs on days with high inferred RMS noise. These days need to be excluded from the on-sky exposure. This is to ensure that the all-sky FRB rate and source repetition rates evaluated using the exposure are not underestimated. We excise days for which the relative RMS noise exceeds the median in the Catalog 1 period by more than  $1\sigma$ . A histogram of the RMS noise values in this period is shown in Figure 3.3 and the  $1\sigma$  excision threshold is indicated. An average of 1.5 FRBs per day is detected on the excised days as compared to 2.4 FRBs on days with nominal sensitivity. Although

the choice of  $1\sigma$  for the excision threshold is arbitrary, the difference in FRB detection rates between the excised and non-excised days validates this choice.

A total of 28 sidereal days are excised, which amount to 7% of the total on-sky exposure in the Catalog 1 period. Twenty three of the 535 FRBs in the catalog were detected on these days. These FRBs are excluded from any population studies as the selection function could be significantly different for the excised intervals.

The exposure in the pre-commissioning phase of the CHIME/FRB project (2018 July 25–2018 August 27) is also excluded. This is because the N-S extent and E-W spacing of the synthesized beams in the pre-commissioning phase were different than those for the current configuration (see §2.1.4). This resulted in the two beam configurations having significantly different primary and synthesized beam responses for a given sky location. The exposure in this period is excluded to avoid adding the duration for transits with different sensitivities. The thirteen FRBs detected in this period are also excluded from any population studies.

### 3.4 Full-sky Exposure Maps

The pipeline and sensitivity metrics are used to determine the daily exposure to any sky location. For each day, we generate two maps in the HEALPix format (Górski et al., 2005), which include the exposure for the upper and lower transit, respectively. Each map has  $2 \times 10^8$  pixels, with each pixel covering an area of 0.7 sq. arcminutes. We choose this resolution to ensure that the variation in the exposure with declination (see Figure 3.1) is accurately captured. Figure 3.4 shows the pixel sizes as compared to the extent of the synthesized beams.

In order to determine the exposure for a given day, we generate timestamps at a cadence of 4 s and query the pipeline metrics at these times. Although the metrics are currently reported at a cadence of a few minutes to an hour (see §3.2), we choose a resolution of 4 s as the metrics will be recorded at this cadence in the future. We exclude time stamps for

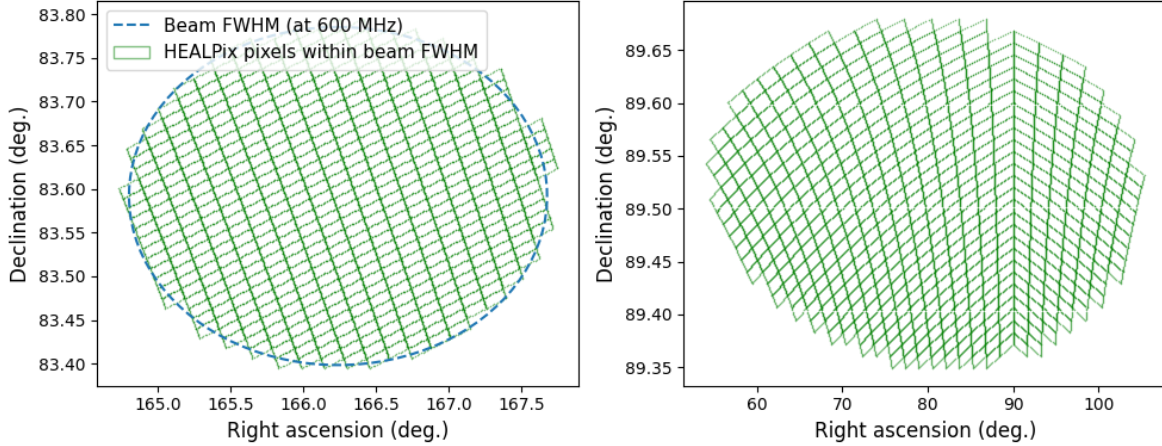


**Figure 3.4:** Sky area in celestial coordinates observed by two synthesized beams at a randomly chosen time. The FWHM region at 600 MHz is shown by the blue dashed ellipse in the left panel. The pixels of the HEALPix exposure map which lie within the FWHM region and thus have non-zero exposure are shown by the green rectangles. The beam FWHM in RA varies as  $\cos^{-1}\delta$  and thus increases with declination, as shown in the right panel. The FWHM region cannot be parameterized as an ellipse in the celestial coordinate system for  $\delta > \sim +89^\circ$ . The RAs of the beam centres in the two panels are randomly chosen, with the beam extent in RA being the same for any value of the central RA.

which the L2/L3 and L4 stages of the pipeline were offline or the system had high relative RMS noise. We determine which sky locations are being observed by the active synthesized beams for the remaining timestamps.

The beam positions,  $(x_{\text{beam}}, y_{\text{beam}})$ , are defined in the telescope frame of reference, where  $x$  is the distance from the meridian in the E-W direction and  $y$  is the zenith angle. We convert the beam positions to celestial coordinates  $(\text{RA}_{\text{beam}}, \delta_{\text{beam}})$  based on the time and the latitude for the CHIME site. For each timestamp, we determine which pixels of the HEALPix map are within the FWHM region of the synthesized beams, as illustrated in Figure 3.4. A pixel has non-zero exposure if its central coordinates,  $(\text{RA}_{\text{pixel}}, \delta_{\text{pixel}})$ , satisfy the condition for a point lying within an ellipse,

$$\frac{(\text{RA}_{\text{pixel}} - \text{RA}_{\text{beam}})^2}{(0.5 \text{ FWHM}_{\text{E-W}} / \cos \delta)^2} + \frac{(\delta_{\text{pixel}} - \delta_{\text{beam}})^2}{(0.5 \text{ FWHM}_{\text{N-S}})^2} < 1. \quad (3.8)$$

Here the FWHM in RA is obtained by dividing  $\text{FWHM}_{\text{E-W}}$  by  $\cos \delta$  (see Equation 3.1).

The FWHM region cannot be parameterized as an ellipse in celestial coordinates for  $\delta > +89^\circ$ , as shown in Figure 3.4. For these declinations, the celestial coordinates for the pixels and beam centres are converted to vectors, by assuming that the pixels and beams are located on the surface of a unit sphere. The Cartesian components of the vectors are then compared to check whether a pixel lies within the FWHM region.

For each timestamp, a duration of 4 s is added to the total exposure of the pixels which lie within the FWHM region of the active beams. The exposure map for each day is generated by iterating over all timestamps. The daily maps are co-added to obtain the total exposure for the Catalog 1 period. The map for the Catalog 1 period is shown in Figure 3.5 with the exposure for the circumpolar locations ( $\delta > +70^\circ$ ) plotted separately.

The up-time for the synthesized beams in the Catalog 1 period was 236211 beam days, amounting to a total exposure of 230.7 days after dividing by the number of beams. We estimate an observing time of 210 days after excluding the downtime of the L2/L3 and L4 stages and the low-sensitivity days. The estimated exposure was used by [CHIME/FRB Collaboration et al. \(2021a\)](#) to determine the all-sky FRB rate based on the Catalog 1 sample. Additionally, the full-sky exposure maps were used to determine CHIME/FRB’s exposure to Galactic pulsars and RRATs ([Good et al., 2020](#)) and rule out a dependence of the FRB rate on Galactic latitude ([Joseph et al., 2021](#)).

### 3.5 Source Exposures

The full-sky maps can also be used to determine the exposure for the FRBs included in Catalog 1. All but two sources<sup>2</sup> included in the catalog have localization regions spanning tens of arcminutes. The localization region for one of these sources is shown in Figure 3.6. Since these regions are larger than the pixels in the exposure maps, the exposure needs to be averaged over all the pixels which lie within the localization region.

---

<sup>2</sup>The repeating FRB sources, FRB 20121102A and FRB 20180916B, have been localized with sub-arcsecond precision ([Chatterjee et al., 2017](#); [Marcote et al., 2020](#)).

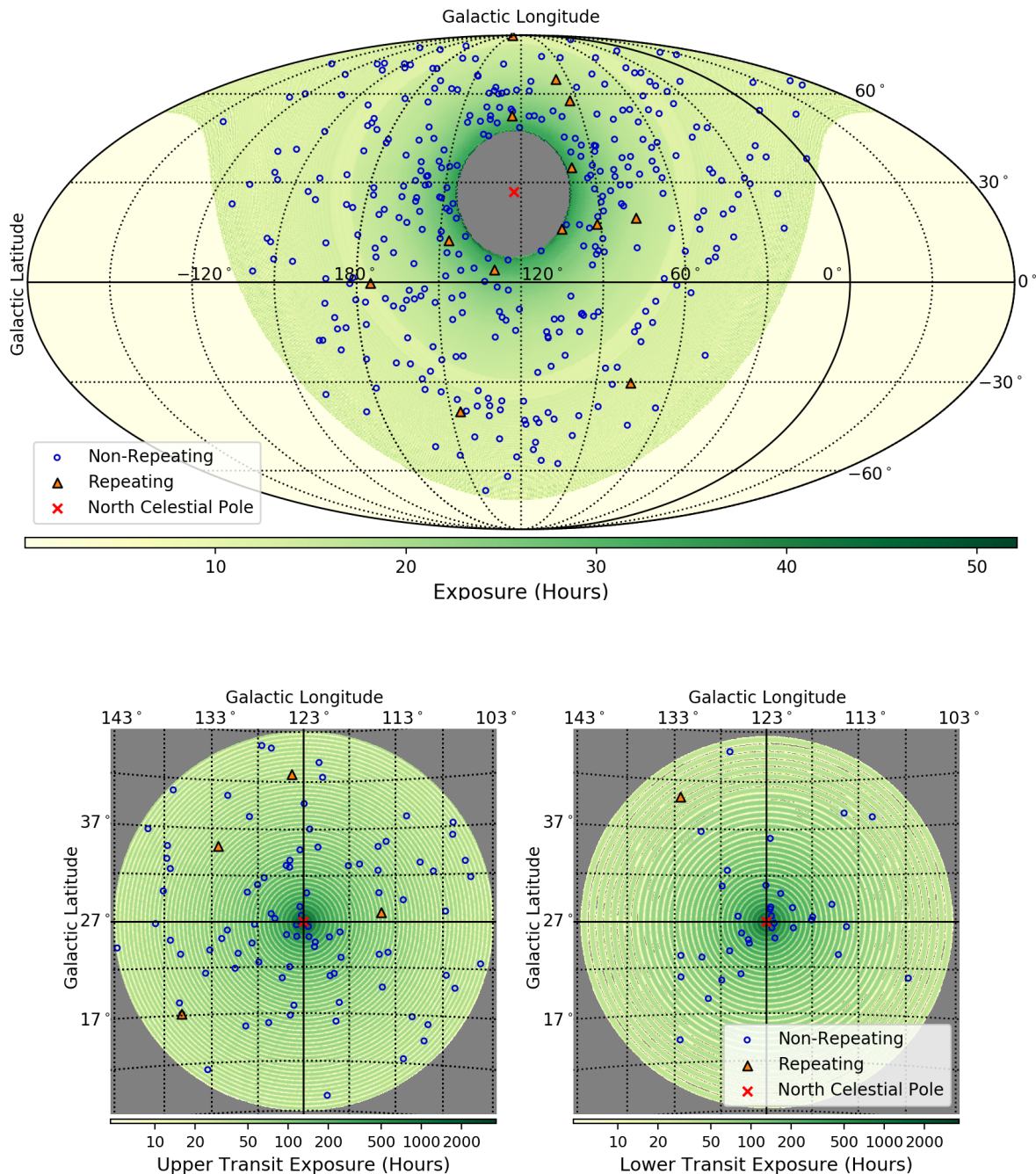


**Figure 3.5:** Sky maps in Galactic coordinates with locations of all repeating and non-repeating sources in the catalog overlaid on the total exposure in the period from 2018 August 28 to 2019 July 1. The top panel shows sky locations that transit across the primary beam of the telescope once per day ( $\delta < +70^\circ$ ) while the bottom panels show upper and lower transit exposures for the circumpolar sources ( $\delta > +70^\circ$ ). Maps in the bottom panel are centred on the NCP and have a logarithmic colour scale. Despite comparable exposure for the two transits, there are fewer FRB detections in the lower transit due to reduced sensitivity of the primary beam as compared to the upper transit. The concentric circular patterns arise due to regions between synthesized beams having zero exposure. Figure made by the author and reproduced from [CHIME/FRB Collaboration et al. \(2021a\)](#).

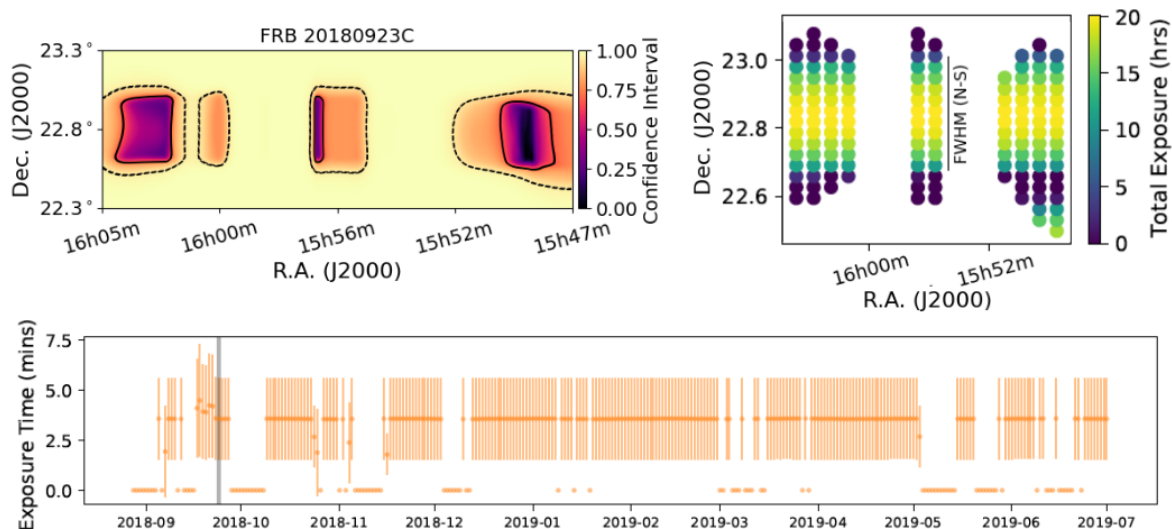


**Figure 3.6:** Localization region and exposure timeline for one of the catalog sources, FRB 20180923C. The left panel is reproduced from [CHIME/FRB Collaboration et al. \(2021a\)](#) and shows the uncertainty in the sky position of this source. The colour scale represents the confidence intervals for the localization with the solid and dashed contours enclosing the 68% and 95% confidence regions, respectively. The right panel shows the exposure in the Catalog 1 period determined for a coarse grid of positions within the 90% confidence localization region. The N-S extent of the synthesized beams that the source transits through is shown by the grey line. The bottom panel shows the daily exposure to the source, obtained by performing a weighted average over the localization region. The increase in exposure from its typical value for some of the days is due to the occurrence of two transits in the same solar day caused by the length of a solar and a sidereal day being slightly different. The day on which the source was detected is indicated by the grey line.

To compute the exposure for a source, we generate a uniform coarse grid of positions within its 90% confidence localization region. The exposure for each of these positions is determined using the exposure maps, as illustrated in Figure 3.6. We then compute the weighted average of the exposure over all grid locations, with the weights being equal to the probability of the source being located at a particular position. The weighted mean and standard deviation of the exposure for all catalog sources is shown in Figure 3.7. The exposures are also provided in a machine-readable format as part of the Catalog 1 data release.

We do not report any uncertainties on the exposure for the two sources with sub-arcsecond localizations, FRB 20121102A and FRB 20180916B. The exposures for all other sources have

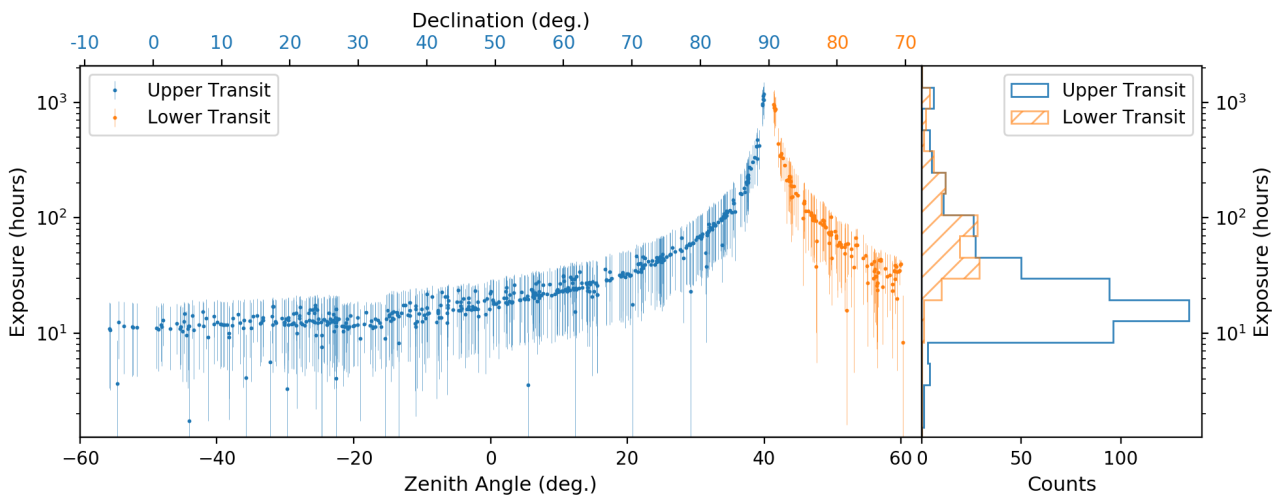


**Figure 3.7:** Upper and lower transit (if observable) exposures for sources included in the first CHIME/FRB catalog. The exposures are plotted as a function of declination ( $\delta$ ) and zenith angle. Errors on the exposure are due to uncertainties in source declinations (see §3.5). The reduced mean exposure for sources with declinations between  $27^\circ$  and  $34^\circ$  is due to a time-limited failure of one of the four CPU nodes designated to process data for this declination range. Some sources have lower exposure than the average for their declination range due to a significant fraction of their localization regions lying outside the FWHM region of the synthesized beams. A histogram of the estimated exposures is plotted in the right panel. Figure made by the author and reproduced from [CHIME/FRB Collaboration et al. \(2021a\)](#).

large uncertainties due to the uncertainty in the source declination being comparable to the beam FWHM, as shown in Figure 3.6. Since the exposure is dependent on the distance from the beam centre, it varies significantly over a localization region which spans the beam FWHM.

The fluence threshold associated with the exposure for each source is also reported in the catalog. The median threshold for all sources is  $\sim 5$  Jy ms. An initial estimate of the threshold is obtained using the measured fluence and S/N of each source. This is done by scaling the measured fluence by the ratio of the burst S/N and the S/N threshold for the real-time pipeline. However, this initial estimate does not account for the daily sensitivity variation (see §3.3) and the variation in the beam response across the transit path and the observing bandwidth. These effects are accounted for in a Monte Carlo simulation, the details of which are provided in [Joseph et al. \(2019\)](#).

## 3.6 FRB Repetition Rates

Prior to the commissioning of the CHIME/FRB system, only one repeating FRB source was known (FRB 20121102A; Spitler et al. 2016). The continued daily exposure to sky locations with  $\delta > -10^\circ$  has enabled the CHIME/FRB system to discover 18 repeating sources in the first year of operations. The techniques discussed in this chapter have been used to characterize the exposure to these sources, which is presented in the discovery papers (CHIME/FRB Collaboration et al., 2019a,c; Fonseca et al., 2020).

The estimated exposures can be used to determine repetition rates and characterize the variation in source activity with time. Studies of the activity levels of repeating FRBs can provide evidence for clustering of bursts, resulting in constraints on the emission mechanism and/or progenitor models. Additionally, such studies can inform the observing strategy for follow-up observations. A study characterizing the periodic modulation in the activity of one of the repeating sources, FRB 20180916B, is described below.

### 3.6.1 FRB 20180916B

The repeating FRB source, FRB 20180916B<sup>3</sup>, is one of the closest localized FRBs, having been localized to a star-forming region in a massive spiral galaxy at  $z = 0.0337 \pm 0.0002$  (Marcote et al., 2020). It is also the first FRB source which was found to exhibit a periodic modulation in its activity. The periodicity of  $16.35 \pm 0.15$  days was discovered by analyzing the arrival times of 38 bursts detected in a span of 1.5 years with the CHIME/FRB system (CHIME/FRB Collaboration et al., 2020a). The folded profile (number of detections as a function of phase) at the 16.35-day period showed deviations from a uniform distribution at  $> 4.5\sigma$  level, based on a  $\chi^2$  test.

To exclude the possibility that the periodicity is instrumental, it is necessary to check if the exposure and/or sensitivity to the source exhibits periodic variations. To check for such trends, we determine the exposure and relative RMS noise for the source using the techniques

---

<sup>3</sup>Formerly known as FRB 180916.J0158+65.

described in earlier sections. These parameters along with the arrival times of the bursts are shown in Figure 3.8. The bursts are detected within a  $\pm 2.7$ -day interval around the epochs of peak activity. There is significant exposure and nominal sensitivity during the inactive periods of the source, which rules out an instrumental origin for the periodicity.

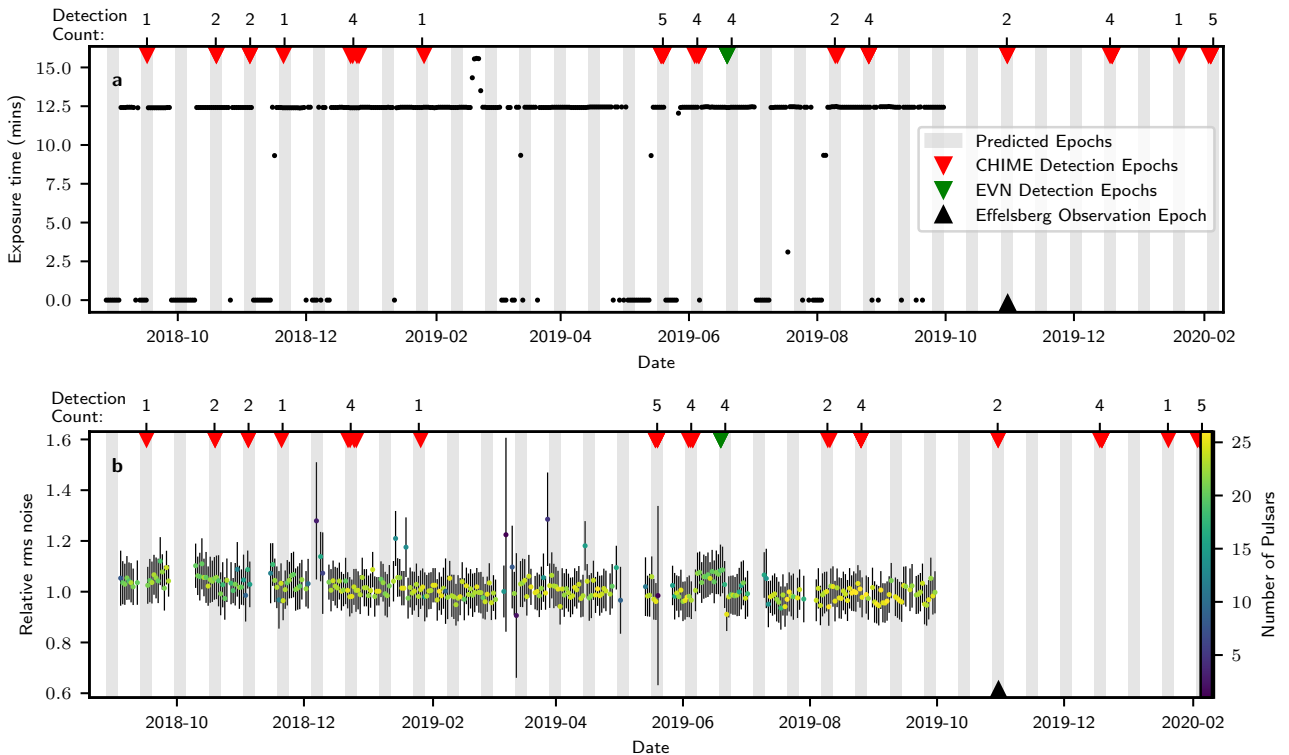


**Figure 3.8:** Timeline of CHIME/FRB’s daily exposure to FRB 20180916B. The black markers in the top panel show the exposure to the source within the FWHM of the synthesized beams at 600 MHz. Downward triangle markers indicate arrival times for detections with CHIME/FRB or the European VLBI Network (EVN) with the number of detections in each active phase indicated above these markers. The upward triangle marker indicates the epoch of non-detection of the source by the Effelsberg telescope. The grey shaded regions show a  $\pm 2.7$ -day interval around estimated epochs of source activity. The bottom panel shows the variation in the daily relative RMS noise at the position of FRB 20180916B, measured using a collection of pulsars detected by CHIME/FRB. The associated  $1\sigma$  uncertainties are also plotted. Figure made by the author and reproduced from [CHIME/FRB Collaboration et al. \(2020a\)](#). The reported exposure is truncated on 2019 September 30 as the relevant metrics were unavailable at the time the paper was published.

Although we confirm that the periodicity is astrophysical, the observed period could be different from the true period due to instrumental effects. Since the CHIME/FRB system

observes the source once every sidereal day (0.99727 solar day), it is possible that the true period is a higher-frequency alias of the observed 16.35-day period. The true frequency can be expressed as  $f_N = N f_{\text{sid}} \pm f_0$ , where  $N$  is an integer,  $f_{\text{sid}} = (0.99727 \text{ day})^{-1}$  and  $f_0 = (16.35 \text{ day})^{-1}$ . To determine if the value of  $N$  differs from zero, the source needs to be observed with a telescope with a different exposure function<sup>4</sup>. Nevertheless, in order to compute the source repetition rate, we assume that  $N = 0$ , i.e. period is 16.35 days.

The exposure for the source in the interval from 2018 August 28 to 2019 September 30 was 64 hours, with a total of 26 bursts being detected during this period. The total exposure for the active phases, defined as  $\pm 2.7$ -day intervals around the epochs of peak activity, was 21 hours. Nineteen of the 26 bursts were detected during the transits included in the exposure. Based on this information, we determine that the repetition rate during the active phases is  $0.9^{+0.5}_{-0.4}$  bursts per hour above a fluence threshold of 5.2 Jy ms. The uncertainties on the burst rate represent the 95% confidence interval, assuming Poisson statistics. We exclude six bursts as they were detected when the source was not within the FWHM regions used for the exposure calculation. Another burst was excluded as it was detected on a day when the pipeline metrics were not being recorded.

The total exposure during the inactive periods was 43 hours. Based on this exposure, we place a 95% confidence upper limit on the repetition rate during the inactive phases of 0.07 bursts per hour. The burst rate during the active and inactive phases is inconsistent at the  $2\sigma$  level, further validating the detection of the periodicity.

Using the exposure information, we can also check whether the source activity is constant within the active phase. In order to do this, we divide the  $\pm 2.7$ -day interval into three sub-intervals of equal duration. The exposure of the CHIME/FRB system in each of these sub-intervals was 7 hours. Thirteen of the 19 bursts were detected within a  $\pm 0.9$ -day interval around the epochs of peak activity, with the repetition rate being  $1.8^{+1.3}_{-0.8}$  bursts per hour in this sub-interval. Five bursts were detected during the second sub-interval, i.e. the duration

---

<sup>4</sup>The possibility of the 16.35-day period being an alias of the true period has been ruled out using observations with the Apertif telescope, which covered the full activity cycle (Pastor-Marazuela et al., 2020).

between 0.9 and 1.8 days of the epochs of peak activity, resulting in a burst rate of  $0.8_{-0.5}^{+1.0}$  bursts per hour. The third sub-interval, which covers the rest of the active phase, had a repetition rate of  $0.1_{-0.1}^{+0.6}$  bursts per hour. The rates in the first and third sub-interval are inconsistent at the  $2\sigma$  level, suggesting that the source activity varies during the active phase.

Knowing that the source activity is maximum in a  $\pm 0.9$ -day interval around the epochs of peak activity, we conducted low-frequency observations of the source during these intervals with the Green Bank and LOFAR telescopes. This strategy maximized the chances of detecting repeat bursts, resulting in the detection of seven bursts with the Green Bank telescope. The observations and burst properties are discussed in the next chapter.

## Chapter 4

# Detection of FRB 180916.J0158+65 Down to Frequencies of 300 MHz

The contents of this chapter have previously been published in the article: Chawla et al., 2020, Detection of Repeating FRB 180916.J0158+65 Down to Frequencies of 300 MHz, *The Astrophysical Journal Letters*, 896, L41.

### 4.1 Introduction

Over the past decade, most FRBs have been observed at a frequency of  $\sim 1$  GHz, with one of the sources, FRB 20121102A, also being detected in the 4–8 GHz frequency range ([Michilli et al., 2018](#); [Gajjar et al., 2018](#)). The detection of FRBs by CHIME in the frequency range of 400–800 MHz (see §2.3) has shown that FRB emission extends to lower radio frequencies. With the apparent ubiquity of these bursts above a frequency of 400 MHz, it is surprising that none of the FRB searches conducted in the frequency range of 300–400 MHz (e.g., [Deneva et al. 2016](#), [Chawla et al. 2017](#), [Rajwade et al. 2020a](#)) have detected any FRBs so far.

Observations of FRBs at low frequencies are important to ascertain whether there exists a cutoff or turnover frequency for their emission, which can help constrain proposed emission mechanisms. FRBs could also be rendered undetectable at low frequencies due to a spectral

turnover arising from propagation effects in the circumburst environment or due to scattering (see §1.3.3). Either of these possibilities offers an opportunity to constrain the properties of the circumburst medium using low-frequency detections (CHIME/FRB Collaboration et al., 2019b; Ravi & Loeb, 2019). Additionally, observations in the 300–400-MHz frequency range can enable studies of the frequency dependence of FRB activity, allowing determination of optimal observing strategies for future FRB searches with instruments such as the Low-Frequency Array (LOFAR) and the Murchison Widefield Array (MWA) which have not detected any FRBs so far at frequencies close to 150 MHz (Coenen et al., 2014; Tingay et al., 2015; Karastergiou et al., 2015; Sokolowski et al., 2018).

To detect emission from FRBs at low frequencies, a complementary strategy to blind searches is targeted follow-up of repeating FRBs (e.g., Houben et al. 2019). The repeating FRBs which exhibit periodic modulation in their activity (see §1.3.4) are excellent targets for low-frequency follow-up. This is because the probability of detecting repeat bursts from these sources is higher than that for a source which emits sporadically, provided that the observations are conducted during the predicted activity windows.

The first FRB source which was found to be periodically active was FRB 180916.J0158+65<sup>1</sup> (CHIME/FRB Collaboration et al., 2020b). The source exhibits a 16.35-day modulation in its activity, with bursts being detected in a 5-day-long activity window. Further details about the discovery of the periodicity are presented in §3.6.1. Following this discovery, we conducted observations to search for repeat bursts from this source in the frequency range of 100–400 MHz.

In this chapter, we report on the detection of low-frequency radio emission from FRB 180916.J0158+65 with the 100-m diameter Robert C. Byrd Green Bank Telescope (GBT) and simultaneous observations of the source with the CHIME/FRB instrument and LOFAR. In §4.2, we provide details of observations made with the above-mentioned instruments. In §4.3,

---

<sup>1</sup>The source is referred to as FRB 20180916B in previous chapters. The source name was changed from FRB 180916.J0158+65 to FRB 20180916B due to the establishment of the Transient Name Server (TNS) naming convention (<https://www.wis-tns.org>).

we describe the methodology used to determine burst properties and sensitivity thresholds for these observations. In §4.4, we discuss the frequency dependence of burst activity as well as the implications of the detection of emission at low frequencies from this source. We summarize our conclusions in §4.5.

## 4.2 Observations

### 4.2.1 Green Bank Telescope

We observed the interferometric position of FRB 180916.J0158+65 (RA =  $01^{\text{h}}58^{\text{m}}00^{\text{s}}.0075$ ,  $\delta = 65^{\circ}43'00.3152''$ ; [Marcote et al. 2020](#)), in the period from 2019 November 15 to 2020 January 20, with the GBT at a central frequency of 350 MHz. Data spanning 100 MHz of bandwidth were recorded using the Green Bank Ultimate Pulsar Processing Instrument backend (GUPPI; [DuPlain et al. 2008](#)). We conducted six observations of the source, all of which were within a  $\pm 1.2$ -day interval of predicted epochs of peak source activity ([CHIME/FRB Collaboration et al., 2020a](#)). Details of the observations are provided in Table 4.1 with a timeline shown in Figure 4.1.

In each observation, data for all four Stokes parameters were recorded for 512 frequency channels at a cadence of  $20.48 \mu\text{s}$ . Since the DM of the source was known prior to the observations, data were coherently dedispersed to the nominal DM ( $349.5 \text{ pc cm}^{-3}$ , [CHIME/FRB Collaboration et al. 2019a](#)), thereby increasing search sensitivity by mitigating the effects of intra-channel dispersive smearing.

We downsampled the data to a resolution of  $327.68 \mu\text{s}$  and searched for bursts using the PRESTO software package<sup>2</sup> ([Ransom, 2001](#)). In order to do so, we masked time samples and frequency channels containing RFI using PRESTO’s `rfifind`. This process reduced the usable bandwidth in each observation to  $\sim 80$  MHz due to persistent RFI in the 360–380 MHz frequency range at the telescope site. We then dedispersed the data at a large number of trial

<sup>2</sup><https://github.com/scottransom/presto>

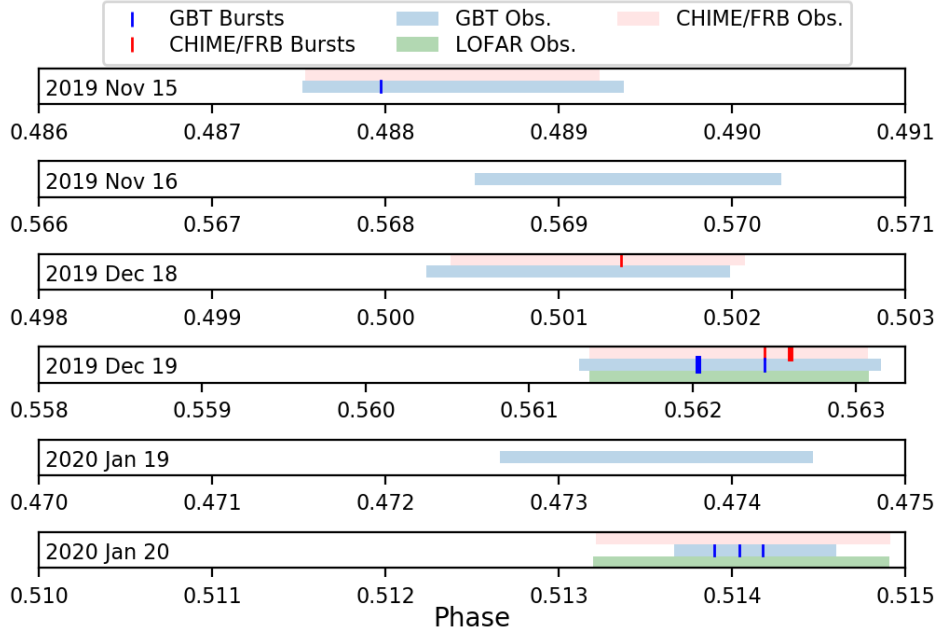


**Figure 4.1:** The exposure of GBT, LOFAR and the CHIME/FRB system for each day of observations as a function of source activity phase (see §4.4.2). The duration of each observation is represented by the shaded regions with the vertical lines marking the burst detection times. Heavy lines represent detection of two bursts.

DMs (in steps of  $0.03 \text{ pc cm}^{-3}$ ) in a narrow range of  $20 \text{ pc cm}^{-3}$  around the nominal DM. Each dedispersed topocentric time series was searched for single pulses (with a maximum width of 100 ms) using the PRESTO-based matched filtering algorithm, `single_pulse_search.py`. We found a total of eight candidate bursts having  $S/N > 7$  in these observations, seven of which were found to be astrophysical after examining their dynamic spectra. The other candidate burst comprised of two narrow-band RFI signals which were observed at different times but were detected with a high  $S/N$  as they coincidentally lined up at the DM of the source. The dynamic spectra of these bursts are shown in Figure 4.2 with the burst properties determined in §4.3.

### 4.2.2 CHIME/FRB Instrument

Four of the six GBT observations were scheduled to coincide with the transit of the source over the CHIME telescope. The repeating FRB 180916.J0158+65 is observable daily for 12 minutes within the FWHM (at 600 MHz) of the synthesized beams of the CHIME/FRB system. Transit of the source over the extent of the primary beam of the CHIME telescope is much longer ( $\sim 40$  minutes). However, sensitivity to the source varies significantly during the primary beam transit.

All CHIME/FRB compute nodes responsible for processing data for the four synthesized beams through which the source transits were operational at the time of the GBT observations. Four bursts from the source were detected by the CHIME/FRB system during these observations (CHIME/FRB Collaboration et al., 2020a), three of which do not have any coincident emission detected with the GBT (see Figure 4.1). However, one of these bursts, with emission in a narrow frequency range of  $\sim 50$  MHz at the bottom of the CHIME band, is found to be associated with the GBT-detected burst 191219C after referencing burst arrival times for both telescopes to the solar system barycentre. We caution that we cannot accurately determine the temporal separation between the two bursts as there could be as-yet-uncharacterized offsets (of the order of  $\sim$ ms) between the timestamps reported by the two backends (GUPPI and CHIME/FRB). However, our current estimate of the separation between the best-fit burst arrival times (see Table 4.2) is  $\sim 23$  ms, which implies that the bursts together constitute emission drifting downwards in frequency — even after correction for dispersion. The phenomenon of downward-drifting sub-bursts (see §1.3.2) has been observed previously for this source as well as for other repeating FRBs (Hessels et al., 2019; CHIME/FRB Collaboration et al., 2019a,c). The dynamic spectra of these bursts are shown in Figure 4.2 with characterization of burst properties and the frequency-drift rate described in §4.3.

Telescope	Obs. Freq. (MHz)	Bandwidth (MHz)	Calendar Date	Start Time (MJD) <sup>a</sup>	Duration (hours)	No. of Detections <sup>b</sup>
LOFAR	150	80	2019 Dec 19	58836.15841	0.67	...
			2020 Jan 20	58868.07083	0.67	...
GBT	350	100	2019 Nov 15	58802.25100	0.73	1
			2019 Nov 16	58803.57524	0.69	...
			2019 Dec 18	58835.15885	0.69	...
			2019 Dec 19	58836.15731	0.73	3
			2020 Jan 19	58867.40803	0.71	...
			2020 Jan 20	58868.07846	0.37	3
CHIME/FRB <sup>c</sup>	600	400	2019 Nov 15	58802.25126	0.67	...
			2019 Dec 18	58835.16114	0.67	1
			2019 Dec 19	58836.15841	0.67	3
			2020 Jan 20	58868.07103	0.67	...

**Notes.**

<sup>a</sup>Reported start times are topocentric at each observing site.

<sup>b</sup>Detections with the CHIME/FRB system have been reported on by [CHIME/FRB Collaboration et al. \(2020a\)](#).

<sup>c</sup>The start time and duration of each observation with the CHIME/FRB system corresponds to the transit of the source across the primary beam of the telescope (see §4.2.2).

**Table 4.1:** Summary of the observations of FRB 180916.J0158+65

### 4.2.3 Low-Frequency Array (LOFAR)

The LOFAR telescope comprises of thousands of antennas located across Europe, with a dense core located in the Netherlands (van Haarlem et al., 2013; Stappers et al., 2011). A group of antennas forms a station and the signals from any subset of these stations can be combined coherently or incoherently. We recorded beam-formed complex voltage data with the high-band antennas of all core stations (24 in number) at 110–190 MHz during the time of two GBT observations in which bursts are detected. This data has a native resolution of  $5.12 \mu\text{s}$  and  $0.195312 \text{ MHz}$ .

All channels were coherently dedispersed to  $350 \text{ pc cm}^{-3}$  using `cdmt` (Bassa et al., 2017), RFI was masked using PRESTO’s `rfifind` and the barycentred start times of the observations were calculated using `sigproc`’s `barycentre` module.

We performed a traditional single-pulse search of the observations, using PRESTO’s `single_pulse_search.py`, split into a high-time resolution and a low-time resolution search. We adopt this strategy to be sensitive to both narrow (similar burst width as in the GBT band) and wide bursts, in case bursts are intrinsically broader at lower frequencies or are broadened by scattering. For the high-time-resolution search, the data were downsampled to  $t_s = 0.65536 \text{ ms}$ , and DMs  $330\text{--}370 \text{ pc cm}^{-3}$  were searched in  $0.005 \text{ pc cm}^{-3}$  steps up to burst widths of  $0.05 \text{ s}$ . For the low-time-resolution-search, the data were downsampled to  $t_s = 20.97152 \text{ ms}$ , and DMs  $330\text{--}370 \text{ pc cm}^{-3}$  were searched in  $0.2 \text{ pc cm}^{-3}$  steps up to burst widths of  $0.3 \text{ s}$ . No bursts were detected with  $S/N > 7$  and  $> 9$ , the noise floors for the high and low-time resolution searches, respectively.

We converted the GBT burst times-of-arrival (TOAs; listed in Table 4.2) to expected TOAs at  $150 \text{ MHz}$  in the barycentric frame and generated  $\sim 20 \text{ s}$  of dynamic spectra around that time, incoherently dedispersed to  $348.82 \text{ pc cm}^{-3}$  (the best measured DM from high-resolution CHIME/FRB data; CHIME/FRB Collaboration et al., 2020a), sub-banded to 200 channels of  $0.390624 \text{ MHz}$  bandwidth each and downsampled to  $1.96608\text{-ms}$  and  $20.97152\text{-ms}$  time resolution. We inspected these dynamic spectra by eye in order to be sensitive to bursts

with potentially narrow ( $\sim 10\text{--}20$  MHz) emission bandwidths and slow frequency drifts, to which a traditional search that sums over the full bandwidth has reduced sensitivity. This burst spectrum is expected from extrapolating burst widths and linear drift rates at higher frequencies down to 150 MHz (Hessels et al., 2019; Josephy et al., 2019). No bursts were found.

A 300-s test observation of pulsar B2111+46 (with a spin period of 1.01 s) was recorded and processed in the way described above (except that it was dedispersed at both the coherent and incoherent dedispersion stage to  $141.3 \text{ pc cm}^{-3}$ ). Pulses were detected in both a by-eye inspection of dynamic spectra and in a blind search, with the expected S/N. As the closest test observation is from 2019 July 30 this gives confidence in the processing pipeline.

## 4.3 Analysis

### 4.3.1 Determination of Burst Properties

We determine burst properties from data which are downsampled to a resolution of  $327.68 \mu\text{s}$  and corrected for the receiver bandpass using the radiometer equation for each frequency channel,

$$\Delta S_{\text{sys},\nu} = \frac{T_{\text{rec}} + T_{\text{sky}}}{G \sqrt{n_{\text{p}} t_{\text{samp}} \Delta \nu_{\text{chan}}}}, \quad (4.1)$$

where  $\Delta S_{\text{sys},\nu}$  is the RMS noise for each frequency channel,  $T_{\text{rec}}$  is the receiver temperature,  $G$  is the telescope gain,  $n_{\text{p}}$  is the number of summed polarizations,  $t_{\text{samp}}$  is the sampling time and  $\Delta \nu_{\text{chan}}$  is the frequency resolution. The GBT's 350-MHz receiver has<sup>3</sup>  $n_{\text{p}} = 2$ ,  $T_{\text{rec}} = 23$  K and  $G = 2 \text{ K Jy}^{-1}$ . The sky temperature at the central frequency of each channel,  $T_{\text{sky}}$ , was estimated using the 408-MHz all-sky map produced by Remazeilles et al. (2015) by assuming a spectral index of  $-2.55$  for Galactic synchrotron emission (Haslam et al., 1982). We calibrate the data by subtracting the off-pulse mean, dividing by the off-pulse

<sup>3</sup><https://science.nrao.edu/facilities/gbt/proposing/GBTpg.pdf>

standard deviation and converting the counts in each frequency channel to a flux density using Equation 4.1. Here we define the on-pulse region (shown in Figure 4.2) as twice the full width at tenth maximum (FWTM) in a Gaussian model fit to the band-averaged time series.

Using the calibrated data, we estimate burst DMs with the `DM_phase` package<sup>4</sup> (Seymour et al., 2019) which has previously been used to characterize FRBs with complex morphologies, particularly those with downward-drifting sub-bursts. For each burst, the algorithm estimates the optimal DM based on whether the coherent power over the emission bandwidth, and hence the burst structure, is maximized. The measured DMs (see Table 4.2) for all but two GBT detections are consistent within  $1\sigma$  uncertainties with the average DM of  $348.82 \text{ pc cm}^{-3}$  measured for the source using complex voltage data recorded by the CHIME/FRB system (CHIME/FRB Collaboration et al., 2020a). The DMs of the other two detections, 191115 and 191219C, although higher, are consistent with the average source DM at the  $3\sigma$  level. We note that measurements can be biased high if drifting sub-structure within bursts is unresolved at the time resolution used for obtaining the best-fit DM.

We also fitted models of dynamic spectra to all calibrated GBT bursts for estimating component widths and scattering timescales, using the same least-squares algorithm employed in previous CHIME/FRB analyses (CHIME/FRB Collaboration et al., 2019a,b,c; Fonseca et al., 2020). For all modelling, we held the DM fixed to the values listed in Table 4.2 while fitting six parameters that describe a pulse broadening function – the convolution of a Gaussian temporal profile with a one-sided exponential decay induced by scattering (e.g. McKinnon, 2014) — modulated by a running power law across the band. However, FRBs from repeating sources regularly display complex behaviour, such as drifting sub-structure as well as frequency-dependent profile variations intrinsic to the emission mechanism (Hessels et al., 2019). In the low-S/N limit, such frequency-dependent

---

<sup>4</sup>[https://github.com/danielemichilli/DM\\_phase](https://github.com/danielemichilli/DM_phase)

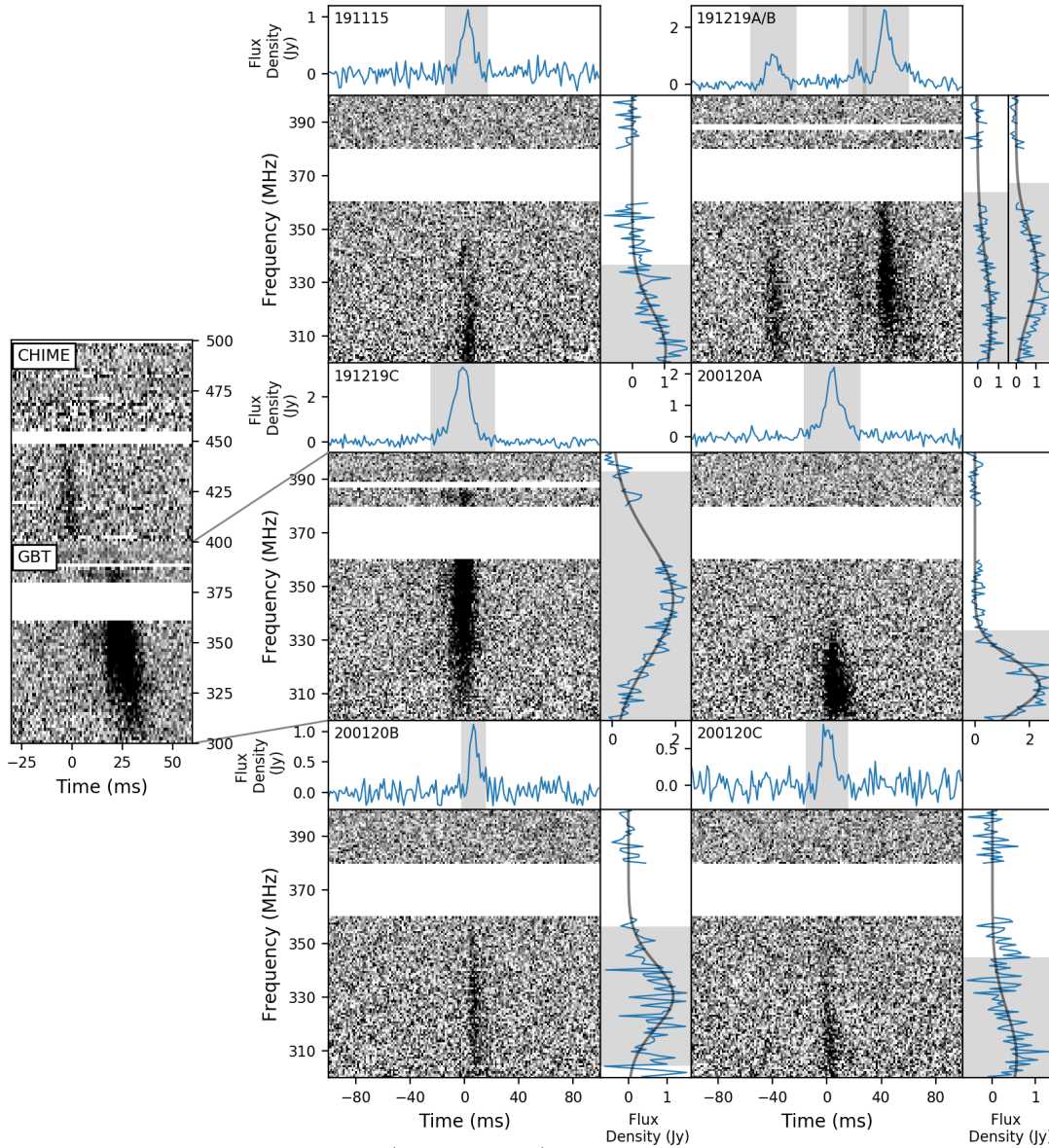


**Figure 4.2:** Dynamic spectrum (“waterfall”) plots of seven bursts from the repeating FRB 180916.J0158+65 detected with the GBT. For each burst, data for 128 frequency sub-bands, corrected for the receiver bandpass and dedispersed to the structure-optimizing DM (listed in Table 4.2), are plotted here. In order to better visualize the burst, each dynamic spectrum is downsampled to a resolution of 1.31 ms and intensity values are saturated at the 5th and 95th percentiles. Horizontal white bands are the frequency channels masked due to RFI. The band-averaged time series is plotted on the top of each dynamic spectrum. The on-pulse spectrum (plotted on the right) is obtained by averaging the flux within twice the FWTM of a Gaussian model fit to the time series. The assumed on-pulse region is shaded in grey in the top panel with the shaded region in the right panel showing the FWTM of a Gaussian model fit to the on-pulse spectrum. Dynamic spectra for bursts 191219A and 191219B are shown in the same panel since the arrival times for the two are within  $\sim 60$  ms of each other. *Burst 191219C sub-panel:* This burst was associated with a CHIME/FRB detection (see §4.2.2). The composite dynamic spectrum for the two bursts, shown in the left-most panel, is corrected for the instrument bandpass and has a time and frequency resolution of 0.98304 ms and 1.5625 MHz, respectively. Data for the composite spectrum are dedispersed to the average DM of the source,  $348.82 \text{ pc cm}^{-3}$ , whereas data shown in the panel to the right are dedispersed to the structure-optimizing DM derived from the GBT-detection ( $349.5 \text{ pc cm}^{-3}$ ; see §4.3.1). There is no visible emission in the CHIME/FRB data outside the frequency range plotted here.

structure can be temporally unresolved and mimic the effects of scatter broadening, potentially biasing the scattering measurements. However, in order to assess the statistical significance of scattering and place upper limits whenever possible, we nonetheless apply two-dimensional pulse broadening functions as models to the GBT spectra in a manner consistent with previous CHIME/FRB analyses.

We estimate fluence by integrating the extent of each burst in the band-averaged time series with the peak flux density estimated to be the highest value in this time series. Both these measurements rely on the off-pulse mean and standard deviation used in correcting the data for the receiver bandpass. Therefore, we generate different realizations of calibrated data, each using the off-pulse mean and standard deviation from a different time chunk (of 3-s duration) in the observation in which the burst was detected. We measure the fluence and peak flux density for each realization of the calibrated data and report the mean and standard deviation of these measurements in Table 4.2.

### 4.3.2 Drift Rate Measurement for Burst 191219C

If the estimate of the temporal separation between burst 191219C and its coincident CHIME/FRB detection is correct, then we can measure the linear drift rate of the sub-bursts in the burst envelope that drifts from the bottom of the CHIME band into the top of the GBT band (see Figure 4.2) using a Monte Carlo resampled auto-correlation analysis (CHIME/FRB Collaboration et al., 2019a). A 2D auto-correlation of the dedispersed dynamic spectrum characterizes the self-similarity of the burst in frequency and time and thus provides a measurement of the drift rate. We use the composite dynamic spectrum in the frequency range of 300–500 MHz having 256 normalized frequency channels dedispersed to  $348.82 \text{ pc cm}^{-3}$  for this analysis.

The Monte Carlo resampling aspect of the analysis involves performing the auto-correlation for spectra dedispersed at different DMs and with random instances of noise being added to the data. The resampling provides multiple measurements of the drift

Name	Arrival Time <sup>b</sup> (MJD)	S/N	DM <sup>c</sup> (pc cm <sup>-3</sup> )	Scattering Time <sup>d</sup> (ms)	Width <sup>e</sup> (ms)	Fluence (Jy ms)	Peak Flux Density <sup>f</sup> (Jy)	Centre Freq. (MHz)	Bandwidth (MHz)	RM <sup>g</sup> (rad m <sup>-2</sup> )
191115	58802.25840267	11.3	349.3(2)	<2.9	3.6(5)	10.2(5)	1.18(6)	304(5)	64(17)	
191219A	58836.16929624	13.3	348.8(4)	5.9(3)	2.7(4)	11.2(4)	1.24(5)	316(5)	96(19)	-116.9(5)
191219B <sup>h</sup>	58836.16929695	28.6	348.8(4)	5.9(3)	3.9(8)	5.2(2)	1.09(4)	334(1)	66(6)	-116.9(2)
	58836.16929720				2.42(18)	31.9(1.1)	2.66(9)			
191219C	58836.17591822	54.9	349.5(3)	<1.7	5.89(11)	48.9(1.7)	3.58(13)	345.2(7)	96(2)	-116.6(2)
200120A	58868.08221442	19.3	348.9(1)	4.1(3)	3.7(2)	28.1(9)	2.28(7)	312.9(6)	41(2)	-117.7(3)
200120B	58868.08461892	14.4	348.7(2)	3.1(5)	1.5(3)	7.8(2)	1.30(4)	330.5(9)	52(4)	
200120C	58868.08679636	11.9	348.8(2)	1.8(9)	3.2(6)	7.7(2)	0.98(3)	307(5)	75(16)	

**Notes.**

<sup>a</sup>Uncertainties and upper limits are reported at the  $1\sigma$  and  $2\sigma$  confidence level, respectively.

<sup>b</sup>Arrival times are corrected to the solar system barycentre and referenced to infinite frequency.

<sup>c</sup>DMs reported here are obtained through the process of structure-optimization (see §4.3) with the dynamic spectra shown in Figure 4.2 dedispersed to these DMs.

<sup>d</sup>Scattering timescales reported here are measured at a frequency of 350 MHz. See §4.4.1 for a discussion on the scattering estimates and sources of bias that can produce apparent variations.

<sup>e</sup>All values are intrinsic burst widths since spectra are fitted with two-dimensional pulse broadening functions, and thus separate frequency-dependent scattering contributions and intrinsic components from the observed widths.

<sup>f</sup>Peak flux density for each burst is estimated from the corresponding band-averaged time series at a resolution of 327.68  $\mu$ s.

<sup>g</sup>The values are not corrected for ionospheric contribution.

<sup>h</sup>Burst 191219B is treated as having two components rather than being two separate bursts since the emission between the two does not revert to the baseline noise level. Therefore, arrival time, width, fluence and peak flux density for the two components are reported separately.

**Table 4.2:** Burst Properties<sup>a</sup>

rate, enabling characterization of the measurement uncertainty. We use  $100 \times 100 = 10,000$  random noise and DM uncertainty samples, and set the difference between the best known DM for the source and the inverse-variance weighted average DM of the GBT bursts,  $0.12 \text{ pc cm}^{-3}$ , as the DM uncertainty. Two systematics in the auto-correlation analysis are the 0.1953125 MHz offset between the two bands and the alignment of time samples of the two systems, which is uncertain on the  $\sim 30 \mu\text{s}$  level. Both effects introduce uncertainties on the drift rate measurement that are much smaller than the nominal uncertainty calculated from resampling the noise and DM uncertainty distributions. However, as noted above, there might be an additional unaccounted for offset between the two receivers on the  $\sim \text{ms}$  level. We measure  $d\nu/dt = -4.2_{-0.4}^{+0.4} \text{ MHz ms}^{-1}$  (68% confidence interval), under the assumption that that receiver time offset is negligible. This value is consistent with the general observed trend for the drift rates to be lower at lower frequencies for bursts from FRB 121102 (Hessels et al., 2019; Josephy et al., 2019) and it points to a similar trend for FRB 180916.J0158+65. However, for FRB 180916.J0158+65, the lack of drift rate measurements at gigahertz frequencies impedes a measurement of drift rate evolution with frequency for now.

### 4.3.3 Polarization Properties

Polarization properties have been analyzed for four bursts of our sample. The lower S/N of the rest of the detections did not allow us to obtain robust measurements. One second of frequency-resolved Stokes parameters have been extracted for each burst by using the PSRCHIVE library<sup>5</sup> (Hotan et al., 2004). A one-minute scan of a noise diode was acquired at the beginning of each observation and was used to calibrate the Stokes parameters of the bursts (van Straten et al., 2012). All the bursts have been dedispersed to  $349.5 \text{ pc cm}^{-3}$  for this analysis. Following CHIME/FRB Collaboration et al. (2019a), the rotation measures (RMs) of the bursts have been calculated by using the implementation of rotation measure

---

<sup>5</sup><http://psrchive.sourceforge.net>

synthesis (Burn, 1966; Brentjens & de Bruyn, 2005) in the RM-tools package<sup>6</sup> and the resulting Faraday dispersion function (FDF) was cleaned with the deconvolution algorithm presented by Heald (2009). The FDF of bursts detected on MJD 58836 showed effects of a bad calibration, apparent in the presence of peaks at RM values symmetric about zero. This was solved by using the scan of the noise diode acquired on MJD 58835. The quality of the FDFs, one of which is reported in the bottom of Figure 4.3, demonstrates the validity of this operation.

The measured RM values are reported in Table 4.2. On 2018 December 26, the RM for FRB 180916.J0158+65 was measured to be  $-114.6(6) \text{ rad m}^{-2}$  (CHIME/FRB Collaboration et al., 2019a); it therefore shows possible evidence of a decrease of  $2\text{--}3 \text{ rad m}^{-2}$  over one year. According to the RM model of the ionosphere `RMextract` (Mevius, 2018), its varying contribution can account for  $\lesssim 0.4 \text{ rad m}^{-2}$ . However, systematic effects between GBT and CHIME could account for the remaining discrepancy. Among the GBT bursts, 191219A and 191219B are separated by less than 100 ms. They show the same RM within the errors. Burst 191219C, detected on the same day, also shares the same RM. However, burst 200120A, detected a month later, shows a marginal increase in RM of  $\sim 1 \text{ rad m}^{-2}$ , which is still compatible at  $2\sigma$  level. Therefore, even though the varying contribution of the ionosphere only accounts for  $\sim 0.1 \text{ rad m}^{-2}$ , we consider the measurements in agreement and more observations are required to detect an eventual evolution of the RM with time.

Each of the bursts has been corrected for its RM and the resulting polarization profiles are reported in Figure 4.3. Following Everett & Weisberg (2001), we estimate that all the bursts in the sample have a linear polarization fraction larger than 90% and a circular polarization fraction consistent with zero. However, we note that the fractional polarization measurements could be biased, especially for weak bursts.

The time-resolved polarization angle (PA), also shown in Figure 4.3, is approximately flat within each burst, with reduced  $\chi^2$  values with respect to a straight line ranging between

---

<sup>6</sup><https://github.com/CIRADA-Tools/RM>

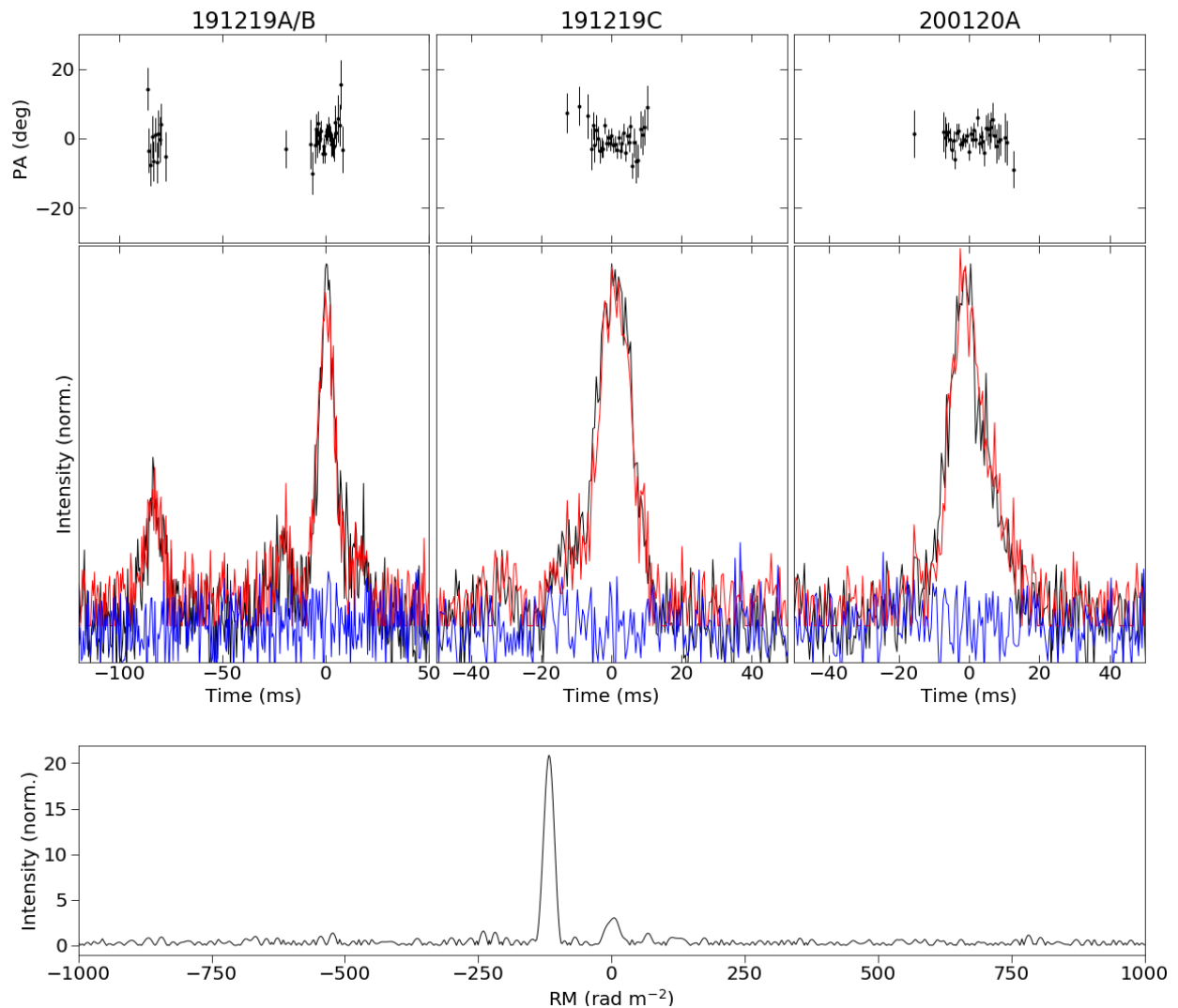


**Figure 4.3:** Polarization properties of four of the GBT bursts. Top: Pulse profiles, in normalized units, of total intensity (black), linear polarization (red) and circular polarization (blue) with polarization angles plotted on top. Polarization angle measurements have been rotated independently in each panel to have a null mean. Bottom: example of the FDF for burst 191219C after applying the cleaning algorithm (see text).

0.7 and 0.9. Due to the lack of an absolute polarization calibration, we did not attempt to compare PA values for different bursts, except for bursts 191219A and 191219B, which are separated by only 100 ms. Their average PA values are in agreement, with a difference of the weighted PA curves of  $0.5 \pm 2.5$  deg.

It is interesting comparing the polarization properties of FRB 180916.J0158+65 with the other repeating FRB source with a measured RM, FRB 121102 (Michilli et al., 2018). The latter shows an extreme value of Faraday rotation corresponding to an RM  $\sim 10^5$  rad m<sup>-2</sup>, orders of magnitude higher than the value measured for FRB 180916.J0158+65. The RM of FRB 121102 varied by  $\sim 10\%$  over 7 months, which is not observed for FRB 180916.J0158+65. The flat PA curve within each burst is an interesting similarity between the two FRB sources, together with a linear polarization fraction close to 100% and a circular polarization fraction of approximately 0%. The rest of the FRB population shows very diverse polarization properties, with varying RM values, polarization fractions and PA curves (Petroff et al., 2016).

#### 4.3.4 Periodicity Search

Although the source exhibits a modulation in activity at a 16.35-day period (or possibly a higher-frequency alias; see §3.6.1), an additional periodicity of the order of milliseconds to seconds might be present if the progenitor is a neutron star (Yang & Zou, 2020; Lyutikov et al., 2020; Ioka & Zhang, 2020) and the bursts come from a narrow range of rotational phases. We use two different methods to search for a periodicity due to stellar rotation. First, we fit the largest common denominator to the differences in arrival times of bursts detected in individual observations, as is done for rotating radio transients (McLaughlin et al., 2006). We did not find any statistically significant periodicities in the two observations having multiple detections (see Table 4.1). We note that bursts 191219A and 191219B have a separation of  $\sim 60$  ms which is similar to the separation between sub-bursts in two bursts of this source, as noted by CHIME/FRB Collaboration et al. (2019a). However, periods close

to 60 ms were not found to be statistically more significant than any other trial periods in the aforementioned analysis. Detection of eight or more bursts in a single observation might be necessary to determine an underlying periodicity, if it exists, with this method (Cui et al., 2017).

For GBT observations in which there were single-pulse detections, we also searched for a rotational periodicity using PRESTO’s Fourier domain acceleration search algorithm, `accelsearch`. We conducted this search on the same  $327.68\text{-}\mu\text{s}$  resolution data as the initial single-pulse search, with the same `rfifind` mask and dedispersed to the same grid of DMs. Initially we searched all DMs using a `zmax` parameter of 200, implying an acceleration range of  $\pm 20\text{ ms}^{-2}$  for a 500 Hz (2 ms) signal. Next, we used the “jerk-search” functionality of `accelsearch` (Andersen & Ransom, 2018) to search at the nominal DM with a `zmax` of 100 and a `wmax` of 500, corresponding to an acceleration range of  $\pm 10\text{ ms}^{-2}$  and a jerk range of  $0.02\text{ ms}^{-3}$  for a 500 Hz signal. Finally, we ran a jerk search for the period of time in the MJD 58836 observation encompassing 10 min around burst 191219B, with a `zmax` of 100 and a `wmax` of 500, corresponding to an acceleration range of  $\pm 167\text{ ms}^{-2}$  and a jerk range of  $1.40\text{ ms}^{-3}$  for a 500 Hz signal. The best candidates from all three of these searches were folded using PRESTO’s `prepfold` and inspected by eye. No convincing periodic astrophysical signals were found.

#### 4.3.5 Determination of System Sensitivity

We determine fluence completeness for the CHIME/FRB system at the time of detection of the GBT bursts by expanding on the methods outlined in Josephy et al. (2019). Previously, detection scenarios were generated in a Monte Carlo simulation in order to capture sensitivity variations due to source position along transit, burst spectral shape, and detection epoch. Relative sensitivities for these detection scenarios were translated to fluence thresholds using bandpass-calibrated observations of bursts detected from FRB 180916.J0158+65 by CHIME/FRB Collaboration et al. (2020a). In this work, we do not

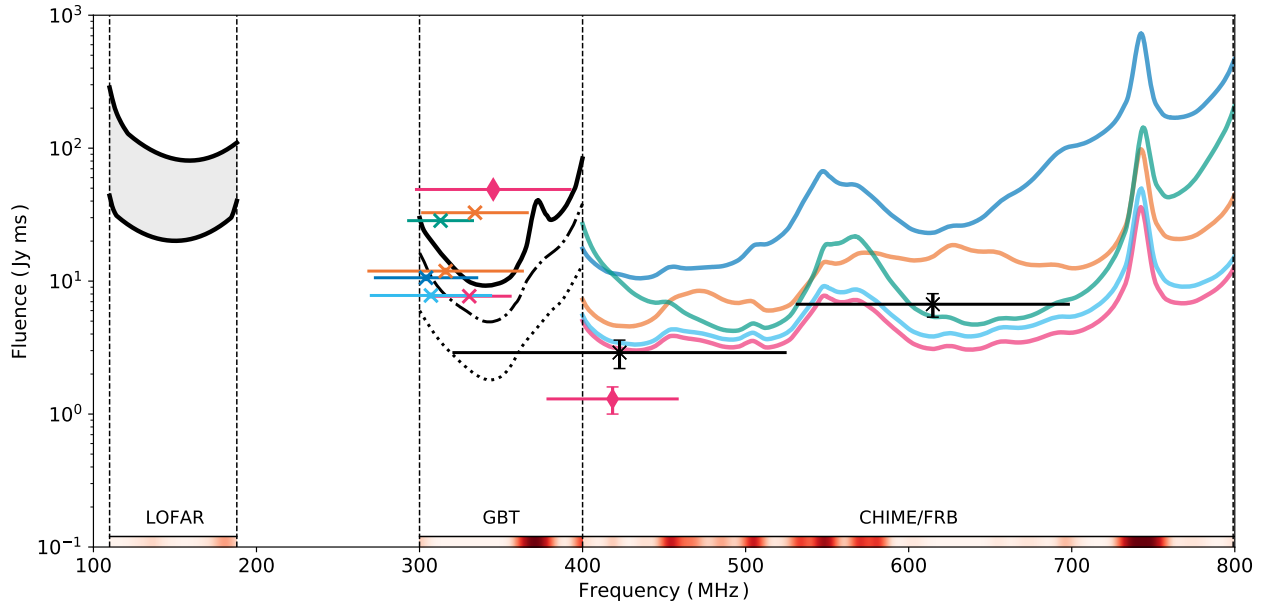


**Figure 4.4:** Burst fluences and completeness limits for LOFAR, GBT, and CHIME/FRB. Vertical dashed lines bracket the observing frequencies of each instrument. Markers with  $\times$ 's represent bursts detected with a single instrument, while the diamond markers correspond to the co-detection between GBT and CHIME/FRB. Markers are placed according to the peak frequency of their Gaussian fits, with horizontal lines in the frequency axis representing the FWTM of the fit. Marker colours and line colours are matched to show instantaneous sensitivity across instruments (approximated as constant for GBT and LOFAR, variable for CHIME/FRB depending on source position within synthesized beams). Solid lines show fluence completeness at the 90% confidence interval towards bursts with Gaussian spectral profiles centred at each given frequency, with emission bandwidths ranging from 10–80 MHz (FWHM). The non-monotonic nature of the CHIME/FRB completeness curves (i.e., crossing lines) are due to side-lobe sensitivity of the four synthesized beams relevant for detection. For GBT, we also show 50% completeness and 5% completeness with dash-dotted and dotted lines respectively, indicating typical and optimistic sensitivities. For LOFAR, we show completeness in the limit of no scattering (bottom line), and for the scattering timescale upper limit of 50 ms at 150 MHz (top line). The red shaded strips along the bottom of the plot show average RFI masking fractions of each instrument convolved with a 10 MHz (FWHM) Gaussian profile; masking fraction ranges from 0% (white) to 100% (dark red).

sample the transit position when simulating detection scenarios; instead we examine the instantaneous sensitivity at the time of each GBT burst. This distinction is important for CHIME/FRB, since the sensitivity varies significantly depending on the source’s position within the synthesized beams, as seen in Fig. 4.4. Furthermore, we compute fluence thresholds for Gaussian bursts of different central frequencies instead of computing band-averaged fluence thresholds. This choice is informed by the bands under consideration having frequency-dependent sensitivity and appreciable RFI contamination due to which the detectability of a given burst varies significantly as it is shifted throughout the band. For burst bandwidths, we uniformly sample from 10–80 MHz (FWHM) to match the observed range.

We extend this analysis to obtain the fluence completeness limit for the GBT observations by swapping in the appropriate bandpass. The frequency response across the band is estimated to be the mean of the counts detected in each frequency channel over all time intervals not flagged for masking. The completeness limit as a function of the central frequency of emission is shown in Figure 4.4, while the band-averaged 90%-completeness limit is estimated to be 22 Jy ms. In extending the analysis to LOFAR, we determine the frequency response using Equation 4.1; taking into account the exact number of Core stations used and correcting for the zenith-angle dependence as described by [Kondratiev et al. \(2016\)](#). Since no burst was detected in the LOFAR observations, we use the radiometer equation to construct a fiducial reference burst, which is parameterized as having the mean width of all bursts reported in this work (3.3 ms), a S/N of 7 (detection threshold of the search pipeline), a central frequency of 150 MHz, and a spectral bandwidth of 80 MHz (FWHM). With 18% of channels having some RFI contamination, we take the effective bandwidth to be 64 MHz. Substituting these parameters and a band-averaged sky temperature, receiver temperature and gain in the radiometer equation in the limit of no pulse broadening, this reference scenario gives a fluence detection limit of 21 Jy ms. Considering the same range of Gaussian spectral profiles as above, the

band-averaged 90%-completeness limit is estimated to be 24 Jy ms. To account for suppressed detectability due to potential pulse broadening, we repeat this analysis using the upper limit on the scattering timescale of 50 ms at 150 MHz (see §4.4.1). In this scenario, the band-averaged 90%-completeness becomes 106 Jy ms, assuming a power-law index of  $-4$  for the frequency dependence of scatter-broadening for different spectral profiles. The completeness threshold is significantly higher than that of the GBT due to the high Galactic foreground emission (a sky temperature of  $\sim 700$  K at 150 MHz) at the source position.

## 4.4 Discussion

The detection of emission in multiple bursts from FRB 180916.J0158+65 down to the bottom of the GBT band indicates that a cutoff or turnover in the FRB rest-frame spectrum can only exist below a frequency of  $\sim 300$  MHz. Since this source is the closest localized FRB (Marcote et al., 2020), other FRBs could be detectable at frequencies lower than 300 MHz as their rest-frame spectra would be redshifted to even lower frequencies. We note that this conclusion would not apply to the so-far non-repeating FRBs if repeating and non-repeating sources do not share a common emission mechanism. A spectral turnover due to propagation effects in the circumburst environment (Ravi & Loeb, 2019) or scattering combined with a flat spectrum for FRB emission (Chawla et al. 2017) can still render FRBs undetectable at low frequencies. Therefore, detection of emission from this source at 300 MHz can potentially still be consistent with the non-detection of FRBs with several surveys in this frequency range (Deneva et al., 2016; Chawla et al., 2017; Rajwade et al., 2020a) if a less dense circumburst environment (see §4.4.4), low scattering timescale (see §4.4.1) and the proximity of the source conspire to make its emission particularly detectable.

#### 4.4.1 Scattering Times

Assuming that the scattering properties of the intervening medium do not change between detections, we report a 95% confidence upper limit of 1.7 ms on the scattering timescale of the source at 350 MHz, improving significantly on the constraint derived from CHIME/FRB observations,  $< 0.9$  ms at 600 MHz (which translates to  $< 8$  ms at 350 MHz, assuming a power-law frequency dependence of  $-4$ ; [Bhat et al. 2004](#)). An indirect measurement of scattering for this source,  $\sim 2.7$   $\mu$ s at 1.7 GHz, was obtained by [Marcote et al. \(2020\)](#) using the auto-correlation function estimated from a burst spectrum, assuming that the frequency-dependent intensity variations are due to scintillation. This translates to a scattering timescale of  $\sim 1.5$  ms at 350 MHz which is consistent with the GBT measurement. We used the methodology and code employed by [Masui et al. \(2015\)](#) to estimate the auto-correlation function for the spectrum of the brightest burst in our sample (191219C) but find its magnitude small enough to suggest a non-astrophysical origin and be potentially explained by errors in modelling the burst spectrum or in correcting for the receiver bandpass.

Assuming a power-law index of  $-4$ , the upper limit on the scattering timescale derived from GBT observations translates to 50 ms at 150 MHz. This suggests that pulse smearing due to scattering alone cannot explain the non-detection with LOFAR, for which observations were searched for bursts with widths up to 0.3 s (see §4.2.3). Detection of the source at frequencies lower than 300 MHz is essential to obtain an accurate measurement of the scattering timescale. However, the measured upper limit is not inconsistent with that of known FRBs: an FRB discovered by the UTMOST telescope exhibited a scattering timescale of  $4.1 \pm 2.7$   $\mu$ s at 835 MHz (scales to 0.13 ms at 350 MHz; [Farah et al. 2018](#)), suggesting that FRB 180916.J0158+65 is not atypical of the FRB population.

#### 4.4.2 Phase Dependence of Source Activity

If the periodic modulation of source activity is due to orbital motion, then any inhomogeneities in the source environment can cause some burst properties to be phase-dependent, as suggested by [CHIME/FRB Collaboration et al. \(2020a\)](#). Following the approach of [CHIME/FRB Collaboration et al. \(2020a\)](#), we compute the phases of all detections and see no monotonic variation in DM, fluence, burst width, scattering timescale or emission frequency with phase or time in the sample of GBT bursts as well as in the overall sample of bursts from the source which includes detections from the CHIME/FRB system and the European Very-long-baseline-interferometry Network (EVN; [Marcote et al. 2020](#)). We caution that observations of the source with the GBT did not cover a large fraction of the 5-day-long activity window. Additionally, we note that the aforementioned conclusion would not hold if the true period is not 16.35 days, as the estimated phases for all detections would be incorrect. Detections with the GBT cannot help in ruling out any of the possible higher-frequency aliases of the 16.35-day period, as all observations in which these detections were made were coincident with the transit of the source over the CHIME telescope.

#### 4.4.3 Frequency Dependence of Source Activity

Six of the seven GBT bursts were not detected with the CHIME/FRB system although their GBT fluences were higher than or, in two cases, comparable to the corresponding 95% confidence fluence threshold (see Figure 4.4). The burst for which coincident emission was detected was the only GBT burst with emission detected at the top of the band (400 MHz), with a GBT-measured fluence of  $48.9 \pm 0.3$  Jy ms and a fluence in the CHIME band of  $1.3 \pm 0.3$  Jy ms. Coincident detection of only one burst out of a total of ten unique bursts detected by the two instruments during simultaneous observations suggests that emission is restricted to a narrow frequency range for individual bursts (fractional bandwidths of 13–30% were measured for the GBT detections), with the overall source spectrum being

highly variable as the centre frequency of the individual bursts varies with time. This is consistent with the non-detection of coincident emission from FRB 121102 with the Arecibo telescope at 1.4 GHz and the Very Large Array (VLA) at 3 GHz for several bursts detected in simultaneous observations with the two instruments (Law et al., 2017; Gourdji et al., 2019). Similarly, Hessels et al. (2019) used 1.1–1.7-GHz Arecibo observations to show that FRB 121102 bursts have fractional bandwidths ranging from 7–30% at these frequencies. Longer observations of repeating FRB sources, simultaneously in several observing bands, are required to identify any potential temporal variations in the emission frequency of multiple narrow-band detections.

Based on a total of 3.9 hours of exposure to the source, we estimate the burst rate in the 300–400 MHz frequency range to be  $\lambda_1 = 1.8_{-1.1}^{+1.9}$  bursts  $\text{hr}^{-1}$  above a fluence threshold,  $F_{\nu_1, \text{min}}$ , of 22 Jy ms, with the uncertainties representing the 95% confidence interval derived assuming Poisson statistics. Since all observations were within a phase window of 0.1 (phases ranging from 0.47 to 0.57; see Figure 4.1), we compare the GBT-detection rate with the CHIME/FRB measurement in the same phase window,  $\lambda_2 = 1.7_{-0.8}^{+1.3}$  bursts  $\text{hr}^{-1}$  above a fluence threshold,  $F_{\nu_2, \text{min}}$ , of 5.2 Jy ms (CHIME/FRB Collaboration et al., 2020a). We scale the CHIME/FRB detection rate to that expected for a fluence threshold of  $F_{\nu_1, \text{min}}$  using a power-law index,  $\gamma = -2.3 \pm 0.4$ , estimated for the differential energy distribution of the source by CHIME/FRB Collaboration et al. (2020a) and find that the expected detection rate is consistent with that measured for the GBT. Therefore, we cannot ascertain whether there is a variation in source activity with frequency using a direct comparison of the detection rates in the two bands.

Following Houben et al. (2019), we characterize the frequency dependence of source activity using a statistical spectral index,  $\alpha_s$ , which characterizes the power law relating the normalization (A) of the differential energy distribution ( $dN(\nu)/dE = A(\nu)E^\gamma$ ) at different frequencies. The detection rates,  $\lambda_1$  and  $\lambda_2$ , at two frequencies,  $\nu_1$  and  $\nu_2$ , are then related

as,

$$\frac{\lambda_1}{\lambda_2} = \left(\frac{\nu_1}{\nu_2}\right)^{-\alpha_s \gamma} \left(\frac{F_{\nu_1, \min}}{F_{\nu_2, \min}}\right)^{\gamma+1}. \quad (4.2)$$

We estimate  $\alpha_s = -1.6_{-0.6}^{+1.0}$ , with the reported 95% confidence level uncertainties determined by the range obtained when solving for this parameter in 10,000 simulations of sets of  $\lambda_1$ ,  $\lambda_2$  and  $\gamma$ , where each is sampled from its Gaussian distribution of mean and range given above. This measurement is consistent within reported uncertainties with the statistical spectral index estimated for FRB 121102 using observations in the frequency range of 1.2–3.5 GHz by [Houben et al. \(2019\)](#). We note that this measurement is robust only if the true period of the source is 16.35 days since a higher-frequency alias would imply that all observations are at phases different than those currently estimated. Moreover, the conclusion also relies on the burst rate being constant in each period of source activity since the GBT detection rate is estimated from observations over three periods as compared to the  $\sim 20$  periods used for the CHIME/FRB measurement. If the aforementioned assumptions hold, then the measurement implies decreasing burst activity with increasing frequency for the source and could explain its non-detection at 1.4 GHz (above a fluence threshold of 0.17 Jy ms) with the Effelsberg telescope in 17.6 hours of exposure during a predicted epoch of activity ([CHIME/FRB Collaboration et al., 2020a](#)). This conclusion would also be consistent with the spectral index of  $\alpha = -1.5 \pm 0.2$  estimated for the mean spectrum of 23 FRBs detected by ASKAP at 1320 MHz ([Macquart et al., 2019](#)) with the caveat that the mean spectrum is not redshift-corrected while the statistical spectral index that we evaluate characterizes the rest-frame spectrum of the source.

We did not detect coincident emission with LOFAR at the time of detection of six GBT bursts. Assuming the emission is broadband and that the burst fluence scales with frequency as  $F_\nu \propto \nu^\alpha$ , we can use the brightest burst in our sample, 191219C, to place a constraint on the spectral index,  $\alpha$ , of the instantaneous emission from the source. We obtain a lower limit of  $\alpha > -1.0$ , which is the spectral index for which the 95% confidence lower bound on the GBT-measured fluence of the burst (see Table 4.2) would imply a fluence at 150 MHz

equal to the 90% completeness fluence threshold of the LOFAR observations (106 Jy ms; see §4.3.5). However, it could be that coincident emission was suppressed in the LOFAR band not due to the burst having a flat spectrum but rather due to its band-limited nature. In that scenario, non-simultaneous bursts could still have been detected in the LOFAR band during the 1.3 hours of exposure to the source. The non-detection of such bursts could be explained by flattening of the statistical spectrum at low frequencies, as suggested by [Houben et al. \(2019\)](#) for FRB 121102. To investigate the possibility of spectral flattening, we derive a 95% confidence upper limit on the burst rate in the LOFAR band of 2.2 bursts hour<sup>-1</sup> above a fluence threshold of 106 Jy ms. We then obtain a 95% confidence lower limit on the statistical spectral index between the GBT and LOFAR bands,  $\alpha_s > -1.4$ . Since this measurement of the statistical spectral index is consistent with that derived by comparing detection rates in the GBT and CHIME bands, we cannot confirm or rule out a flattening of the spectrum at low frequencies.

#### 4.4.4 Constraints on Proposed Models

The detection of FRB 180916.J0158+65 down to 300 MHz shows that its source’s ambient environment is optically thin to free-free absorption at 300 MHz. For an ionized nebula of size  $l_{\text{pc}}$ , and  $\text{DM} < 70 \text{ pc cm}^{-3}$  ([Marcote et al., 2020](#)), this implies the optical depth due to free-free absorption ([Condon & Ransom, 2016](#)),

$$\tau_{\text{ff}} = 1.6 \times 10^{-3} \times \left( \frac{T}{10^4 \text{K}} \right)^{-1.35} \times \left( \frac{\nu}{1 \text{GHz}} \right)^{-2.1} \times \frac{1}{f_{\text{eff}} l_{\text{pc}}} \times \left( \frac{\text{DM}}{70 \text{ pc cm}^{-3}} \right)^2 \ll 1, \quad (4.3)$$

where  $f_{\text{eff}}$  is a factor that accounts for the volume-filling factor and the electron density fluctuation in the circumburst medium. If such a nebula circumscribes the FRB 180916.J0158+65 source, our detection implies  $l \gg 0.02 \text{ pc} (T/10^4 \text{ K})^{-1.35}$  which rules out a surrounding dense and compact ionized nebula like a hyper-compact HII region ([Churchwell, 2002](#)) or a young supernova remnant (age  $< 50 \text{ yr}$ ; [Piro 2016](#)). This result is

consistent with observations of the source by [Marcote et al. \(2020\)](#) who conclude, based on the measured RM and non-detection of an associated persistent radio source, that FRB 180916.J0158+65 has a much less extreme circumburst environment compared to that of the other localized repeater, FRB 121102. From Equation 4.3, free-free absorption at frequencies well below 300 MHz seems unlikely to inhibit detectability, so follow-up observations in this regime are warranted in order to constrain the intrinsic FRB spectrum turn-over frequency.

Induced Compton scattering (ICS) can also suppress the observed low-frequency emission from FRBs specifically in models that invoke magnetar giant flares ([Lyubarsky, 2014](#); [Beloborodov, 2017](#); [Metzger et al., 2019](#); [Margalit et al., 2020](#); [Levin et al., 2020](#)). In the synchrotron maser model ([Metzger et al., 2019](#); [Margalit et al., 2020](#)), FRBs are produced when the decelerating ultra-relativistic shock waves from a flaring hyperactive magnetar interact with the sub-relativistic circumstellar medium (CSM). As the shock propagates into the CSM, ICS attenuates the FRB emission. However, the negative spectral indexes of some of the bursts we have observed for FRB 180916.J0158+65 argue that the optical depth due to ICS,  $\tau_{\text{ICS}} < 1$  at 300 MHz. The constraint that  $\tau_{\text{ICS}} < 1$  implies a density upstream from the shock ([Kumar & Lu, 2020](#)),

$$\rho \lesssim 8 \times 10^{-3} \text{cm}^{-3} \left( r_{\text{dec}} / 10^{12} \text{cm} \right)^2 \left( L / 10^{43} \text{erg s}^{-1} \right)^{-1} \left( w_i / 1 \text{ms} \right)^{-1} \left( \Gamma_{\text{CSM}} \right)^{-2}, \quad (4.4)$$

at the deceleration radius  $r_{\text{dec}}$ , the distance that a relativistic shock travels before half of its energy is dissipated to its ambient medium,  $\sim 10^{12}$  cm ([Metzger et al., 2019](#)). Here,  $L$  is the isotropic equivalent luminosity of the FRB,  $w_i$  is the burst temporal width, and  $\Gamma_{\text{CSM}}$  is the Lorentz factor of the shocked CSM gas. However, the [Metzger et al. \(2019\)](#) model requires an upstream density of  $\sim 10^2 \text{cm}^{-3}$  for the synchrotron maser to be effective; for our optical depth constraint, this requires  $r_{\text{dec}} > 10^{14}$  cm for the above parameters. [Kumar & Lu \(2020\)](#) have argued that it is difficult to produce FRBs at distances  $> 10^{14}$  cm because of the

requirement of the source luminosity to be  $> 10^{46}$  erg s $^{-1}$  for each repeat burst — difficult to obtain even from a hyperactive magnetar. Thus, the detection of FRB 180916.J0158+65 bursts down to 300 MHz challenges some of the assumptions of the maser synchrotron model.

## 4.5 Conclusions

We have reported on the detection of emission from the repeating FRB 180916.J0158+65 at frequencies down to 300 MHz. This result implies that any cutoff in the rest-frame FRB spectrum exists at a frequency below 300 MHz, and thus bodes well for future blind surveys for FRBs as well as follow-up observations of repeating FRBs at low radio frequencies. Using burst rates in the GBT band (300–400 MHz) and the CHIME band (400–800 MHz), we compute a statistical spectral index,  $\alpha_s$ , to characterize the frequency dependence of source activity. We find  $\alpha_s = -1.6_{-0.6}^{+1.0}$ , which is consistent with observations of FRB 121102 by [Houben et al. \(2019\)](#) and motivates follow-up observations of other repeating FRBs to determine whether this trend is common to all sources. We do not see any frequency dependence to the polarization fraction in the overall sample of bursts from this source, with the four brightest bursts in the GBT sample being nearly 100% linearly polarized and having a circular polarization fraction consistent with zero.

Our observation strategy of simultaneous coverage with GBT, the CHIME/FRB system and LOFAR allowed for a study of emission from this source over a large range of frequencies. Most bursts detected during these observations had low emission bandwidths (being observable with either the GBT or with CHIME/FRB) with the notable exception of GBT-detected burst 191219C which had a potentially associated sub-burst in the CHIME band. We detected no bursts in the frequency range 110–190 MHz with LOFAR despite performing an extensive search for bursts with narrow emission bandwidths and slow frequency drifts by visually inspecting LOFAR data in a  $\pm 10$ -s interval around the arrival times of the GBT bursts. Our constraint on the scattering timescale for the source,

$< 1.7$  ms at 350 MHz, rules out the phenomenon of scattering alone as a cause of non-detection of the source with LOFAR. However, we cannot yet say whether the reduced system sensitivity owing to the high sky temperature or a spectral turnover at these frequencies was the cause of the non-detection. More observations of the source at lower frequencies might help determine whether a spectral turnover exists.

In the late stages of writing this paper, we became aware of follow-up observations of the source at 328 MHz with the Sardinia radio telescope by [Pilia et al. \(2020\)](#). Detection of three bursts from the source in these observations is consistent with our conclusions.

## Chapter 5

# Modelling Dispersion and Scattering in the First CHIME/FRB Catalog

The contents of this chapter are part of a manuscript which has been submitted to the *Astrophysical Journal*: Chawla et al., 2021, Modeling Fast Radio Burst Dispersion and Scattering Properties in the First CHIME/FRB Catalog, arXiv e-prints, arXiv:2107.10858.

### 5.1 Introduction

Although the physical origin of FRBs is as yet unknown, they can be used as probes of electron density in the intervening media. As FRB sightlines encounter baryons occurring in a highly diffuse state in the IGM, the measured DMs of localized FRBs have been used to constrain the cosmic baryon density (Macquart et al., 2020). Variations in DM along FRB sightlines can probe electron density fluctuations in the IGM and constrain the length scales for IGM turbulence (McQuinn, 2014; Masui & Sigurdson, 2015; Xu & Zhang, 2020). Additionally, FRB DMs can be used to study the diffuse ionized gas in the halos of the Milky Way and other Local Group galaxies (see, e.g., Prochaska & Zheng 2019; Platts et al. 2020).

Another property of FRBs that can be used to study intervening plasma is scattering. The dominant source of FRB scattering is uncertain. No correlation has been observed between FRB scattering times and DMs (Katz, 2016a; Cordes et al., 2016; Qiu et al., 2020).

Since the IGM contributes significantly to FRB DMs (Shannon et al., 2018), the lack of a correlation between DMs and scattering times suggests that the IGM is not a significant source of scattering. Masui et al. (2015) also argue against the IGM being the dominant source of scattering for FRB 20110523A and suggest that scattering material is located either in the host galaxy or the circumburst environment. More recently, Chittidi et al. (2020) and Simha et al. (2020) concluded that the scattering for FRB 20190608B originates in either the spiral arm of the host galaxy or the circumburst environment and ruled out intervening halo gas as a source of scattering.

While the aforementioned studies focus on individual FRBs, it is important to ascertain the dominant source of scattering for the population as a whole. If scattering originates in the circumburst medium, then observed scattering timescales can help determine its properties and allow for constraints on progenitor models (CHIME/FRB Collaboration et al., 2019b). If the majority of scattering is found to be caused by halos of intervening galaxies instead, as is suggested by Vedantham & Phinney (2019), then FRB scattering can enable studies of these halos which are poorly understood. Additionally, population studies can also probe the level of plasma turbulence in galaxies that host FRBs (Cordes et al., 2016).

Population synthesis studies of FRB scattering involve simulating host galaxies and other intervening media to assess whether they can reproduce the observed properties for the population. Using this approach, CHIME/FRB Collaboration et al. (2019b) concluded that FRBs are located in environments with stronger scattering properties than the Milky Way ISM based on 13 FRBs detected with the CHIME telescope. Furthermore, Hackstein et al. (2020) found that the scattering timescales for bursts detected with the Parkes (Murriyang) telescope can only be explained by a more turbulent environment than that of SGR 1935+2154. However, these studies were conducted on small FRB samples without absolute calibration of observational biases.

As discussed in §2.3, the first CHIME/FRB catalog is the largest sample of FRBs detected using a single detection pipeline with a well-characterized selection function. In this chapter,

we report on a population synthesis study to interpret the scattering properties of the bursts in the catalog. In §5.2, we discuss our observational inputs which include the dispersion and scattering properties of the CHIME/FRB catalog. Simulated models for intrinsic FRB properties and propagation effects are described in §5.3 and §5.4, respectively. The procedure for the simulations is detailed in §5.5 while results are presented and discussed in §5.6. We summarize our conclusions in §5.7. We adopt the Planck cosmological parameters (Planck Collaboration et al., 2016) throughout this chapter.

## 5.2 Observations

The first CHIME/FRB catalog contains 474 so-far non-repeating sources and 61 bursts from 18 previously reported repeating sources observed in the interval from 2018 July 25 to 2019 July 2 (see §2.3). These bursts were detected in the frequency range of 400–800 MHz by searching 1024 total intensity (Stokes I) sky beams with a 0.983-ms time resolution.

The burst-fitting process is described in detail by CHIME/FRB Collaboration et al. (2021a). In summary, intensity data for the beam in which the burst was detected with the highest S/N is processed using a least-squares fitting routine, `fitburst`<sup>1</sup>. The two-dimensional dynamic spectra of the bursts is modelled as the product of two terms describing the time-independent spectral energy distribution (SED) and the temporal shape, respectively. The SED is modelled as a power-law function with an extra “running” term  $r$  in the exponent. The intensity at frequency  $\nu$ ,  $I(\nu) = (\nu/\nu_0)^{-\alpha+r\ln(\nu/\nu_0)}$ , where  $\alpha$  is the spectral index and  $\nu_0$  is the reference frequency (set to be equal to 400.1953125 MHz). The temporal shape is described by a Gaussian function convolved with an exponential scattering tail, the timescale for which has a power-law index of  $-4$  for the frequency dependence.

The routine fits for intrinsic width, DM, scattering timescale, burst amplitude, time of

---

<sup>1</sup>The `fitburst` code has not yet been made public, but the underlying model and likelihood are the same as that used by Masui et al. (2015), whose code is public.

arrival, spectral index and spectral running. A second model assuming no scattering is also fit to each burst and  $\chi^2$  values for the two models are compared to assess whether the detection of scattering is statistically significant. If the statistical significance is less than  $3\sigma$ , the scattering time is reported as an upper limit approximately equal to the intrinsic width. This criterion results in scattering times for 257 bursts being reported as upper limits. The best-fit models for a subset of the bursts in the catalog are shown in Figure 2.6.

The observed distribution of best-fit scattering times for the 535 bursts in the sample is not equivalent to the intrinsic distribution for the FRB population and requires correction for selection biases. As a start, bursts susceptible to unquantifiable selection effects are removed from the scattering time distribution. Detailed criteria for exclusion are presented by [CHIME/FRB Collaboration et al. \(2021a\)](#), but we note that these exclude bursts with DMs  $< 100 \text{ pc cm}^{-3}$ . Bursts with DMs  $< 1.5$  times the maximum of the Galactic DM estimates based on the NE2001 ([Cordes & Lazio, 2002](#)) and YMW16 ([Yao et al., 2017](#)) models are also excluded.

Additionally, we only include the first detection from each repeating FRB source. Subsequent bursts are excluded to ensure that repeating FRBs are not over-represented in the scattering time distribution for the full population. In doing so, we assume that the scattering timescales do not change between detection of repeat bursts. We find that this assumption is valid for all but one of the repeating sources in our sample i.e. scattering times for repeat bursts are consistent with each other at the  $3\sigma$  level.

The remaining sample includes 292 bursts from both repeating and non-repeating FRB sources. The distribution of scattering times for the surviving sample is then corrected for selection biases, which can be introduced by the telescope beam, RFI environment, gain calibration and signal-classification techniques. These biases are determined by injection of simulated signals into the real-time detection pipeline (see §2.2.4). In summary, the fluence, DM, pulse width, scattering time, spectral index and running of the simulated signals are sampled from the plausible ranges of these parameters. The detection probabilities

determined for the injected signals are used to ascertain the instrument selection function for different burst properties (CHIME/FRB Collaboration et al., 2021a).

We use the resulting selection-corrected distribution of scattering timescales as an observable to which we compare our simulations. Since dispersion and scattering properties for a given medium are correlated and cannot be studied in isolation, the selection-corrected DM distribution is also used in our analysis. Our population synthesis study tests different FRB population models based on whether they can reproduce this joint distribution of DM and scattering.

The population models that we test assume different spatial distributions and host galaxy types for the simulated FRBs. Additionally, some of the models invoke scattering originating in the circumburst medium and/or in the halos of intervening galaxies. For each population model, we first simulate properties intrinsic to the source, namely, burst energy, redshift and sky location. The prescriptions that we use for simulating these properties are described in §5.3. We then simulate the DM and scattering contributions of different intervening media, prescriptions for which are detailed in §5.4. Based on burst energies and redshifts, we determine which of the simulated FRBs are detectable with the CHIME/FRB system. The DM and scattering distributions of the simulated detectable bursts are then compared with the corresponding distributions in Catalog 1.

## 5.3 Modelling Intrinsic Properties

### 5.3.1 Redshift

The intrinsic distribution of FRB redshifts is not well-characterized due to the small number of observed FRBs with host galaxy associations (Heintz et al., 2020). In the absence of knowledge about the distribution, we test two different models for the variation of the number density of FRBs with redshift. The first model assumes a constant comoving number density

with the probability of detecting an FRB at a redshift  $z$ ,

$$P(z) \propto \frac{1}{1+z} \frac{dV_C}{d\Omega dz}, \quad (5.1)$$

where  $dV_C/(d\Omega dz)$  is the differential comoving volume per unit solid angle per unit redshift. The factor of  $(1+z)$  corrects the occurrence rate of FRBs in each redshift interval  $dz$  for time dilation due to cosmic expansion. The second model assumes that the number density

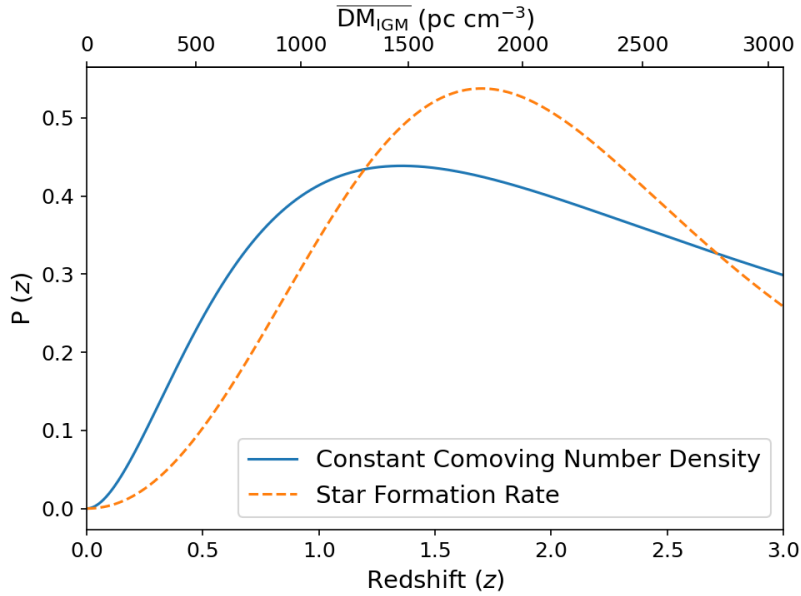


**Figure 5.1:** Probability density function of source redshift for two models of the FRB population. The two distributions correspond to comoving number density of FRBs being constant or following the star formation rate (see §5.3.1). The top x-axis translates redshift to the mean DM contribution of the intergalactic medium. (see §5.4.2).

follows the star-formation rate, motivated by emission models which suggest that FRBs could originate from young stars (see, e.g., Connor et al. 2016; Margalit & Metzger 2018). For this model, the probability of detecting an FRB at a redshift  $z$  is given by

$$P(z) \propto \frac{(1+z)^{2.7}}{1 + [(1+z)/2.9]^{5.6}} \frac{1}{1+z} \frac{dV_C}{d\Omega dz}, \quad (5.2)$$

where the additional pre-factor describes the variation in the comoving star-formation rate with redshift (Madau & Dickinson, 2014). The probability density functions for the two

models are plotted in Figure 5.1.

We simulate FRBs up to a maximum redshift of  $z = 3$  for both models. This choice is informed by the maximum possible redshift calculated using the [Macquart et al. \(2020\)](#) relation for the highest-DM event in Catalog 1. The event, FRB 20180906B, has a measured extragalactic DM of  $3015 \text{ pc cm}^{-3}$ , which translates to a maximum redshift of 2.95. The maximum redshift of 3 is a conservative assumption as approximately half of the CHIME-detected FRBs are at redshifts  $< 0.5$  ([CHIME/FRB Collaboration et al., 2021a](#)).

### 5.3.2 Energy

We sample the energy emitted by the simulated bursts in the CHIME band according to the Schechter function ([Schechter, 1976](#)), for which the differential energy distribution is given by,

$$\frac{dN}{dE} \propto E^{-\gamma} \exp\left(-\frac{E}{E_{\max}}\right). \quad (5.3)$$

While a power-law model is widely used to describe the energy distribution of several extragalactic high-energy transients (see, e.g., [Sun et al. 2015](#)), we use the Schechter function as it adds an exponential cutoff to the power-law model. The exponential cutoff above a maximum energy,  $E_{\max}$ , ensures that the total energy emitted by the FRB population ( $\int_0^\infty E (dN/dE) dE$ ) does not diverge for  $\gamma < 2$ . To reduce the computational cost incurred in simulating progressively larger number of FRBs with low energies, we also assume a minimum energy,  $E_{\min}$ . While we allow the power-law index of the distribution,  $\gamma$ , to vary for each population model being tested (see §5.5), the minimum and maximum burst energies are held fixed.

We choose the values of  $E_{\min}$  and  $E_{\max}$  by studying the inferred energy distribution of events included in Catalog 1. The isotropic-equivalent energy of each event is inferred using

the expression derived by [Macquart & Ekers \(2018\)](#),

$$E = \frac{4\pi D_L^2 F \Delta\nu}{(1+z)^{2-\alpha}}, \quad (5.4)$$

where  $D_L$  is the luminosity distance to the FRB source,  $F$  is the burst fluence,  $\Delta\nu$  is the observing bandwidth and  $\alpha$  is the spectral index ( $F_\nu \propto \nu^\alpha$ ). We set  $\alpha = 0$  to be consistent with the calibration technique used to measure fluences for the Catalog 1 events. Calibration is performed on a band-averaged time series for each burst and thus involves the implicit assumption of  $\alpha = 0$  ([CHIME/FRB Collaboration et al., 2021a](#)).

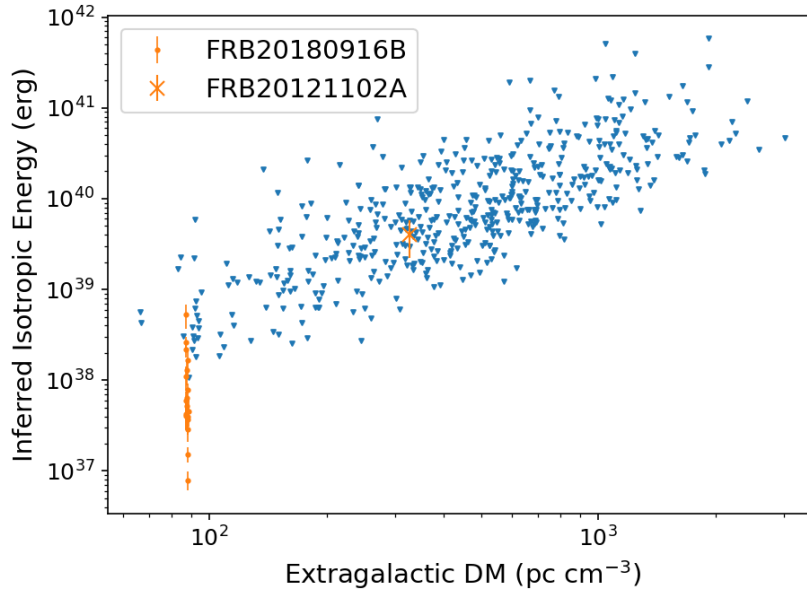


**Figure 5.2:** Inferred isotropic-equivalent energy for Catalog 1 events plotted as a function of their extragalactic DM. Events with measured redshifts are repeaters and are plotted in orange with the error bars corresponding to  $1\sigma$  uncertainties propagated from the fluence measurements. Events plotted in blue do not have corresponding redshift measurements. Their energy is estimated using upper limits on the source redshift and burst fluence (see §5.3.2).

Equation 5.4 requires the redshift to be known, which is the case for only two sources in Catalog 1, FRB20121102A and FRB20180916B ([Tendulkar et al., 2017](#); [Josephy et al., 2019](#); [Marcote et al., 2020](#)). For these sources, we compute burst energies with the associated

uncertainties being propagated from the fluence measurements. For all other sources, i.e., those with undetermined redshifts, we compute a maximum energy by ascribing the excess DM to the IGM and calculating a maximum possible redshift using the Macquart relation (Macquart et al., 2020). The inferred burst energies are plotted in Figure 5.2.

Based on the inferred energy distribution, we adopt a value of  $10^{42}$  erg for  $E_{\max}$ . We note that the fluence measurements in Catalog 1 are biased low as they are derived assuming the burst is detected along the meridian, which is the most sensitive location along the transit path. This effect is not accounted for in the fluence uncertainties, thereby causing the maximum inferred energy to not be a true upper bound. Therefore, we re-examine the assumed value of  $E_{\max}$  in §5.6.1. We choose the value of  $E_{\min}$  based on the inferred energies for the two sources with measured redshifts. While the lowest inferred energy is  $7 \times 10^{36}$  erg, we adopt a more conservative value of  $10^{36}$  erg for  $E_{\min}$ .

### 5.3.3 Sky Location

We simulate sky locations in order to determine the contribution of the Milky Way to the burst DMs and scattering timescales. Burst locations are simulated based on the exposure of the CHIME/FRB system during the observing duration for Catalog 1 (2018 July 25 to 2019 July 1). Since the sky exposure does not vary significantly with right ascension, we sample the burst right ascensions from a uniform distribution. However, the exposure varies significantly with declination, with sky locations at  $\delta > +70^\circ$  transiting through the field of view twice per day.

In order to characterize the variation in the total exposure of the CHIME/FRB system as a function of declination, we first co-add exposure maps for the two transits provided by CHIME/FRB Collaboration et al. (2021a). While the native resolution of this combined map is 0.7 sq. arcminutes, we downsample the map to a resolution of 1 sq. deg. in order to smooth over the small-scale features such as zero exposure in the gaps between synthesized beams. We then marginalize the resulting map over right ascension to obtain the exposure as

a function of declination. Multiplying this function with a cosine function, which describes the variation in sky area with declination, provides us with a probability distribution. We sample burst declinations in accordance with this probability distribution, which is shown in Figure 5.3. We note that we do not consider variation in sensitivity with declination or across beams and transits while simulating burst locations, as the selection-corrected distributions of observed properties, which the simulated distributions will be compared to, account for bursts detected in locations with different sensitivities.

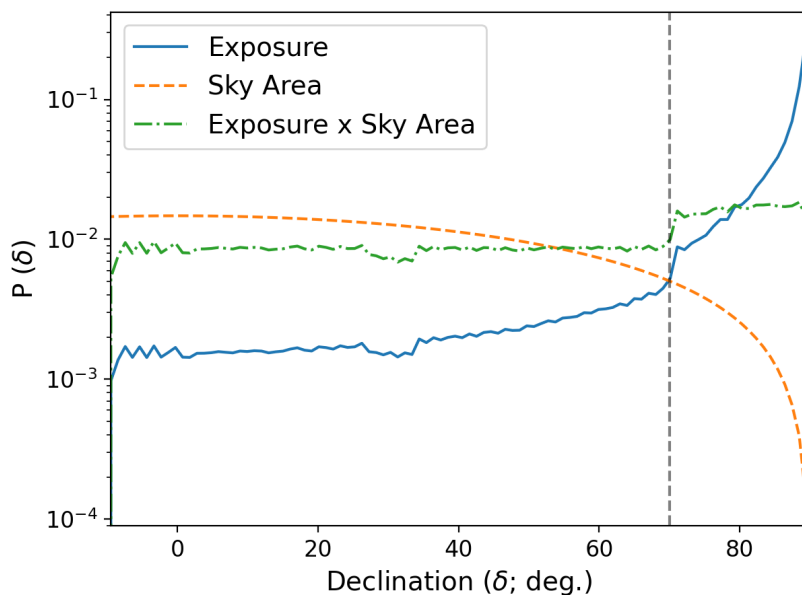


**Figure 5.3:** Probability density function (PDF) of burst declinations sampled based on the sky exposure of the CHIME/FRB system. The exposure marginalized over right ascension is plotted in blue while the orange curve shows variation of sky area with declination. The simulated FRB distribution follows the product of these two PDFs represented by the green curve. The dashed grey line marks the declination at which the exposure doubles due to circumpolar sources being visible in two transits.

## 5.4 Modelling Propagation Effects

We generate the DMs and scattering timescales of simulated FRBs by modelling the different media through which FRB signals propagate. The DM of each burst is equal to the integrated

electron density ( $n_e$ ) along the line of sight and is modelled as,

$$\text{DM}_{\text{total}} = \int_0^D n_e ds = \text{DM}_{\text{MW}} + \text{DM}_{\text{IGM}} + \frac{\text{DM}_{\text{Host}}}{(1+z)} + \frac{\text{DM}_{\text{Local}}}{(1+z)}, \quad (5.5)$$

where the subscripts ‘MW’, ‘IGM’, ‘Host’ and ‘Local’ stand for the Milky Way, the intergalactic medium, host galaxy and local environment of the FRB source, respectively. Assumed models of electron density for each of these media are described in the following subsections. The DM contribution of the host galaxy and the circumburst environment are both reduced by a factor of  $(1+z)$  to account for the combined effect of time dilation of the dispersive delay and photon redshift (Ioka, 2003).

We simulate the phenomenon of scattering using the prescription provided by Cordes & Lazio (2002). They model electron density fluctuations ( $\delta n_e$ ) in the intervening inhomogeneous plasma as having a power-law wavenumber ( $q$ ) spectrum,

$$P_{\delta n_e}(q) = C_n^2 q^{-\beta}, \quad (5.6)$$

where  $C_n^2$  is the spectral coefficient and denotes the level of turbulence. The inner and outer scale of these fluctuations are denoted by  $l_i = 2\pi/q_i$  and  $l_o = 2\pi/q_o$ , respectively, and  $\beta$  is set to be equal to  $11/3$  for a Kolmogorov wavenumber spectrum. Based on this prescription, we can evaluate the scattering time ( $\tau$ ) using the following expression (Blandford & Narayan, 1985; Cordes et al., 2016),

$$\tau = \frac{1}{2c} \int_0^{D_A} ds \eta(s) s(1 - s/D_A) \quad (5.7)$$

$$= \frac{3\Gamma(7/6)\lambda^4 r_e^2 q_i^{1/3}}{2c} \int_0^{D_A} ds s(1 - s/D_A) C_n^2. \quad (5.8)$$

Here  $\eta$  is the mean-square scattering angle per unit distance, which we express in Equation 5.8 in terms of  $C_n^2$  following Appendix B of Cordes et al. (2016). Additionally,  $c$  is the speed of light,  $\Gamma$  is the gamma function,  $\lambda$  is the observing wavelength (corresponding to a

frequency of 600 MHz),  $r_e$  is the classical electron radius and  $D_A$  is the angular diameter distance to the source. Following Cordes et al. (2016), we set the inner scale,  $q_i$  to be equal to  $10^3$  km. The finite wavenumber cutoff associated with the inner scale results in a power-law index of  $-4$  for the frequency dependence, as opposed to the canonical value of  $-4.4$  for a Kolmogorov medium with a negligible inner scale (Bhat et al., 2004).

The models of electron density assumed for different media can also be used to ascertain scattering measures (SM). The SM integrates the amplitude of the turbulence over the path length that the FRB signal passes through and is estimated using the following equation presented by Cordes & Lazio (2002),

$$SM = 6 \int_0^{D_A} ds (s/D_A) (1 - s/D_A) C_n^2. \quad (5.9)$$

Analogous to the total DM, we obtain the total SM by adding the contributions of all intervening media,

$$SM_{\text{total}} = SM_{\text{MW}} + SM_{\text{IGM}} + \frac{3SM_{\text{Host}}}{(1+z)^3} + \frac{6SM_{\text{Local}}}{(1+z)^3}. \quad (5.10)$$

We increase  $SM_{\text{Host}}$  and  $SM_{\text{Local}}$  by a factor of 3 and 6, respectively, to account for the increased broadening caused by plane waves from extragalactic sources as compared to spherical waves from sources within the Milky Way (Cordes et al., 2016). The factor of  $(1+z)^3$  in the terms for scattering media at the source redshift corrects for the dilation of the scattering timescale and the observing frequency being redshifted as compared to the emission frequency (Macquart & Koay, 2013). The total SM of each FRB is calculated based on its simulated redshift. The SM is then substituted in Equation 8 to calculate a scattering time after appropriately accounting for the prefactors.

### 5.4.1 Milky Way

We estimate the contribution of the Milky Way to the dispersion and scattering measures using the NE2001 model of electron density (Cordes & Lazio, 2002). The software implementation of the model integrates the electron density up to a galactocentric radius of 50 kpc, which is greater than the size of any modelled components, thereby providing the maximum possible values for  $DM_{MW}$  and  $SM_{MW}$ .

We note that we do not use the more recent YMW16 model (Yao et al., 2017) as it derives Galactic scattering times using a  $\tau$ -DM relation instead of modelling electron density fluctuations. As the scattering time depends on a geometrical weighting factor,  $s(1 - s/D)$ , it varies with the location of the scattering material ( $s$ ) and the source (see Equation 5.7). Galactic scattering time evaluated using the YMW16 model needs to be corrected for this weighting factor, which requires an assumption to be made about the location of the scattering material. We refrain from making this assumption as the material is likely distributed along the path length through the Galaxy.

In addition to the components of the ISM included in the NE2001 model, we simulate the DM contributed from the halo of the Milky Way. The DM of the Galactic halo,  $DM_{MW,Halo}$ , is greatly uncertain with estimates spanning  $\sim 10$ – $100 \text{ pc cm}^{-3}$  (Dolag et al., 2015; Prochaska & Zheng, 2019; Keating & Pen, 2020). We initially assume  $DM_{MW,Halo} = 30 \text{ pc cm}^{-3}$  based on the results of Dolag et al. (2015). We examine the effect of this assumption on our results in §5.6.1. We do not simulate the scattering contribution of the halo as it is constrained to be at least an order of magnitude lower than the temporal resolution of the CHIME/FRB system (Ocker et al., 2021).

### 5.4.2 Intergalactic Medium

The contribution of the IGM to the DMs of FRBs can be calculated using the Macquart relation, which relates the source redshift to  $DM_{IGM}$  (Macquart et al., 2020). There is significant scatter in this relation due to the inhomogeneity of the IGM with a majority of

sightlines intersecting galaxy halos (McQuinn, 2014). To account for these sightline variations, we sample the  $DM_{\text{IGM}}$  for each simulated FRB from a normal distribution with the mean calculated as per Zheng et al. (2014),

$$\overline{DM_{\text{IGM}}} \cong n_0 f_e D_L [1 + 0.932z + (0.16\Omega_m - 0.078)z^2]^{-0.5} \quad (5.11)$$

where  $n_0$  is the mean number density of nucleons at  $z = 0$ ,  $f_e$  is the fraction of baryons in an ionized state and  $\Omega_m$  is the matter density in units of the critical density at  $z = 0$ . The top x-axis in Figure 5.1 shows the variation in  $DM_{\text{IGM}}$  as a function of redshift. The standard deviation of the aforementioned normal distribution is obtained from cosmological simulations performed by McQuinn (2014, see Figure 1 of their paper) for  $z < 1.5$ . The standard deviation varies from  $\sim 50\%$  at  $z = 0.1$  to  $\sim 20\%$  at  $z = 1.5$ . For simulated FRBs with  $z > 1.5$ , we assume a standard deviation of 20%.

We do not simulate scatter-broadening caused by the IGM and set  $SM_{\text{IGM}} = 0$ . This choice is motivated by the expected scattering time at 600 MHz, derived based on the turbulence injection scale associated with cosmic structure formation, being at least an order of magnitude lower than the sampling time of the CHIME/FRB system (Macquart & Koay, 2013; Zhu et al., 2018).

### 5.4.3 Host Galaxy

We simulate FRBs in different types of host galaxies, namely, spiral, elliptical and dwarf galaxies. We adopt different models of electron density for each galaxy type, which are described in the following subsections. Additionally, we assume that the inclination angles of these host galaxies are uniformly distributed, with the probability of having an inclination angle  $i$ ,  $P(i) \propto \sin(i)$ . For each FRB, we randomly sample an inclination angle in the range,  $0 \leq i \leq \pi/2$ , based on the aforementioned probability. We do not simulate inclination angles with values between  $\pi/2$  and  $\pi$  as the assumed electron density models are symmetric about

the plane of the galaxy.

We simulate  $10^4$  FRB locations within the host for each galaxy type. The assumed distributions of FRB locations are also described in the following subsections. We then estimate  $DM_{\text{host}}$  and  $SM_{\text{host}}$  for these  $10^4$  sightlines through the host galaxy by integrating over the electron density distribution from the event location to the near edge of the host galaxy. The resulting distributions of DMs and scattering times are shown in Figure 5.4. Additionally, we add the DM expected from the halo of the host galaxy to  $DM_{\text{host}}$ . Analogous to the Milky Way, we assume  $DM_{\text{Host,Halo}} = 30 \text{ pc cm}^{-3}$ . We make this assumption for all galaxy types as the electron distribution in the halos of dwarf and elliptical galaxies is poorly understood.

While the known sample of FRB host galaxies is morphologically diverse (Heintz et al., 2020), we initially test population models where all FRBs are located in host galaxies of the same type. However, we repeat our analysis for models where FRBs exist in more than one type of host galaxy and present the results in §5.6.4.

### Spiral Galaxies

We assume that all spiral galaxies have electron density distributions similar to the Milky Way and use the prescription from the NE2001 model to simulate the electron density in the thin disk, thick disk, spiral arms and galactic centre (see Table 2 of Cordes & Lazio 2002). In using the NE2001 model to simulate the electron density of the host galaxy, we implicitly assume that the amplitude of turbulence ( $C_n^2$ ) and inner scale of the fluctuations in electron density,  $l_i$ , are the same as those assumed for the Milky Way by Cordes & Lazio (2002). As noted earlier, we do not use the YMW16 model to simulate the host galaxy, as Yao et al. (2017) use a  $\tau$ -DM relation (as described in §5.4.1) to obtain the scattering time. As this relation is based on Galactic pulsars observed from the Earth, it is valid for sightlines passing through the plane of the host galaxy. Since we simulate host galaxies at random inclination angles, not all sightlines would pass through the plane, implying that this relation would

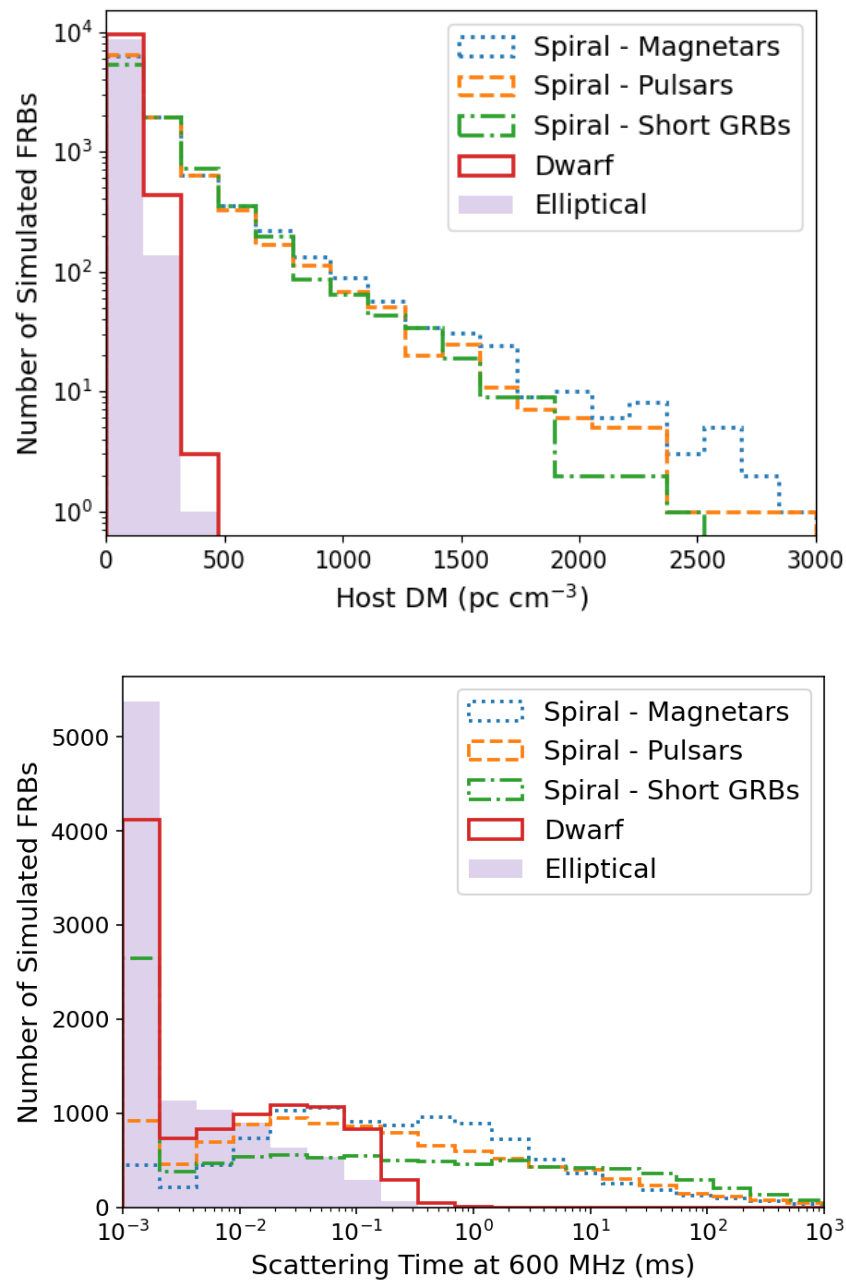


**Figure 5.4:** Histogram of the host DMs and scattering times for  $10^4$  simulated FRBs located in different types of host galaxies, namely spiral, dwarf and elliptical galaxies. Spatial distributions of FRBs within the host galaxy are described in §5.4.3. Three distributions are considered for spiral galaxies, which emulate the magnetar, pulsar and short GRB populations. For visualization purposes, scattering times  $< 10^{-3}$  ms are set to be equal to  $10^{-3}$  ms in the bottom panel.

overestimate the pulse broadening.

The distribution of host DMs and scattering times could be influenced by the size distribution of the host galaxies. We assign a radius to each spiral host galaxy by first sampling a galaxy mass and then using the mass-radius relationship provided by [Shen et al. \(2003\)](#),

$$R \text{ (kpc)} = 0.1 \left( \frac{M}{M_{\odot}} \right)^{0.14} \left( 1 + \frac{M}{4 \times 10^{10} M_{\odot}} \right)^{0.25}. \quad (5.12)$$

Here  $R$  is the galaxy half-light radius and  $M$  is the galaxy stellar mass. We sample the galaxy mass using the stellar mass function of star-forming galaxies, located at  $z \sim 0.1$ , provided in Table 3 of [Moustakas et al. \(2013\)](#). In doing so, we assume that the rate of FRB occurrence within a galaxy is proportional to its stellar mass. We then derive a radius for each host galaxy based on Equation 5.12, and scale all modelled electron density structures by a factor of  $(R/R_{\text{MW}})$ . Here  $R_{\text{MW}}$  is the effective radius of the Milky Way and is set to be equal to 2.5 kpc ([van den Bergh, 1999](#)).

We simulate three spatial distributions of FRBs within a spiral host, modifying any length scales for these distributions by a factor of  $(R/R_{\text{MW}})$ . The three distributions are motivated by progenitor models involving isolated pulsars ([Connor et al., 2016](#); [Cordes & Wasserman, 2016](#)), isolated magnetars ([Metzger et al., 2019](#)) and merging neutron stars ([Totani, 2013](#); [Wang et al., 2016](#); [Margalit et al., 2019](#)). For all of these spatial configurations, we sample the source height above the plane of the host galaxy from an exponential distribution. The scale heights of these exponential distributions are set to be equal to those inferred from the observed Galactic population of these sources using population synthesis analyses. We assume a scale height of 30 pc for the magnetar population ([Olausen & Kaspi, 2014](#)), 330 pc for the pulsar population ([Lorimer et al., 2006](#)) and 800 pc for binary neutron star systems ([Kiel et al., 2010](#)).

For the pulsar and magnetar models, we simulate FRBs along the spiral arms of the host galaxy. This is motivated by the results of a population synthesis analysis performed by [Faucher-Giguère & Kaspi \(2006\)](#) and we use the methodology described in §3.1.2 of their

paper. In summary, the galactocentric radii of simulated FRBs are sampled from a radial distribution for which the surface density peaks at 3 kpc. The azimuthal angle of each FRB is sampled in a way that it falls on the centroids of the spiral arms, locations of which are consistent with those used in the NE2001 model.

For the model in which FRBs are associated with binary neutron star mergers, we simulate the galactocentric radius based on the corresponding distribution observed for short gamma-ray bursts, which exhibit large offsets from the centres of their host galaxies. We sample the radius of the simulated FRBs using the cumulative distribution function (CDF) of host-normalized offsets ( $r/R$ ) provided by [Fong & Berger \(2013\)](#).

### Elliptical Galaxies

While we have a prior on the electron density distribution in spiral galaxies owing to extensive modelling of the Milky Way, the corresponding distribution for elliptical galaxies is not well understood. Although some theoretical models provide a functional form for the variation in electron density with radius (see, e.g., [Seta et al. 2021](#)), they do not include a prescription for the scattering properties of elliptical galaxies. Therefore, we follow [Xu & Han \(2015\)](#) in modelling an elliptical galaxy using the thick disk and galactic centre components of the NE2001 model, using which we can ascertain both dispersive and scattering properties.

This approach makes an implicit assumption that the elliptical galaxy is the same size as the Milky Way. However, we reduce the free electron density by a factor of  $\sqrt{10}$  in order to account for the lack of ionized gas in elliptical galaxies. This factor is derived based on the  $H\alpha$  luminosity for an average elliptical galaxy being an order of magnitude lower than the inferred luminosity for the Milky Way ([James et al., 2004](#)). As the  $H\alpha$  luminosity is a tracer of ionized hydrogen, it is proportional to  $\int n_e^2 dV$ , implying that the free electron density is proportional to the square root of the total  $H\alpha$  luminosity emitted by the galaxy.

We assume a population of FRBs within the galaxy with a scale height and radial distribution the same as that inferred for the short GRB population, described in §5.4.3.

The resulting DM and scattering time distributions are shown in Figure 5.4. We note that we do not simulate other spatial distributions of FRBs in elliptical galaxies. Another caveat is that reducing the free electron density across the galaxy by a factor based on the  $H\alpha$  luminosity assumes that the distribution of ionized hydrogen in elliptical galaxies is similar to that for the Milky Way. This factor could be different if a significant fraction of the  $H\alpha$  emission originates in small-scale structures such as HII regions. Assuming a different spatial distribution for FRBs or correction factor for the  $H\alpha$  luminosity is unlikely to significantly change our results. This is because the contribution of an elliptical host galaxy to the total DM and SM will be significantly lower than that of other media, regardless of the assumed parameters.

### Dwarf Galaxies

We model dwarf galaxies using the prescription for the electron density distribution in the Large Magellanic Cloud (LMC) proposed by Yao et al. (2017). Although the LMC is not representative of the full population of dwarf galaxies, observations of radio pulsars have enabled modelling of its electron density distribution. Since similar studies have not been conducted for other galaxies, we use the LMC as a prior for all dwarf galaxies.

Based on DMs observed for 23 pulsars in the LMC, Yao et al. (2017) model it as a disk with exponentially decreasing electron density away from the plane of the galaxy and a Gaussian distribution in the radial direction. The scale height for the exponential fall-off is 0.8 kpc and the standard deviation for the Gaussian function is 3 kpc. We assume the vertical heights and galactocentric radii of the simulated FRBs to follow an exponential and Gaussian distribution, respectively. The parameters of these distributions are set to be the same as those for the assumed electron density distribution. While integrating over this electron density distribution to calculate the SM of a simulated FRB, we assume the turbulence to be the same as that for the thick disk of the Milky Way since the scattering properties of the LMC are not well understood. This is done by setting  $C_n^2$  in Equation 5.9

to be the same as that for the thick disk in the NE2001 model.

We note that we do not implement a distribution of galaxy radii for dwarf or elliptical galaxies as the total DM and scattering time distribution is not expected to change significantly by varying the sizes of these galaxies. This is because the contribution of these galaxy types to the total DMs of simulated FRBs is much lower than the expected IGM contribution. Additionally, the simulated host scattering times, as shown in Figure 5.4, are lower than the temporal resolution of the CHIME/FRB instrument.

#### 5.4.4 Circumburst Environment

The local environment of an FRB source could contribute significantly to its observed DM, as has been suggested for models in which FRBs are produced by young neutron stars (see, e.g., [Connor et al. 2016](#); [Piro 2016](#)). However, these works do not provide an estimate of the scatter-broadening caused by high electron density local environments. The NE2001 model of electron density in the Milky Way provides empirical estimates of local DM and SM (hereafter  $DM_{\text{clump}}$  and  $SM_{\text{clump}}$ ) for  $\sim 100$  Galactic pulsars ([Cordes & Lazio, 2003](#)). [Cordes & Lazio \(2003\)](#) note that most of these clumps are not associated with known HII regions or supernova remnants and hence might not be an adequate measure of the dispersive or scattering properties of such environments. Nevertheless, in the absence of theoretical estimates, we choose to use these empirically derived values as a prior on the scattering properties of HII regions and supernova remnants.

We sample the DM of the local environment,  $DM_{\text{Local}}$ , from a log-normal distribution. The parameters of this distribution are based on the distribution of  $DM_{\text{clump}}$  values modelled by [Cordes & Lazio \(2003\)](#). The mean and standard deviation of the underlying normal distribution are 0.18 and 1.09, respectively. The DM values are generated within  $2\sigma$  of the mean of the normal distribution. Simulated values of  $DM_{\text{Local}}$  range from 0.1 to  $\sim 300$   $\text{pc cm}^{-3}$ . The distribution of  $DM_{\text{clump}}$  and  $DM_{\text{Local}}$  are shown in Figure 5.5. In order to estimate  $SM_{\text{Local}}$  from the corresponding  $DM_{\text{Local}}$  for each simulated FRB, we first model the

relationship between  $SM_{\text{clump}}$  and  $DM_{\text{clump}}$  with a power law using an ordinary least squares regression (see, e.g., [Isobe et al. 1990](#)). We then calculate  $SM_{\text{Local}}$  using this power-law model, but allow for scatter in the SM values based on the prediction interval for the least squares regression. The confidence and prediction intervals are shown in Figure 5.5. While the confidence interval represents the uncertainty in the fit, the prediction interval accounts for the scatter in the dependent variable ( $SM_{\text{clump}}$ ) and indicates the range in which a future observation will lie.

We test another configuration in which the circumburst environment has more extreme properties than those assumed above. This is done by setting a minimum threshold for  $DM_{\text{Local}}$ . While sampling local DMs for this configuration, DMs lower than the threshold are rejected and redrawn. We initially assume a threshold of  $10 \text{ pc cm}^{-3}$  but examine the effect of increasing the threshold in §5.6.2. The scattering measure,  $SM_{\text{Local}}$ , is derived using the same method as described above.

#### 5.4.5 Intervening Galaxies

The line of sight to an FRB could also intersect one or more galaxy halos. While the DM contribution of such halos is accounted in the scatter in the Macquart relation (see §5.4.2), we model the scattering times using the formalism proposed by [Vedantham & Phinney \(2019\)](#). Their model suggests that sub-parsec scale cool ionized gas clumps ( $T \sim 10^4 \text{ K}$ ) in the circumgalactic media (CGM) of intervening galaxies could contribute to FRB scattering.

The scattering time in this model depends on the volume fraction of the cool gas clumps ( $f_v$ ), the fraction of baryons in the CGM ( $f_{\text{CGM}}$ ) and the source redshift. Additionally, the scattering time for two sources at the same redshift could vary by several orders of magnitude depending on the number of galaxy halos their sightlines intersect, masses and redshifts of these halos and the impact parameter to the centre of the galaxy. [Vedantham & Phinney \(2019\)](#) account for the aforementioned variables to derive an expression for the fraction of sightlines (referred to as the areal covering factor) for which the scattering time exceeds any

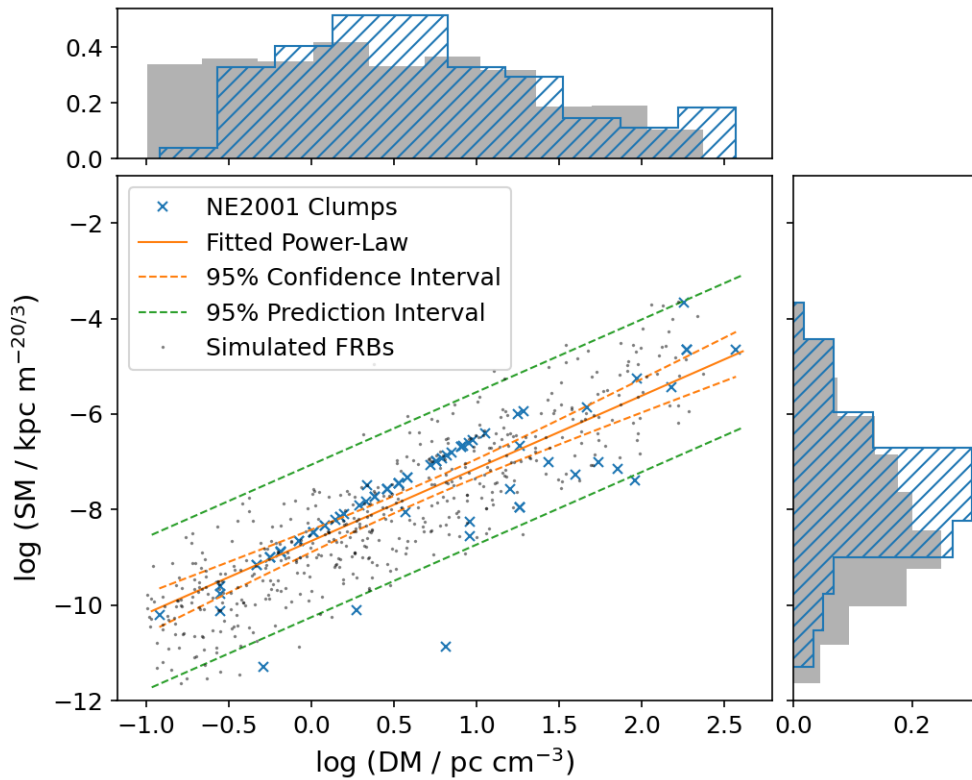


**Figure 5.5:** Dispersion and scattering measures for local environments of simulated FRBs in this work and for regions of intense scattering modelled as electron density clumps in the NE2001 model (see §5.4.4). Histograms of the distribution of local DMs for the simulated FRBs (in grey) and for the NE2001 clumps (in blue) are plotted in the top panel while the corresponding histograms for the local SMs are shown in the right panel. The DMs of the simulated FRBs are drawn from a log-normal distribution and the SMs are estimated using a power-law model fit to the DM and SM of the NE2001 clumps. The power-law model with the  $2\sigma$  confidence interval for the fit is plotted in orange. The scatter in the SMs for the simulated FRBs is dictated by the prediction interval, the bounds for which are shown by the dashed green lines.

given value of  $\tau$  (see Figure 8 of their paper). The differential of the areal covering factor with respect to  $\tau$  provides the probability density function for  $\tau$ . We sample the scattering time of each FRB based on this probability density function evaluated at the simulated source redshift.

Vedantham & Phinney (2019) note that their model is simplistic with many assumptions and that the values of several key parameters such as  $f_v$  and  $f_{\text{CGM}}$  are poorly

constrained. The existence of cool gas in galaxy halos has been inferred through quasar absorption spectroscopy, which only measures the column density of the gas (Tumlinson et al., 2017). The volume fraction,  $f_v$ , is estimated using photo-ionization modelling and thus has significant uncertainties (see Table 1 of McCourt et al. 2018). Moreover, spectroscopic and imaging observations cannot probe structures of sub-parsec sizes, making it difficult to confirm whether the gas clumps are compact enough to cause intense scattering.

As the validity of the model is uncertain, we perform our population synthesis analysis for two scenarios, with and without scattering originating in the CGM of intervening galaxies. For the former scenario, we test two configurations corresponding to 30% and 60% of baryons in the CGM, i.e.,  $f_{CGM} = 0.3$  and  $0.6$ , setting  $f_v = 10^{-4}$  for both these configurations. We choose these two configurations as they can explain scattering observed for FRBs at 1.4 GHz, as noted by Vedantham & Phinney (2019). The scattering time is proportional to  $(f_{CGM})^{3.2}$  and hence varies by an order of magnitude, on average, between the two configurations. Models with  $f_{CGM} > 0.6$  are disfavoured by Vedantham & Phinney (2019) based on the observed scattering of FRBs at 1.4 GHz.

## 5.5 Simulation Procedure

We test different population models of FRBs, which are listed in Table 1, using Monte Carlo simulations. For each population model, we start by simulating properties intrinsic to the source, namely, burst energy, redshift, sky location, and pulse width ( $w_i$ ). We sample pulse widths in accordance with the log-normal function fit to the selection-corrected distribution of intrinsic widths for the Catalog 1 sample. Other intrinsic properties are sampled as described in §5.3. Burst energies are sampled according to the Schechter function (see Equation 5.3) for which the power-law index is initially set to be equal to a fiducial value of 2.

Based on simulated burst energies and redshifts, we calculate band-averaged fluences

for the CHIME band using Equation 5.4. A simulated burst is considered to be detectable if its fluence is greater than 0.4 Jy ms, which is the lowest fluence for any burst in the catalog. We choose this threshold knowing that selection effects for the catalog have been adequately characterized above this fluence, thereby allowing a robust comparison of the simulated distributions with the selection-corrected distributions. Previous population synthesis studies (see, e.g., [Caleb et al. 2016](#); [Gardenier et al. 2019](#)) implement a fluence threshold dependent on the pulse width, scattering time and DM, determined using the radiometer equation. Since an absolute calibration of selection effects is performed for Catalog 1, we do not use the radiometer equation as an approximation for the sensitivity of the CHIME/FRB system.

We simulate  $10^4$  bursts for each population model, the DMs and scattering times for which are sampled using the prescriptions provided in §5.4. All DMs and scattering times include the contribution of the Milky Way, the host galaxy and the IGM. While the contributions of the Milky Way and the IGM are derived based on simulated sky locations and redshifts, the host galaxy contribution is simulated for  $10^4$  different sightlines (see §5.4.3). Contributions of intervening galaxies and local environments are added if the population model in consideration requires them.

In order to compare the simulated DM and scattering distributions with Catalog 1, we perform the same set of cuts on these distributions as in the catalog. This involves excising bursts with  $DM < 100 \text{ pc cm}^{-3}$  or  $DM < 1.5$  times the maximum of the Galactic DM estimates obtained from the NE2001 and YMW16 models (see §5.2). Additionally, we excise all bursts with  $\tau_{600 \text{ MHz}} > 100 \text{ ms}$ , as selection effects for the catalog have not been assessed beyond this timescale ([CHIME/FRB Collaboration et al., 2021a](#)). Since 95% of Catalog 1 bursts survived these three cuts, we redraw DMs and scattering times for bursts which are rejected until the surviving simulated sample contains at least 9500 bursts.

We also apply two corrections to the simulated distributions to emulate the constraints in measuring widths and scattering times for the Catalog 1 sample. The first of these corrections

concerns narrow bursts for which intrinsic widths are difficult to discern due to dispersive smearing and scatter broadening. Simulated bursts with  $w_i < 0.1$  ms are set to have widths equal to 0.1 ms, as [CHIME/FRB Collaboration et al. \(2021a\)](#) report that intrinsic widths lower than this threshold cannot be robustly measured. The second correction is applied to bursts with low scattering times ( $\tau_{400 \text{ MHz}} < w_i$ ), which are difficult to measure using burst-fitting algorithms. For these bursts, we set  $\tau_{600 \text{ MHz}}$  to be equal to half the intrinsic width, as is done for Catalog 1 ([CHIME/FRB Collaboration et al., 2021a](#)).

For each population model, we first compare the simulated DM distribution with the selection-corrected catalog. We generate 100 realizations of the DM distribution for both the catalog and the model. The model distribution includes more than 9500 bursts and thus does not vary significantly between realizations. However, we vary the catalog distribution between realizations to account for the uncertainties shown in Figure 5.6. This is done by randomly sampling the probability density for each DM bin within its 68% confidence interval. Since the post-cut catalog consists of 292 bursts (see §5.2), we sample 292 DM values in accordance with the PDF.

For each realization, we compare the DM distribution for the catalog with the model using a two-sample Kolmogorov-Smirnov (KS) test ([Massey Jr., 1951](#)). If the two distributions are inconsistent with each other, with  $> 3\sigma$  significance, we resample the intrinsic properties, DMs, and scattering timescales for all bursts assuming a different power-law index for the energy distribution. The power-law index is varied in steps of 0.01 until the two DM distributions are found to be consistent. For most population models, we converge on a power-law index for which the simulated DM distribution is consistent with the catalog. We do not proceed with the scattering time comparison for models which fail to converge.

We compare the scattering time distribution for 100 realizations of the converged models with the catalog using both the KS and the Anderson-Darling (AD) tests ([Scholz & Stephens, 1987](#)). The probability density function for the selection-corrected scattering

time distribution for Catalog 1 has fairly large uncertainties particularly longward of 10 ms, as shown in Figure 5.6. Therefore, for each of the 100 catalog realizations, we randomly sample the probability density in each scattering time bin within its 68% confidence interval. We sample 292 scattering timescales based on the resulting PDF and compare these scattering times with the simulated sample of  $> 9500$  bursts. We report the results from these statistical tests in Table 5.1.

## 5.6 Results and Discussion

We conclude that a model is able to reproduce the catalog if at least one of 100 Monte Carlo realizations of the DM and scattering distributions for the model is found to be consistent with the corresponding distributions for Catalog 1. The criteria for consistency is finding no significant differences between the observed and simulated distributions at  $> 3\sigma$  confidence level with both KS and AD tests. Among the several models being tested (see Table 5.1), we find that only one population model is able to reproduce the observed properties in Catalog 1. The model that we cannot rule out corresponds to an FRB population hosted in spiral galaxies with a spatial distribution within the host resembling that of the short GRB population. The model also includes scattering arising both in the local environment ( $\text{DM}_{\text{Local}} > 10 \text{ pc cm}^{-3}$ ) and in intervening galaxies ( $f_{\text{CGM}} = 0.6$ ). Additionally, the model assumes that the FRB population evolves with redshift in a manner consistent with the star formation rate.

For this model, the mean p-value is  $10^{-4}$  for the KS test comparing the simulated scattering time distribution with the catalog. While this value is lower than the threshold for  $3\sigma$  confidence, we do not reject the model as we are performing multiple statistical tests using the same data. Testing multiple hypotheses increases the chances of observing a rare event, thereby requiring a lower p-value threshold to claim an inconsistency between the model and the data. The modified threshold is evaluated using the Bonferroni correction

DM <sub>Local</sub> (pc cm <sup>-3</sup> )		-		-		> 0.1 <sup>a</sup>		> 10 <sup>a</sup>		
Intervening Galaxies (f <sub>CGM</sub> ) <sup>b</sup>	Host Galaxy	-	0.3	0.6	-	0.3	0.6	-	0.3	0.6
Redshift Dist.	Host Galaxy									
Constant	Elliptical	10 <sup>-82</sup>	10 <sup>-42</sup>	10 <sup>-17</sup>	10 <sup>-77</sup>	10 <sup>-46</sup>	10 <sup>-15</sup>	10 <sup>-39</sup>	10 <sup>-19</sup>	10 <sup>-8</sup>
Number	Dwarf	10 <sup>-83</sup>	10 <sup>-53</sup>	10 <sup>-25</sup>	10 <sup>-62</sup>	10 <sup>-35</sup>	10 <sup>-21</sup>	10 <sup>-41</sup>	10 <sup>-15</sup>	10 <sup>-10</sup>
Density	Spiral - Short GRBs	10 <sup>-41</sup>	10 <sup>-22</sup>	10 <sup>-15</sup>	10 <sup>-32</sup>	10 <sup>-19</sup>	10 <sup>-10</sup>	10 <sup>-17</sup>	10 <sup>-7</sup>	10 <sup>-6</sup>
	Spiral - Pulsars	10 <sup>-53</sup>	10 <sup>-30</sup>	10 <sup>-20</sup>	10 <sup>-37</sup>	10 <sup>-23</sup>	10 <sup>-13</sup>	10 <sup>-24</sup>	10 <sup>-10</sup>	10 <sup>-8</sup>
	Spiral - Magnetars	10 <sup>-45</sup>	10 <sup>-36</sup>	10 <sup>-31</sup>	10 <sup>-44</sup>	10 <sup>-20</sup>	10 <sup>-21</sup>	...	10 <sup>-15</sup>	10 <sup>-11</sup>
	Dwarf	10 <sup>-110</sup>	10 <sup>-44</sup>	10 <sup>-19</sup>	10 <sup>-75</sup>	10 <sup>-31</sup>	10 <sup>-17</sup>	10 <sup>-33</sup>	10 <sup>-20</sup>	10 <sup>-9</sup>
SFR <sup>c</sup>	Spiral - Short GRBs	10 <sup>-42</sup>	10 <sup>-20</sup>	10 <sup>-15</sup>	10 <sup>-35</sup>	10 <sup>-18</sup>	10 <sup>-9</sup>	10 <sup>-15</sup>	10 <sup>-8</sup>	<b>10<sup>-4</sup></b>
	Spiral - Pulsars	10 <sup>-49</sup>	10 <sup>-26</sup>	10 <sup>-14</sup>	10 <sup>-43</sup>	10 <sup>-23</sup>	10 <sup>-15</sup>	10 <sup>-19</sup>	10 <sup>-10</sup>	10 <sup>-12</sup>
	Spiral - Magnetars	10 <sup>-51</sup>	10 <sup>-28</sup>	10 <sup>-19</sup>	10 <sup>-33</sup>	10 <sup>-26</sup>	10 <sup>-12</sup>	10 <sup>-23</sup>	10 <sup>-33</sup>	...

**Notes.**

<sup>a</sup>The DM of the local environment ranges from the minimum reported here to  $\sim 300$  pc cm<sup>-3</sup> and is drawn from a log-normal distribution (§5.4.4).

<sup>b</sup>A dash (-) indicates that the scattering contribution of the CGM of intervening galaxies is assumed to be 0.

<sup>c</sup>For the redshift distribution tracing the star formation rate, we do not test the model in which all FRBs are in elliptical galaxies. The model is not physically motivated due to the low rate of star formation in these galaxies.

**Table 5.1:** P-value for the KS test comparing the selection-corrected scattering time distribution for Catalog 1 and the corresponding simulated distribution for different population models. One hundred realizations are simulated for each model and the simulated scattering distribution is compared to the catalog only if the simulated and observed DM distributions are consistent with each other. The mean p-value for the realizations in which this comparison is performed are reported here. The null hypothesis is that the simulated distribution for a population model is identical to the catalog. The p-value for the model for which at least one of the 100 realizations cannot be ruled out with  $> 3\sigma$  confidence by both KS and AD tests is indicated in bold. The p-value is not available (as indicated by ‘...’) for models for which the simulated DM distributions are found to be inconsistent with Catalog 1 for all trial power-law indices of the burst energy distribution (see §5.5).

(Shaffer, 1995) which involves dividing the threshold for  $3\sigma$  confidence (0.0027) by the total number of tests performed (81; see Table 5.1). The mean p-value for the favoured model is greater than the modified threshold ( $10^{-5}$ ) implying that the model is marginally consistent with the observations. None of the other population models have mean p-values greater than this threshold. We investigate why other models were unable to reproduce our observations in §5.6.2 and §5.6.5.

The simulated DM and scattering distributions for the model we cannot exclude along with the corresponding distributions for Catalog 1 are shown in Figure 5.6 and 5.7. The DM and scattering time distributions for the model are obtained by modelling different intervening media (see §5.4), the contributions of which are shown in Figure 5.8. The conclusion of the aforementioned model being marginally consistent with the observations is subject to various assumptions that we test in §5.6.1. We discuss the constraints we can place on the properties of the intervening media and on FRB progenitor models based on this result in §5.6.2–5.6.5.

### 5.6.1 Varying Assumed Parameters

The results reported in Table 5.1 are derived from simulations of intrinsic and observed properties of FRBs, modelling of which requires many assumptions. We investigate the robustness of our results to some of these assumptions by repeating our analysis for different values of the assumed parameters.

The first set of assumptions is related to measured fluences in Catalog 1 being biased low as they are calculated assuming all bursts are detected at the most sensitive location along their transit. This systematic error propagates through to the assumed value of  $E_{\max}$  for the intrinsic energy distribution chosen based on the inferred energies of Catalog 1 events (as described in §5.3.2). Additionally, this one-sided systematic error also implies that the minimum detectable fluence assumed for the simulations (0.4 Jy ms; lowest-measured fluence in Catalog 1) could be an underestimate.

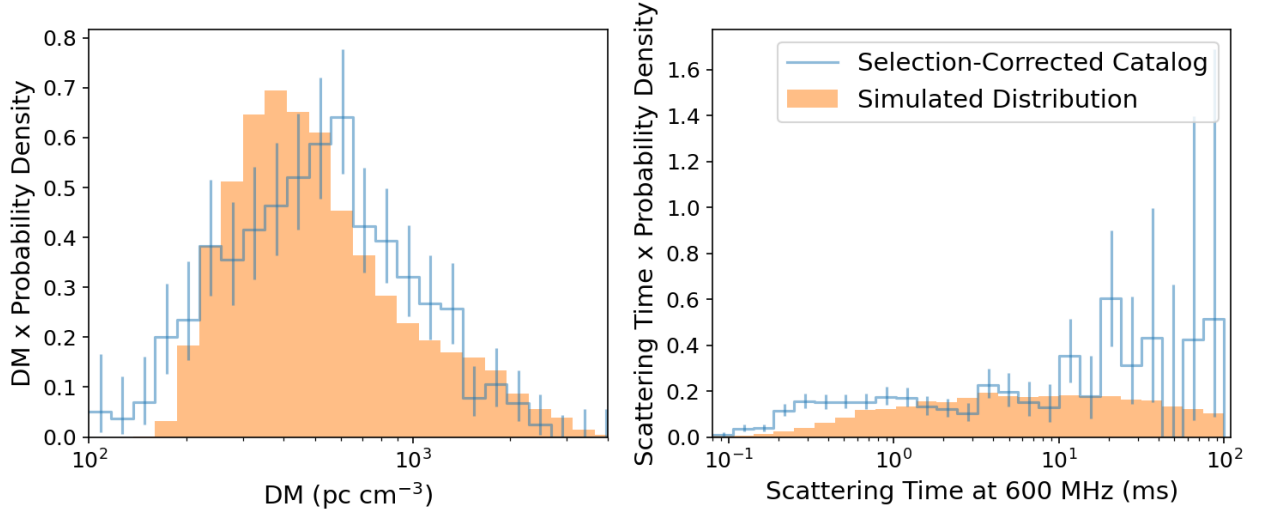


**Figure 5.6:** Dispersion measure and scattering time distributions for Catalog 1 and the population model which we cannot rule out. The model assumes FRBs to be spatially distributed like short GRBs in spiral galaxies. The local environment of the FRB source and the CGM of intervening galaxies are the dominant sources of scattering for this model (see Figure 5.8). The histograms represent the probability density function re-parameterized in terms of the natural logarithm of the two quantities, DM and scattering time. The blue histograms are the catalog data corrected for selection effects with the error bars showing the 68% Poissonian confidence interval for each bin value. The simulation histograms, plotted in orange, show the average PDF over 100 Monte Carlo realizations of the model. While the model does not adequately reproduce the scattering time distribution, it is found to be marginally consistent based on KS and AD tests and thus cannot be ruled out (see Table 5.1). The difference between the probability density function of the simulated and observed scattering distributions for timescales  $< 1$  ms is not significant as is shown by the corresponding cumulative distribution functions plotted in Figure 5.7.

We rerun the simulations for all population models twice, first by setting  $E_{\max}$  to  $10^{46}$  erg as compared to its previously assumed value of  $10^{42}$  erg. In the second iteration, we increase the minimum detectable fluence to twice the previously assumed value, setting it to be 0.8 Jy ms. The results for both these iterations confirm our initial conclusions. We find that a short GRB-like population in spiral galaxies with scattering arising in the local environment ( $DM_{\text{Local}} > 10 \text{ pc cm}^{-3}$ ) and CGM of intervening galaxies ( $f_{\text{CGM}} = 0.6$ ) still remains the only model even marginally consistent with Catalog 1. The other assumed parameter that we vary is the DM contribution of the halo of the Milky Way and the host galaxy. While we initially assumed  $DM_{\text{Halo}} = 30 \text{ pc cm}^{-3}$ , we perform another iteration of the simulations

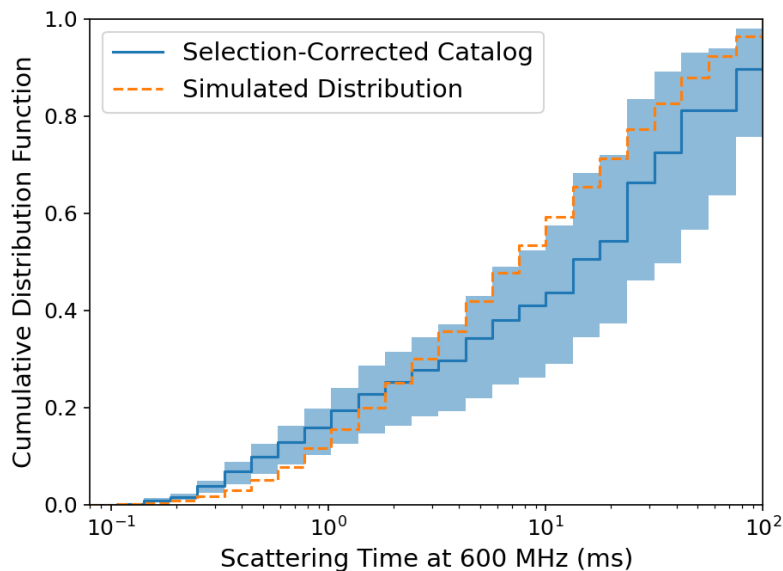


**Figure 5.7:** Cumulative distribution function for the scattering times in Catalog 1 and the model which we cannot rule out. The model assumes that FRBs are spatially distributed like short GRBs in spiral galaxies. The model includes scattering originating in the local environment and in the CGM of intervening galaxies. The CDF for the simulated distribution, plotted in orange, is averaged over 100 Monte Carlo realizations of the model. The simulated distribution is found to be marginally consistent with Catalog 1 based on KS and AD tests. The CDF for the selection-corrected catalog is plotted in blue. Uncertainties on the catalog CDF are determined by generating 100 realizations of the probability density function shown in Figure 5.6. In each realization, the probability density for each scattering time bin is sampled within its 68% confidence interval.

by sampling halo DM uniformly in the range from 50 to 80  $\text{pc cm}^{-3}$  (Prochaska & Zheng, 2019). We find the same model to be flavoured for this iteration as well.

For all population models, the simulated scattering times are compared to catalog measurements which are derived assuming a power-law index of  $-4$  for the frequency dependence. This choice is motivated by the measured scattering indices for pulsars and FRBs. While the mean value measured for 98 Galactic pulsars is  $-3.9 \pm 0.2$  (Bhat et al., 2004), the measured indices for FRBs<sup>2</sup> range from  $-6$  to  $-3.5$  (Petroff et al., 2016). All these measurements are consistent with an index of  $-4$  due to the large associated uncertainties. However, these measurements could also be consistent with an index of  $-4.4$ ,

<sup>2</sup><https://www.frbcat.org>

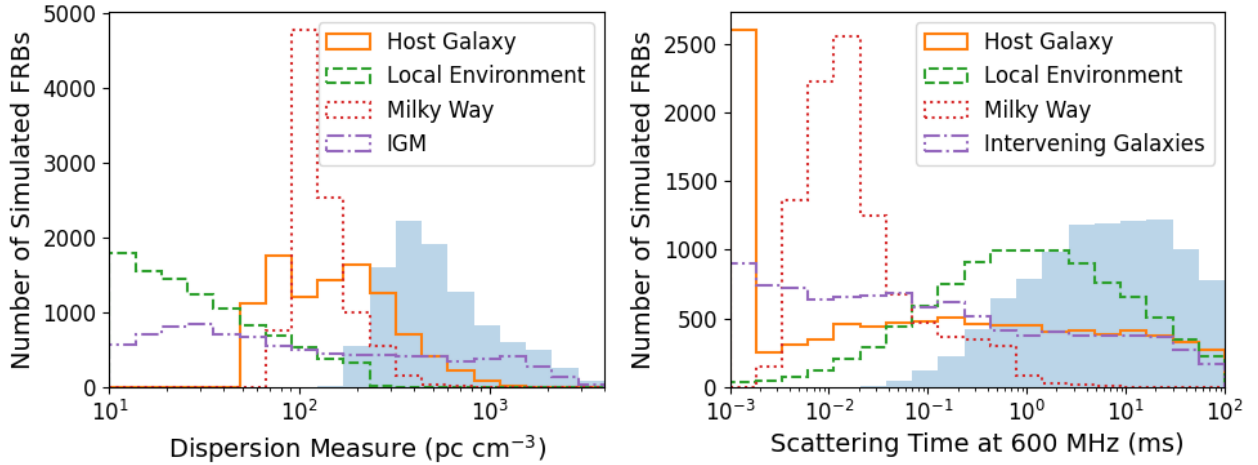


**Figure 5.8:** Simulated distributions of DMs and scattering times for the model found to be marginally consistent with Catalog 1 based on KS and AD tests. Histograms for the total DM and scattering time of the simulated FRBs are shown in blue. All other histograms show the DM and scattering contributions of different intervening media (see §5.4). For visualization purposes, scattering times  $< 10^{-3}$  ms are set to be equal to  $10^{-3}$  ms in the right panel. The contribution of the IGM is not shown in the right panel as we do not simulate scattering in the IGM (see §5.4.2). We remove FRBs with total scattering times  $> 100$  ms from the simulated distribution to allow for comparison with the selection-corrected scattering time distribution obtained for Catalog 1, which extends up to 100 ms.

which is the theoretical expectation for a Kolmogorov medium with a negligible inner scale.

While fitting the Catalog 1 bursts with a scattering timescale valid for a power-law index of  $-4.4$  is outside the scope of this paper, we note that a difference of 0.4 in the index will modify the scattering time by a maximum of  $(\nu_1/\nu_2)^{-0.4} \sim 30\%$ . Here  $\nu_1$  and  $\nu_2$  are the lowest and highest observing frequencies, respectively. Since the PDF for the scattering time distribution in the catalog is evaluated for logarithmic bins, measured scattering times for an index of  $-4.4$  would lie in the same or adjacent bin. The results of the comparison between the simulated distributions and Catalog 1 would thus not change significantly if a power-law index of  $-4.4$  is assumed.

### 5.6.2 Circumburst Environment

We find that none of the population models in which scattering originates only in the ISM of the Milky Way and the host galaxy can reproduce the observed scattering time distribution (see Table 5.1). These models fail to match the large population of events with scattering times  $> 10$  ms, as shown in Figure 5.9. This result confirms the conclusions of a population synthesis analysis conducted for the first 13 CHIME-detected bursts, which suggested that FRBs must have local environments with stronger scattering properties than the Milky Way ISM (CHIME/FRB Collaboration et al., 2019b). Additionally, this result is also consistent with the observation of two FRBs located in the outskirts of their host galaxies showing significant scattering (Day et al., 2020).

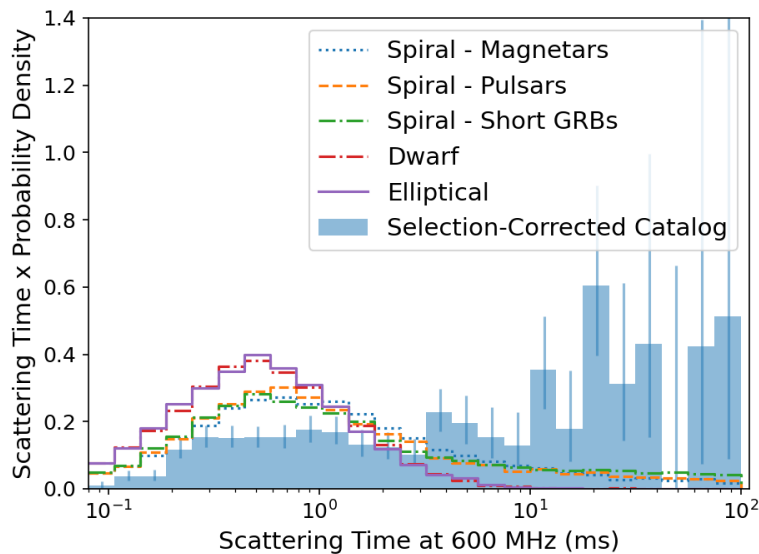


**Figure 5.9:** Scattering time distribution for population models in which the ISM of the host galaxy and the Milky Way are the dominant sources of scattering. The models assume FRBs to be located in different types of host galaxies. For spiral galaxies, three spatial distributions within the host are simulated, which emulate the magnetar, pulsar and short GRB populations. These models do not include DM or scattering contribution from the circumburst environment. The histograms represent the probability density function reparameterized in terms of the natural logarithm of the scattering timescale. The scattering time distribution for the catalog is shown in blue. The catalog data are corrected for selection effects with the error bars showing the 68% Poissonian confidence interval for each bin value. The simulation histograms show the average PDF over 100 Monte Carlo realizations of each model.

We also test models in which FRBs inhabit dense local environments, the DMs and scattering times for which are simulated based on empirically derived values for the lines of sight of  $\sim 100$  Galactic pulsars. The additional scattering contributed by these environments reduces the discrepancy between the simulated and observed population as is indicated by higher p-values for the KS test (see columns for which  $DM_{\text{Local}} > 0.1 \text{ pc cm}^{-3}$  in Table 5.1). We also allow for circumburst environments with more extreme properties by introducing a higher threshold for the local DM contribution,  $DM_{\text{Local}} > 10 \text{ pc cm}^{-3}$ . Although these models, on average, have higher scattering times and higher p-values for the KS test, they are still unable to explain the highly scattered bursts in the observed population, as shown in Figure 5.10.

While further increasing the local DM threshold increases the total scattering timescales, it causes the overall DM distribution to be inconsistent with the catalog, as shown in Figure 5.10 for a model in which  $DM_{\text{Local}} > 50 \text{ pc cm}^{-3}$ . Our results therefore suggest that the circumburst media must contribute more scattering per unit DM than typical Galactic plane environments such as HII regions or star-formation complexes. This agrees with the results of a population study of scattering in Parkes FRBs which concluded that FRBs must inhabit a denser and more turbulent environment than a SGR 1935+2154-like magnetar (Hackstein et al., 2020). One caveat, however, is that scattering could be contributed by sources other than the local environment and the ISM of the Milky Way and the host galaxy. We discuss the CGM of intervening galaxies as one such source in §5.6.3.

### 5.6.3 Intervening Galaxies

Introducing the CGM of intervening galaxies as an additional source of scattering reduces the discrepancy between the observed and simulated distributions. This is illustrated in Table 5.1, where population models with no scattering arising in intervening galaxies show higher deviation from the observed distribution as compared to models in which this source of scattering is included. Among the population models we test, the only one we cannot

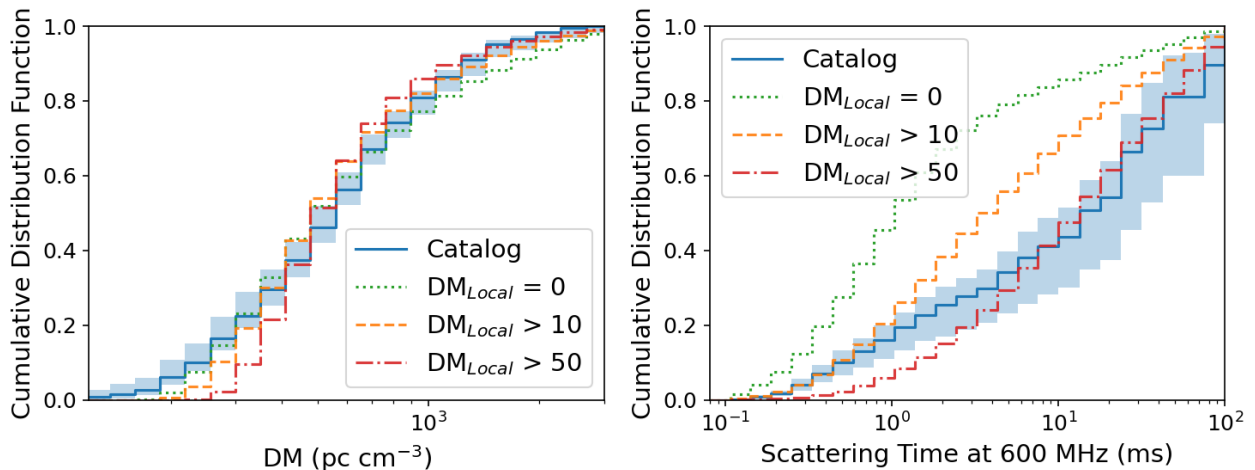


**Figure 5.10:** Cumulative distribution function for simulated DMs and scattering times for a short GRB-like spatial distribution of FRBs in spiral galaxies. Simulated distributions for three population models are shown here with the models differing in the contribution of the local environment to burst DMs and scattering times. The DMs of the local environment are drawn from a lognormal distribution (see §5.4.4) with a minimum threshold as indicated in the legend. Increasing the local DM threshold results in higher scattering times, which reduces the discrepancy between the simulated and observed scattering time distribution but exacerbates the differences between the corresponding DM distributions at the low-DM end. The CDF for the simulated distributions are averaged over 100 Monte Carlo realizations for each model. The selection-corrected DM and scattering distributions in the catalog are plotted in blue. Uncertainties on the catalog CDF are determined in the same manner as for Figure 5.7.

rule out has scattering originating both in the circumburst environment and in intervening galaxies. This model is statistically preferred over one with scattering originating only in the circumburst environment, as the sub-parsec scale clumps in the CGM of intervening galaxies (Vedantham & Phinney, 2019) contribute more scattering per unit DM as compared to the simulated circumburst environments.

However, it could be that the CGM of intervening galaxies is not as turbulent as assumed in the model put forth by Vedantham & Phinney (2019). Ocker et al. (2021) place an upper limit on the fluctuation parameter, which is proportional to  $(\tau/\text{DM}^2)$ , for the CGM of the Milky Way using scattering measurements of two FRBs. The fluctuation parameter that they infer is orders of magnitude lower than that proposed for the CGM by Vedantham & Phinney (2019), suggesting that halos of other galaxies might not significantly contribute to FRB

scattering. Recent observations of two FRBs whose sightlines intercept halos of other galaxies also support this claim (Cho et al., 2020; Simha et al., 2020). The aforementioned studies prompt us to reconsider the conclusions of §5.6.2. If the proposed model of CGM scattering is correct, then the halos of intervening galaxies along with typical galactic plane environments can explain the scattering properties of CHIME/FRB detected sources. However, if the CGM of intervening galaxies is not as turbulent as is suggested by Vedantham & Phinney (2019), then more extreme circumburst environments are required.

#### 5.6.4 Host Galaxies

We initially tested population models in which all FRBs are located in host galaxies of the same type, in order to reduce the computational cost of the simulations. For this simplistic scenario, the only model that we cannot formally exclude given the data assumes that all FRBs are located in spiral galaxies. However, observed host galaxies for localized FRBs seem to be drawn from a more heterogeneous sample. While the first repeating FRB was localized to a dwarf galaxy (Tendulkar et al., 2017), since then several spiral and elliptical hosts have been identified with varying rates of star formation (Bhandari et al., 2020). More recently, Heintz et al. (2020) studied the properties of the localized FRB sample and rejected the hypothesis that the population originates exclusively in late-type galaxies with  $> 3\sigma$  confidence.

To test whether the observed scenario of a heterogeneous sample of host galaxies is consistent with the DM and scattering distributions in the catalog, we rerun our simulations for the model that initially reproduced our observations. However, for this iteration, we place half of the FRB population in spiral galaxies and half in elliptical galaxies. We keep all other parameters constant as we simulate a short GRB-like population evolving with the star-formation rate with scattering arising in the local environment and in intervening galaxies. We find that the population distributed like short GRBs with a mixed distribution of FRB host galaxies is also marginally consistent with the catalog, with the constraints on

scattering being the same as those in §5.6.3. The mean p-value for the KS test comparing 100 realizations of the scattering time distribution for this model with the catalog is  $10^{-4}$ , implying that the model is as likely as the one in which all FRBs have spiral hosts. As the scattering in both the models is mainly contributed by the circumburst environment and the CGM of intervening galaxies, the significance level does not change even after reducing the scattering contribution of the host ISM for half of the simulated FRBs.

Another property of FRB host galaxies that has been constrained by recent population studies is their DM contribution. The constraints range from 50 to 270  $\text{pc cm}^{-3}$  (see, e.g., [Gardenier & van Leeuwen 2021](#); [Yang et al. 2017](#)) and include the contribution of the host galaxy and the circumburst environment. For simulated models consistent with Catalog 1, we find that the median rest-frame host DM ranges from 150 to 200  $\text{pc cm}^{-3}$ . Our findings are consistent with a recent study by [James et al. \(2021\)](#) of a sample of FRBs detected with the Parkes (Murriyang) and ASKAP telescopes. The sample also includes seven FRBs with confirmed host galaxies, based on which they infer an average rest-frame host DM of  $145_{-65}^{+60}$   $\text{pc cm}^{-3}$ .

More recently, an angular cross-correlation analysis of CHIME/FRB sources with cosmological galaxy catalogues has provided evidence for a sub-population of FRBs at  $z \sim 0.4$  with host DMs of  $\sim 400$   $\text{pc cm}^{-3}$  ([Rafei-Ravandi et al., 2021](#)). The aforementioned host DM is estimated in the observer’s frame and translates to a rest-frame DM of  $\sim 560$   $\text{pc cm}^{-3}$ . However, [Rafei-Ravandi et al. \(2021\)](#) clarify that their results do not suggest that majority of FRBs have host DMs greater than this value, implying that the median host DM for our simulations could be consistent with their findings.

[Rafei-Ravandi et al. \(2021\)](#) suggest that the high host DMs for this sub-population of FRBs could be explained if they are located near the centres of large ( $10^{14} M_{\odot}$ ) halos. Although we simulate the DM contribution of the host halo in our analysis, we assume it to be similar to the Milky Way (ranging from 30 to 80  $\text{pc cm}^{-3}$ ). We do not consider the scattering contribution of the host halo as it is expected to be  $< 1$  ms for a Milky Way-like

galaxy (see §5.4.1). Scattering timescales could be larger for halos which are more massive than that of the Milky Way, which has a mass of  $\sim 10^{12}M_{\odot}$  (Posti & Helmi, 2019). We do not simulate a sub-population of FRBs located near these large halos due to the uncertain scattering time contribution but note that it could reduce the discrepancy between the simulated and observed scattering time distributions.

### 5.6.5 Progenitor Models

Our simulations favour a population of FRBs offset from their galaxy centres, modelled based on the observed offsets for the short GRB population. Other progenitor models with offsets similar to those observed for short GRBs could also be consistent with our observations. This result is consistent with observations of FRBs that have been localized with sub-arcsecond precision. Mannings et al. (2021) study the offset distribution for eight such FRBs and find that it is consistent both with a population of core-collapse supernovae and short GRBs (see Figure 4 of their paper).

If the circumburst environment and intervening galaxies contribute significantly to scattering, the simulated scattering times for all tested spatial distributions are consistent with the catalog, as shown in Figure 5.11. However, spatial distributions resembling those of the pulsar and magnetar populations in the Milky Way can be ruled out due to a lack of low-DM FRBs (see Figure 5.11). The simulated DMs for a population modelled based on pulsars or magnetars are consistent with the catalog only if the contributions of the host galaxy, the Milky Way and the IGM are considered. The distributions become inconsistent if the DM contribution of dense circumburst environments is included, as shown in Figure 5.11. Since a population of FRBs offset from their galaxy centres has lower host DMs, on average, than a population distributed along the spiral arms, the simulated DM distribution for a short GRB-like population is statistically consistent with the catalog even with the inclusion of dense circumburst environments.

It is important to note that we cannot rule out pulsars or magnetars as FRB progenitors

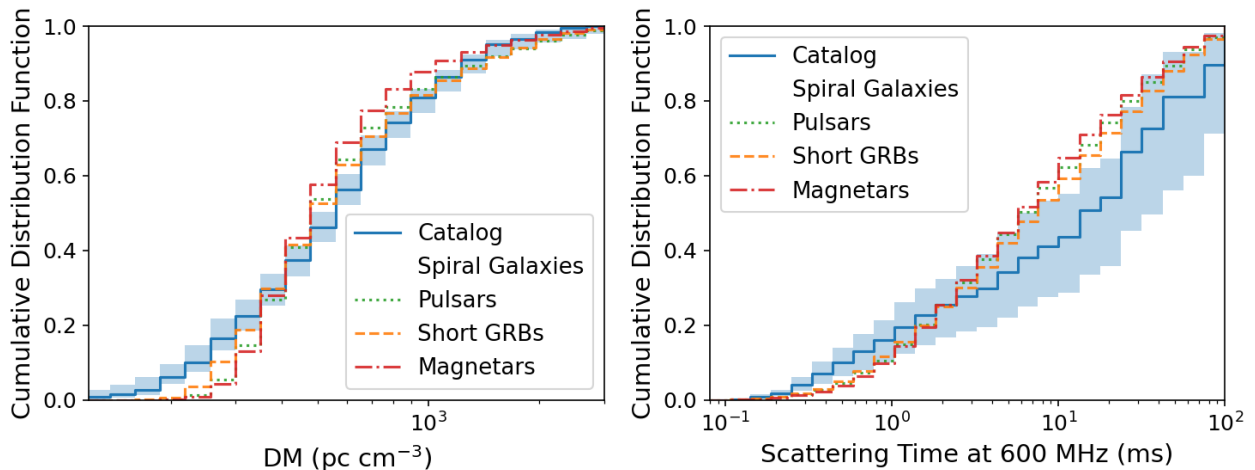


**Figure 5.11:** Cumulative distribution function of simulated DMs and scattering times for different potential FRB progenitors assumed to be located in spiral galaxies. Simulated population models assume that significant scattering is originating in the local environment with the local DM being drawn from a lognormal distribution (see §5.4.4) having a minimum threshold of  $10 \text{ pc cm}^{-3}$ . Scattering is also assumed to be contributed by intervening galaxies with  $f_{\text{CGM}} = 0.6$ . The CDF for the simulated distributions are averaged over 100 Monte Carlo realizations for each model. The selection-corrected DM and scattering distributions in the catalog are plotted in blue. Uncertainties on the catalog CDF are determined in the same manner as for Figure 5.7. While simulated scattering time distributions for some realizations of the pulsar and magnetar models are consistent with the corresponding catalog distribution, the simulated DM distributions for those realizations are found to be inconsistent with the catalog on the basis of a KS test.

if FRBs originate in environments with stronger scattering properties (such as a very young supernova remnant) than those simulated in our analysis. This is because higher scattering per unit DM in the local environment can potentially increase the number of low DM FRBs with high scattering times and reduce the discrepancy between the simulated and observed distributions in Figure 5.11. Although we test different spatial distributions in spiral galaxies, any spatial distribution of FRBs located in a mixed distribution of host galaxies could explain our observations, provided the FRBs inhabit circumburst environments with strong scattering properties. In this scenario, the elliptical and dwarf hosts might be able to explain the observed low DMs while the circumburst environments can reproduce the high scattering timescales.

## 5.7 Summary and Conclusions

We have performed a population synthesis study to interpret the joint distribution of dispersion measures and scattering timescales for the first CHIME/FRB catalog. The study involved simulating FRB populations, specifically, their intrinsic properties and propagation effects arising in the Milky Way, the IGM, the host galaxy and the circumburst environment. The simulated FRB populations were based on different models varying in their redshift distribution, host galaxy types and spatial distribution within the host.

We compared the DM and scattering time distributions for the simulated FRB populations with the corresponding selection-corrected distributions for the catalog using KS and AD tests. For all population models that we simulate, we find that we cannot reproduce the observed scattering times if FRBs have circumburst environments with properties similar to those inferred for the local environments of Galactic pulsars. Based on this result, we infer that the circumburst media of FRBs must have more extreme properties than those of typical Galactic plane environments, thereby improving on the constraints that were derived based on the scattering times of the first 13 CHIME-detected FRBs ([CHIME/FRB Collaboration et al., 2019b](#)).

We also test the possibility that sub-parsec scale cool ionized gas clumps in the circumgalactic medium of intervening galaxies could be contributing to FRB scattering ([Vedantham & Phinney, 2019](#)). We find that we cannot rule out a model of FRBs for which scattering originates in both in the local environment and in intervening galaxies. If the proposed models for CGM scattering are correct, then this additional source of scattering relaxes the requirement of local environments of FRBs having more extreme properties than the ensemble of Galactic plane environments that we model.

While we cannot as yet determine the dominant host galaxy type using the observed DM and scattering distributions, we place some constraints on FRB progenitor models. Our simulations favour a population of FRBs offset from their galaxy centres – like the short GRB population – over a population which is distributed along the spiral arms such as the

magnetar and pulsar populations in the Milky Way. However, this result is dependent on the assumption that circumburst environments resemble those of Galactic pulsars.

Another major caveat is that we simulate FRBs in different host galaxies, the electron density distributions of which are poorly understood. The assumed electron density models might not be able to adequately characterize the dispersive and scattering properties of these galaxies. Population studies of this kind therefore need to be augmented by analysis of scattering budgets of localized FRBs (see, e.g., [Simha et al. 2020](#); [Ocker et al. 2021](#)). We encourage more such studies as the scattering time measurement for localized sources can be interpreted using additional information about the host galaxy, intervening galaxies and the local environment available from multi-wavelength follow-up observations. Such studies could then provide priors on the level of turbulence in other galaxies which in turn can enhance the robustness of population synthesis studies.

It is also important to note that the aforementioned conclusions are derived for the full FRB population as the selection-corrected distributions for the CHIME/FRB catalog include both repeating and so-far non-repeating sources ([CHIME/FRB Collaboration et al., 2021a](#)). The CHIME/FRB system is expected to detect more repeating FRB sources in the coming years which can allow for determination of the selection-corrected distributions exclusively for the repeating FRB population. Analyses similar to the one we report on here can then help discern whether repeating FRBs constitute a different population as compared to non-repeating sources based on their observed scattering properties.

## Chapter 6

### Conclusions

This thesis comprises of several independent analyses, all aimed at characterizing the properties of the FRB population. We summarize the key conclusions of each of these analyses in this chapter. In the time since these analyses were performed, several new results have been obtained from observations with the CHIME/FRB system and other FRB detection instruments. We discuss our conclusions in the context of these results and also present potential directions for future research.

In Chapter 3, we have presented techniques developed to determine the exposure of the CHIME/FRB system. Using these techniques, we generated full-sky exposure maps for the observing duration of the first CHIME/FRB catalog. We used these maps to determine the exposure for all sources included in the catalog. A novel method to determine the variation in the RMS radiometer noise using single pulses from Galactic pulsars is also presented in this chapter. Using this technique, we were able to characterize the daily sensitivity variations for the CHIME/FRB system and exclude days with high RMS noise (and low sensitivity) from the exposure.

The exposure maps are made available to the broader FRB research community as part of the Catalog 1 data release. We envision the use of these maps to determine the CHIME/FRB exposure for FRBs discovered with other instruments and transients detected at other wavelengths. The maps can also be queried to determine the exposure to

particular galaxies or sky regions. As an example, we determined the exposure to 15 nearby star-forming galaxies in order to constrain the rate of FRB-like bursts emitted by the magnetars located in these galaxies (CHIME/FRB Collaboration et al., 2020a).

We plan to make several improvements to the exposure and sensitivity estimation process for future CHIME/FRB catalogs. Firstly, the metrics for different stages of the detection pipeline will be recorded at a cadence of 4 s. The cadence currently ranges from a few minutes to hours, depending on the pipeline stage. Secondly, the number of available frequency channels will be taken into consideration while estimating the exposure. The number of available frequency channels varies on the timescale of a few minutes due to the dynamic nature of the RFI masking process at the L1 stage and the varying up-time of the L0 nodes, each of which process data for 0.4% of the total bandwidth. Thirdly, once the synthetic signal injection system is operational throughout the observations, it will be used to determine the daily sensitivity variations in conjunction with the method reported on in this thesis. Lastly, exposure maps will be made available for a few different frequencies, in addition to the reference frequency of 600 MHz that we adopt in this thesis.

In Chapter 4, we have presented observations of the periodically active FRB source, FRB 20180916B, conducted with the CHIME/FRB system, GBT and LOFAR telescopes. The source was first discussed in Chapter 3, where we used the exposure information to rule out an instrumental origin for its periodicity. We also characterized the variation in the burst rate during the 5-day long active phases of the source and concluded that the source activity is maximum in a  $\pm 0.9$ -day interval around the epochs of peak activity. The observing strategy for the follow-up observations with GBT and LOFAR was informed by these rate estimates.

Seven bursts were detected during the GBT observations in the frequency range of 300–400 MHz, with no detections in the LOFAR band (110–190 MHz). The bursts had detectable emission at the bottom of the GBT band, implying that the cutoff frequency for FRB emission is less than 300 MHz. Knowing that the local environment is optically thin to free-free absorption at 300 MHz, we ruled out the possibility that the source is associated with

a hyper compact HII region or a young supernova remnant. The low observed scattering timescale ( $< 1.7$  ms at 350 MHz) supports this conclusion.

The recent detection of FRB 20180916B with the LOFAR telescope has shown that FRB emission extends down to 110 MHz (Pastor-Marazuela et al., 2020; Pleunis et al., 2021). Moreover, Pastor-Marazuela et al. (2020) find that the repetition rate for this source at 150 MHz is greater than the rate at 1.4 GHz. This result confirms our observation of a decrease in burst activity with increasing frequency, obtained by comparing the repetition rates in the GBT and CHIME bands. It is important to perform multi-band observations of more FRB sources to study the frequency dependence of burst activity. As demonstrated by our analysis, the detection of a spectral turnover (or lack thereof) for these FRB sources can help determine the properties of their local environments and constrain progenitor models.

To determine if a significant fraction of FRBs exhibit a spectral turnover, one can also compare the all-sky rate at different frequencies. Shortly after the GBT detection of FRB 20180916B was published, the detection of an FRB in an all-sky survey at 350 MHz was reported by Parent et al. (2020). The all-sky rate estimated based on this detection is  $3.4_{-3.3}^{+15.4} \times 10^3$  FRBs sky $^{-1}$  day $^{-1}$  above a peak flux density of 0.4 Jy. The large uncertainties on this measurement prohibit a robust comparison with the reported rates at gigahertz frequencies. More detections in blind searches at low frequencies are required to reduce the rate measurement uncertainties and constrain the ensemble spectrum of the FRB population.

In Chapter 5, we have presented a population synthesis study in which we simulate the DM and scattering contribution of different intervening media to test whether they can reproduce the corresponding distributions in the first CHIME/FRB catalog. We find that the population models in which scattering is contributed only by the ISM of the host galaxy and the Milky Way cannot reproduce the scattering properties in the catalog. Motivated by this result, we considered circumburst environments and the CGM of intervening galaxies as additional sources of scattering. Upon including the contribution of these sources, the simulated scattering distribution becomes marginally consistent with the catalog. However,

if the CGM of intervening galaxies is not as turbulent as we assume in our simulations, then we conclude that FRBs must inhabit environments with more extreme scattering properties than typical Galactic plane environments.

To confirm if the circumburst environments have extreme properties, localizations of the order of 100 milli-arcseconds are required as they can determine where an FRB is located within its host galaxy (see, e.g., [Chatterjee et al. 2017](#); [Marcote et al. 2017](#)). On the other hand, localizations of lower precision can be used to confirm whether the CGM of intervening galaxies is a source of intense scattering. A recent study by [Connor & Ravi \(2021\)](#) identified the CHIME-detected FRBs which likely intersect halos of nearby galaxies ( $< 40$  Mpc). They found that this sample had, on average, greater extragalactic DMs than the rest of the catalog sources and suggested that the excess can be explained if galaxy halos contribute significantly to FRB DMs. Similar studies can be performed to constrain the scattering contribution of intervening galaxies.

A sample of localized FRBs can also be used to constrain the DM and scattering contributions of different types of galaxies. Once the host galaxy type is identified and the location of an FRB within the galaxy is known, analysis of the DM and scattering budget of the FRB can provide information about how the free electrons are distributed within the host. It is crucial to perform this analysis, especially for FRBs located in dwarf and elliptical galaxies as the electron density distributions for these galaxies are poorly understood.

The studies proposed above require a much larger sample of localized FRBs than is currently available. The number of localized FRBs is expected to greatly increase once the CHIME/FRB outrigger telescopes come online. These telescopes are currently being built and will provide localization (with a precision of  $\sim 50$  milli-arcseconds) and host galaxy identification for a significant fraction of the FRBs that are detected with CHIME. In the meantime, the CHIME/FRB system is detecting more FRBs and a second FRB catalog is currently in preparation. The larger sample of FRBs can be used to perform population

synthesis studies, similar to the one presented in this thesis, for scattering and other burst properties.

## Bibliography

- Andersen, B. C., & Ransom, S. M. 2018, *The Astrophysical Journal Letters*, 863, L13, doi: [10.3847/2041-8213/aad59f](https://doi.org/10.3847/2041-8213/aad59f)
- Arzoumanian, Z., Baker, P. T., Blumer, H., et al. 2020, *The Astrophysical Journal Letters*, 905, L34, doi: [10.3847/2041-8213/abd401](https://doi.org/10.3847/2041-8213/abd401)
- Backer, D. C. 1970, *Nature*, 228, 42, doi: [10.1038/228042a0](https://doi.org/10.1038/228042a0)
- Bandura, K., Cliche, J. F., Dobbs, M. A., et al. 2016a, *Journal of Astronomical Instrumentation*, 5, 1641004, doi: [10.1142/S225117171641004X](https://doi.org/10.1142/S225117171641004X)
- Bandura, K., Addison, G. E., Amiri, M., et al. 2014, in *Society of Photo-Optical Instrumentation Engineers (SPIE) Conference Series*, Vol. 9145, *Ground-based and Airborne Telescopes V*, ed. L. M. Stepp, R. Gilmozzi, & H. J. Hall, 914522, doi: [10.1117/12.2054950](https://doi.org/10.1117/12.2054950)
- Bandura, K., Bender, A. N., Cliche, J. F., et al. 2016b, *Journal of Astronomical Instrumentation*, 5, 1641005, doi: [10.1142/S2251171716410051](https://doi.org/10.1142/S2251171716410051)
- Bassa, C. G., Pleunis, Z., & Hessels, J. W. T. 2017, *Astronomy and Computing*, 18, 40, doi: [10.1016/j.ascom.2017.01.004](https://doi.org/10.1016/j.ascom.2017.01.004)
- Beloborodov, A. M. 2017, *The Astrophysical Journal Letters*, 843, L26, doi: [10.3847/2041-8213/aa78f3](https://doi.org/10.3847/2041-8213/aa78f3)

- Beniamini, P., Wadiasingh, Z., & Metzger, B. D. 2020, *Monthly Notices of the Royal Astronomical Society*, 496, 3390, doi: [10.1093/mnras/staa1783](https://doi.org/10.1093/mnras/staa1783)
- Bhandari, S., Keane, E. F., Barr, E. D., et al. 2018, *Monthly Notices of the Royal Astronomical Society*, 475, 1427, doi: [10.1093/mnras/stx3074](https://doi.org/10.1093/mnras/stx3074)
- Bhandari, S., Sadler, E. M., Prochaska, J. X., et al. 2020, *The Astrophysical Journal Letters*, 895, L37, doi: [10.3847/2041-8213/ab672e](https://doi.org/10.3847/2041-8213/ab672e)
- Bhardwaj, M., Gaensler, B. M., Kaspi, V. M., et al. 2021, *The Astrophysical Journal Letters*, 910, L18, doi: [10.3847/2041-8213/abeaa6](https://doi.org/10.3847/2041-8213/abeaa6)
- Bhat, N. D. R., Cordes, J. M., Camilo, F., Nice, D. J., & Lorimer, D. R. 2004, *The Astrophysical Journal*, 605, 759, doi: [10.1086/382680](https://doi.org/10.1086/382680)
- Blandford, R., & Narayan, R. 1985, *Monthly Notices of the Royal Astronomical Society*, 213, 591, doi: [10.1093/mnras/213.3.591](https://doi.org/10.1093/mnras/213.3.591)
- Bochenek, C. D., Ravi, V., Belov, K. V., et al. 2020, *Nature*, 587, 59, doi: [10.1038/s41586-020-2872-x](https://doi.org/10.1038/s41586-020-2872-x)
- Brandenberger, R., Cyr, B., & Varna Iyer, A. 2017, arXiv e-prints, arXiv:1707.02397. <https://arxiv.org/abs/1707.02397>
- Brentjens, M. A., & de Bruyn, A. G. 2005, *Astronomy & Astrophysics*, 441, 1217, doi: [10.1051/0004-6361:20052990](https://doi.org/10.1051/0004-6361:20052990)
- Burke-Spolaor, S., & Bannister, K. W. 2014, *The Astrophysical Journal*, 792, 19, doi: [10.1088/0004-637X/792/1/19](https://doi.org/10.1088/0004-637X/792/1/19)
- Burke-Spolaor, S., Johnston, S., Bailes, M., et al. 2012, *Monthly Notices of the Royal Astronomical Society*, 423, 1351, doi: [10.1111/j.1365-2966.2012.20998.x](https://doi.org/10.1111/j.1365-2966.2012.20998.x)

- Burn, B. J. 1966, *Monthly Notices of the Royal Astronomical Society*, 133, 67, doi: [10.1093/mnras/133.1.67](https://doi.org/10.1093/mnras/133.1.67)
- Caleb, M., Flynn, C., Bailes, M., et al. 2016, *Monthly Notices of the Royal Astronomical Society*, 458, 718, doi: [10.1093/mnras/stw109](https://doi.org/10.1093/mnras/stw109)
- Chatterjee, S., Law, C. J., Wharton, R. S., et al. 2017, *Nature*, 541, 58, doi: [10.1038/nature20797](https://doi.org/10.1038/nature20797)
- Chawla, P., Kaspi, V. M., Josephy, A., et al. 2017, *The Astrophysical Journal*, 844, 140, doi: [10.3847/1538-4357/aa7d57](https://doi.org/10.3847/1538-4357/aa7d57)
- CHIME/FRB Collaboration, Amiri, M., Bandura, K., et al. 2018, *The Astrophysical Journal*, 863, 48, doi: [10.3847/1538-4357/aad188](https://doi.org/10.3847/1538-4357/aad188)
- CHIME/FRB Collaboration, Andersen, B. C., Bandura, K., et al. 2019a, *The Astrophysical Journal Letters*, 885, L24, doi: [10.3847/2041-8213/ab4a80](https://doi.org/10.3847/2041-8213/ab4a80)
- CHIME/FRB Collaboration, Amiri, M., Bandura, K., et al. 2019b, *Nature*, 566, 230, doi: [10.1038/s41586-018-0867-7](https://doi.org/10.1038/s41586-018-0867-7)
- . 2019c, *Nature*, 566, 235, doi: [10.1038/s41586-018-0864-x](https://doi.org/10.1038/s41586-018-0864-x)
- CHIME/FRB Collaboration, Amiri, M., Andersen, B. C., et al. 2020a, *Nature*, 582, 351, doi: [10.1038/s41586-020-2398-2](https://doi.org/10.1038/s41586-020-2398-2)
- CHIME/FRB Collaboration, Andersen, B. C., Bandura, K. M., et al. 2020b, *Nature*, 587, 54, doi: [10.1038/s41586-020-2863-y](https://doi.org/10.1038/s41586-020-2863-y)
- CHIME/FRB Collaboration, :, Amiri, M., et al. 2021a, arXiv e-prints, arXiv:2106.04352. <https://arxiv.org/abs/2106.04352>
- CHIME/FRB Collaboration, Andersen, B. C., Bandura, K., et al. 2021b, arXiv e-prints, arXiv:2107.08463. <https://arxiv.org/abs/2107.08463>

- CHIME/Pulsar Collaboration, Amiri, M., Bandura, K. M., et al. 2021, *The Astrophysical Journal Supplement Series*, 255, 5, doi: [10.3847/1538-4365/abfdcb](https://doi.org/10.3847/1538-4365/abfdcb)
- Chittidi, J. S., Simha, S., Mannings, A., et al. 2020, arXiv e-prints, arXiv:2005.13158. <https://arxiv.org/abs/2005.13158>
- Cho, H., Macquart, J.-P., Shannon, R. M., et al. 2020, *The Astrophysical Journal Letters*, 891, L38, doi: [10.3847/2041-8213/ab7824](https://doi.org/10.3847/2041-8213/ab7824)
- Churchwell, E. 2002, *Annual Review of Astronomy and Astrophysics*, 40, 27
- Coenen, T., van Leeuwen, J., Hessels, J. W. T., et al. 2014, *A&A*, 570, A60, doi: [10.1051/0004-6361/201424495](https://doi.org/10.1051/0004-6361/201424495)
- Condon, J. J., & Ransom, S. M. 2016, *Essential radio astronomy* (Princeton University Press)
- Connor, L., & Ravi, V. 2021, arXiv e-prints, arXiv:2107.13692. <https://arxiv.org/abs/2107.13692>
- Connor, L., Sievers, J., & Pen, U.-L. 2016, *Monthly Notices of the Royal Astronomical Society*, 458, L19, doi: [10.1093/mnrasl/slv124](https://doi.org/10.1093/mnrasl/slv124)
- Cordes, J. M., & Chatterjee, S. 2019, *Annual Review of Astronomy and Astrophysics*, 57, 417, doi: [10.1146/annurev-astro-091918-104501](https://doi.org/10.1146/annurev-astro-091918-104501)
- Cordes, J. M., & Lazio, T. J. W. 2002, arXiv e-prints, astro. <https://arxiv.org/abs/astro-ph/0207156>
- . 2003, arXiv e-prints, astro. <https://arxiv.org/abs/astro-ph/0301598>
- Cordes, J. M., & McLaughlin, M. A. 2003, *The Astrophysical Journal*, 596, 1142, doi: [10.1086/378231](https://doi.org/10.1086/378231)

- Cordes, J. M., & Wasserman, I. 2016, *Monthly Notices of the Royal Astronomical Society*, 457, 232, doi: [10.1093/mnras/stv2948](https://doi.org/10.1093/mnras/stv2948)
- Cordes, J. M., Wharton, R. S., Spitler, L. G., Chatterjee, S., & Wasserman, I. 2016, arXiv e-prints, arXiv:1605.05890. <https://arxiv.org/abs/1605.05890>
- Cruces, M., Spitler, L. G., Scholz, P., et al. 2021, *Monthly Notices of the Royal Astronomical Society*, 500, 448, doi: [10.1093/mnras/staa3223](https://doi.org/10.1093/mnras/staa3223)
- Cui, B. Y., Boyles, J., McLaughlin, M. A., & Palliyaguru, N. 2017, *The Astrophysical Journal*, 840, 5, doi: [10.3847/1538-4357/aa6aa9](https://doi.org/10.3847/1538-4357/aa6aa9)
- Curtin, A. 2021, Master's thesis, McGill University
- Dai, Z. G., Wang, J. S., Wu, X. F., & Huang, Y. F. 2016, *The Astrophysical Journal*, 829, 27, doi: [10.3847/0004-637X/829/1/27](https://doi.org/10.3847/0004-637X/829/1/27)
- Day, C. K., Deller, A. T., Shannon, R. M., et al. 2020, *Monthly Notices of the Royal Astronomical Society*, 497, 3335, doi: [10.1093/mnras/staa2138](https://doi.org/10.1093/mnras/staa2138)
- Demorest, P. B., Pennucci, T., Ransom, S. M., Roberts, M. S. E., & Hessels, J. W. T. 2010, *Nature*, 467, 1081, doi: [10.1038/nature09466](https://doi.org/10.1038/nature09466)
- Deneva, J. S., Stovall, K., McLaughlin, M. A., et al. 2016, *The Astrophysical Journal*, 821, 10, doi: [10.3847/0004-637X/821/1/10](https://doi.org/10.3847/0004-637X/821/1/10)
- Deng, M., & Campbell-Wilson, D. 2017, arXiv e-prints, arXiv:1708.08521. <https://arxiv.org/abs/1708.08521>
- Denman, N., Renard, A., Vanderlinde, K., et al. 2020, *Journal of Astronomical Instrumentation*, 9, 2050014, doi: [10.1142/S2251171720500142](https://doi.org/10.1142/S2251171720500142)
- Dolag, K., Gaensler, B. M., Beck, A. M., & Beck, M. C. 2015, *Monthly Notices of the Royal Astronomical Society*, 451, 4277, doi: [10.1093/mnras/stv1190](https://doi.org/10.1093/mnras/stv1190)

- Duncan, R. C., & Thompson, C. 1992, *The Astrophysical Journal Letters*, 392, L9, doi: [10.1086/186413](https://doi.org/10.1086/186413)
- DuPlain, R., Ransom, S., Demorest, P., et al. 2008, *Society of Photo-Optical Instrumentation Engineers (SPIE) Conference Series*, Vol. 7019, *Launching GUPPI: the Green Bank Ultimate Pulsar Processing Instrument*, 70191D, doi: [10.1117/12.790003](https://doi.org/10.1117/12.790003)
- Espinoza, C. M., Lyne, A. G., Stappers, B. W., & Kramer, M. 2011, *Monthly Notices of the Royal Astronomical Society*, 414, 1679, doi: [10.1111/j.1365-2966.2011.18503.x](https://doi.org/10.1111/j.1365-2966.2011.18503.x)
- Ester, M., Kriegel, H.-P., Sander, J., & Xu, X. 1996, in *Proceedings of the Second International Conference on Knowledge Discovery and Data Mining, KDD'96 (AAAI Press)*, 226–231
- Everett, J. E., & Weisberg, J. M. 2001, *The Astrophysical Journal*, 553, 341, doi: [10.1086/320652](https://doi.org/10.1086/320652)
- Farah, W., Flynn, C., Bailes, M., et al. 2018, *Monthly Notices of the Royal Astronomical Society*, 478, 1209, doi: [10.1093/mnras/sty1122](https://doi.org/10.1093/mnras/sty1122)
- Faucher-Giguère, C.-A., & Kaspi, V. M. 2006, *The Astrophysical Journal*, 643, 332, doi: [10.1086/501516](https://doi.org/10.1086/501516)
- Fong, W., & Berger, E. 2013, *The Astrophysical Journal*, 776, 18, doi: [10.1088/0004-637X/776/1/18](https://doi.org/10.1088/0004-637X/776/1/18)
- Fonseca, E., Andersen, B. C., Bhardwaj, M., et al. 2020, *The Astrophysical Journal Letters*, 891, L6, doi: [10.3847/2041-8213/ab7208](https://doi.org/10.3847/2041-8213/ab7208)
- Gajjar, V., Siemion, A. P. V., Price, D. C., et al. 2018, *The Astrophysical Journal*, 863, 2, doi: [10.3847/1538-4357/aad005](https://doi.org/10.3847/1538-4357/aad005)
- Gardenier, D. W., & van Leeuwen, J. 2021, *Astronomy & Astrophysics*, 651, A63, doi: [10.1051/0004-6361/202040119](https://doi.org/10.1051/0004-6361/202040119)

- Gardenier, D. W., van Leeuwen, J., Connor, L., & Petroff, E. 2019, *Astronomy & Astrophysics*, 632, A125, doi: [10.1051/0004-6361/201936404](https://doi.org/10.1051/0004-6361/201936404)
- Geng, J. J., & Huang, Y. F. 2015, *The Astrophysical Journal*, 809, 24, doi: [10.1088/0004-637X/809/1/24](https://doi.org/10.1088/0004-637X/809/1/24)
- Good, D. C., Andersen, B. C., Chawla, P., et al. 2020, arXiv e-prints, arXiv:2012.02320. <https://arxiv.org/abs/2012.02320>
- Górski, K. M., Hivon, E., Banday, A. J., et al. 2005, *The Astrophysical Journal*, 622, 759, doi: [10.1086/427976](https://doi.org/10.1086/427976)
- Gourdji, K., Michilli, D., Spitler, L. G., et al. 2019, *The Astrophysical Journal Letters*, 877, L19, doi: [10.3847/2041-8213/ab1f8a](https://doi.org/10.3847/2041-8213/ab1f8a)
- Gu, W.-M., Dong, Y.-Z., Liu, T., Ma, R., & Wang, J. 2016, *The Astrophysical Journal Letters*, 823, L28, doi: [10.3847/2041-8205/823/2/L28](https://doi.org/10.3847/2041-8205/823/2/L28)
- Hackstein, S., Brüggem, M., Vazza, F., & Rodrigues, L. F. S. 2020, *Monthly Notices of the Royal Astronomical Society*, 498, 4811, doi: [10.1093/mnras/staa2572](https://doi.org/10.1093/mnras/staa2572)
- Hankins, T. H., & Rickett, B. J. 1975, *Methods in Computational Physics*, 14, 55, doi: [10.1016/B978-0-12-460814-6.50007-3](https://doi.org/10.1016/B978-0-12-460814-6.50007-3)
- Haslam, C. G. T., Salter, C. J., Stoffel, H., & Wilson, W. E. 1982, *Astronomy and Astrophysics Supplement*, 47, 1
- Heald, G. 2009, in *IAU Symposium, Vol. 259, Cosmic Magnetic Fields: From Planets, to Stars and Galaxies*, ed. K. G. Strassmeier, A. G. Kosovichev, & J. E. Beckman, 591–602, doi: [10.1017/S1743921309031421](https://doi.org/10.1017/S1743921309031421)
- Heintz, K. E., Prochaska, J. X., Simha, S., et al. 2020, *The Astrophysical Journal*, 903, 152, doi: [10.3847/1538-4357/abb6fb](https://doi.org/10.3847/1538-4357/abb6fb)

- Hessels, J. W. T., Spitler, L. G., Seymour, A. D., et al. 2019, *The Astrophysical Journal Letters*, 876, L23, doi: [10.3847/2041-8213/ab13ae](https://doi.org/10.3847/2041-8213/ab13ae)
- Hewish, A., Bell, S. J., Pilkington, J. D. H., Scott, P. F., & Collins, R. A. 1968, *Nature*, 217, 709, doi: [10.1038/217709a0](https://doi.org/10.1038/217709a0)
- Hilmarsson, G. H., Michilli, D., Spitler, L. G., et al. 2021, *The Astrophysical Journal Letters*, 908, L10, doi: [10.3847/2041-8213/abdec0](https://doi.org/10.3847/2041-8213/abdec0)
- Hotan, A. W., van Straten, W., & Manchester, R. N. 2004, *Publications of the Astronomical Society of Australia*, 21, 302, doi: [10.1071/AS04022](https://doi.org/10.1071/AS04022)
- Houben, L. J. M., Spitler, L. G., ter Veen, S., et al. 2019, *Astronomy & Astrophysics*, 623, A42, doi: [10.1051/0004-6361/201833875](https://doi.org/10.1051/0004-6361/201833875)
- Inoue, S. 2004, *Monthly Notices of the Royal Astronomical Society*, 348, 999, doi: [10.1111/j.1365-2966.2004.07359.x](https://doi.org/10.1111/j.1365-2966.2004.07359.x)
- Ioka, K. 2003, *The Astrophysical Journal Letters*, 598, L79, doi: [10.1086/380598](https://doi.org/10.1086/380598)
- Ioka, K., & Zhang, B. 2020, *The Astrophysical Journal Letters*, 893, L26, doi: [10.3847/2041-8213/ab83fb](https://doi.org/10.3847/2041-8213/ab83fb)
- Isobe, T., Feigelson, E. D., Akritas, M. G., & Babu, G. J. 1990, *The Astrophysical Journal*, 364, 104, doi: [10.1086/169390](https://doi.org/10.1086/169390)
- Iwazaki, A. 2017, arXiv e-prints, arXiv:1707.04827. <https://arxiv.org/abs/1707.04827>
- James, C. W., Prochaska, J. X., Macquart, J. P., et al. 2021, arXiv e-prints, arXiv:2101.07998. <https://arxiv.org/abs/2101.07998>
- James, P. A., Shane, N. S., Beckman, J. E., et al. 2004, *Astronomy & Astrophysics*, 414, 23, doi: [10.1051/0004-6361:20031568](https://doi.org/10.1051/0004-6361:20031568)

- Josephy, A., Chawla, P., Fonseca, E., et al. 2019, *The Astrophysical Journal Letters*, 882, L18, doi: [10.3847/2041-8213/ab2c00](https://doi.org/10.3847/2041-8213/ab2c00)
- Josephy, A., Chawla, P., Curtin, A. P., et al. 2021, arXiv e-prints, arXiv:2106.04353. <https://arxiv.org/abs/2106.04353>
- Karastergiou, A., Chennamangalam, J., Armour, W., et al. 2015, *Monthly Notices of the Royal Astronomical Society*, 452, 1254, doi: [10.1093/mnras/stv1306](https://doi.org/10.1093/mnras/stv1306)
- Kashiyama, K., Ioka, K., & Mészáros, P. 2013, *The Astrophysical Journal Letters*, 776, L39, doi: [10.1088/2041-8205/776/2/L39](https://doi.org/10.1088/2041-8205/776/2/L39)
- Katz, J. I. 2016a, *The Astrophysical Journal*, 818, 19, doi: [10.3847/0004-637X/818/1/19](https://doi.org/10.3847/0004-637X/818/1/19)
- . 2016b, *The Astrophysical Journal*, 826, 226, doi: [10.3847/0004-637X/826/2/226](https://doi.org/10.3847/0004-637X/826/2/226)
- Keane, E. F., Stappers, B. W., Kramer, M., & Lyne, A. G. 2012, *Monthly Notices of the Royal Astronomical Society*, 425, L71, doi: [10.1111/j.1745-3933.2012.01306.x](https://doi.org/10.1111/j.1745-3933.2012.01306.x)
- Keating, L. C., & Pen, U.-L. 2020, *Monthly Notices of the Royal Astronomical Society*, 496, L106, doi: [10.1093/mnrasl/slaa095](https://doi.org/10.1093/mnrasl/slaa095)
- Kiel, P. D., Hurley, J. R., & Baines, M. 2010, *Monthly Notices of the Royal Astronomical Society*, 406, 656, doi: [10.1111/j.1365-2966.2010.16717.x](https://doi.org/10.1111/j.1365-2966.2010.16717.x)
- Kirsten, F., Marcote, B., Nimmo, K., et al. 2021, arXiv e-prints, arXiv:2105.11445. <https://arxiv.org/abs/2105.11445>
- Kondratiev, V. I., Verbiest, J. P. W., Hessels, J. W. T., et al. 2016, *Astronomy & Astrophysics*, 585, A128, doi: [10.1051/0004-6361/201527178](https://doi.org/10.1051/0004-6361/201527178)
- Kulkarni, S. R., Ofek, E. O., Neill, J. D., Zheng, Z., & Juric, M. 2014, *The Astrophysical Journal*, 797, 70, doi: [10.1088/0004-637X/797/1/70](https://doi.org/10.1088/0004-637X/797/1/70)

- Kumar, P., & Lu, W. 2020, *Monthly Notices of the Royal Astronomical Society*, 494, 1217, doi: [10.1093/mnras/staa801](https://doi.org/10.1093/mnras/staa801)
- Kumar, P., Shannon, R. M., Flynn, C., et al. 2021, *Monthly Notices of the Royal Astronomical Society*, 500, 2525, doi: [10.1093/mnras/staa3436](https://doi.org/10.1093/mnras/staa3436)
- Law, C. J., Abruzzo, M. W., Bassa, C. G., et al. 2017, *The Astrophysical Journal*, 850, 76, doi: [10.3847/1538-4357/aa9700](https://doi.org/10.3847/1538-4357/aa9700)
- Lawrence, E., Vander Wiel, S., Law, C., Burke Spolaor, S., & Bower, G. C. 2017, *The Astronomical Journal*, 154, 117, doi: [10.3847/1538-3881/aa844e](https://doi.org/10.3847/1538-3881/aa844e)
- Levin, Y., Beloborodov, A. M., & Bransgrove, A. 2020, *The Astrophysical Journal Letters*, 895, L30, doi: [10.3847/2041-8213/ab8c4c](https://doi.org/10.3847/2041-8213/ab8c4c)
- Lorimer, D. R., Bailes, M., McLaughlin, M. A., Narkevic, D. J., & Crawford, F. 2007, *Science*, 318, 777, doi: [10.1126/science.1147532](https://doi.org/10.1126/science.1147532)
- Lorimer, D. R., & Kramer, M. 2004, *Handbook of Pulsar Astronomy*, Vol. 4
- Lorimer, D. R., Faulkner, A. J., Lyne, A. G., et al. 2006, *Monthly Notices of the Royal Astronomical Society*, 372, 777, doi: [10.1111/j.1365-2966.2006.10887.x](https://doi.org/10.1111/j.1365-2966.2006.10887.x)
- Lyne, A. G., & Rickett, B. J. 1968, *Nature*, 219, 1339, doi: [10.1038/2191339a0](https://doi.org/10.1038/2191339a0)
- Lyubarsky, Y. 2014, *Monthly Notices of the Royal Astronomical Society*, 442, L9, doi: [10.1093/mnrasl/slu046](https://doi.org/10.1093/mnrasl/slu046)
- Lyutikov, M. 2013, *The Astrophysical Journal*, 768, 63, doi: [10.1088/0004-637X/768/1/63](https://doi.org/10.1088/0004-637X/768/1/63)
- Lyutikov, M., Barkov, M. V., & Giannios, D. 2020, *The Astrophysical Journal Letters*, 893, L39, doi: [10.3847/2041-8213/ab87a4](https://doi.org/10.3847/2041-8213/ab87a4)
- Lyutikov, M., Burzawa, L., & Popov, S. B. 2016, *Monthly Notices of the Royal Astronomical Society*, 462, 941, doi: [10.1093/mnras/stw1669](https://doi.org/10.1093/mnras/stw1669)

- Macquart, J. P., & Ekers, R. 2018, *Monthly Notices of the Royal Astronomical Society*, 480, 4211, doi: [10.1093/mnras/sty2083](https://doi.org/10.1093/mnras/sty2083)
- Macquart, J.-P., & Koay, J. Y. 2013, *The Astrophysical Journal*, 776, 125, doi: [10.1088/0004-637X/776/2/125](https://doi.org/10.1088/0004-637X/776/2/125)
- Macquart, J. P., Shannon, R. M., Bannister, K. W., et al. 2019, *The Astrophysical Journal Letters*, 872, L19, doi: [10.3847/2041-8213/ab03d6](https://doi.org/10.3847/2041-8213/ab03d6)
- Macquart, J. P., Keane, E., Grainge, K., et al. 2015, in *Advancing Astrophysics with the Square Kilometre Array (AASKA14)*, 55. <https://arxiv.org/abs/1501.07535>
- Macquart, J. P., Prochaska, J. X., McQuinn, M., et al. 2020, *Nature*, 581, 391, doi: [10.1038/s41586-020-2300-2](https://doi.org/10.1038/s41586-020-2300-2)
- Macquart, J. P. R., Hall, P., & Clarke, N. 2010, in *ISKAF2010 Science Meeting*, ed. J. van Leeuwen, 39
- Madau, P., & Dickinson, M. 2014, *Annual Review of Astronomy and Astrophysics*, 52, 415, doi: [10.1146/annurev-astro-081811-125615](https://doi.org/10.1146/annurev-astro-081811-125615)
- Manchester, R. N., Hobbs, G. B., Teoh, A., & Hobbs, M. 2005, *The Astronomical Journal*, 129, 1993, doi: [10.1086/428488](https://doi.org/10.1086/428488)
- Mannings, A. G., Fong, W.-f., Simha, S., et al. 2021, *The Astrophysical Journal*, 917, 75, doi: [10.3847/1538-4357/abff56](https://doi.org/10.3847/1538-4357/abff56)
- Marcote, B., Paragi, Z., Hessels, J. W. T., et al. 2017, *The Astrophysical Journal Letters*, 834, L8, doi: [10.3847/2041-8213/834/2/L8](https://doi.org/10.3847/2041-8213/834/2/L8)
- Marcote, B., Nimmo, K., Hessels, J. W. T., et al. 2020, *Nature*, 577, 190, doi: [10.1038/s41586-019-1866-z](https://doi.org/10.1038/s41586-019-1866-z)

- Margalit, B., Berger, E., & Metzger, B. D. 2019, *The Astrophysical Journal*, 886, 110, doi: [10.3847/1538-4357/ab4c31](https://doi.org/10.3847/1538-4357/ab4c31)
- Margalit, B., & Metzger, B. D. 2018, *The Astrophysical Journal Letters*, 868, L4, doi: [10.3847/2041-8213/aaedad](https://doi.org/10.3847/2041-8213/aaedad)
- Margalit, B., Metzger, B. D., & Sironi, L. 2020, *Monthly Notices of the Royal Astronomical Society*, 494, 4627, doi: [10.1093/mnras/staa1036](https://doi.org/10.1093/mnras/staa1036)
- Massey Jr., F. J. 1951, *Journal of the American Statistical Association*, 46, 68, doi: [10.1080/01621459.1951.10500769](https://doi.org/10.1080/01621459.1951.10500769)
- Masui, K., Lin, H.-H., Sievers, J., et al. 2015, *Nature*, 528, 523, doi: [10.1038/nature15769](https://doi.org/10.1038/nature15769)
- Masui, K. W., Shaw, J. R., Ng, C., et al. 2017, arXiv e-prints, arXiv:1710.08591. <https://arxiv.org/abs/1710.08591>
- Masui, K. W., & Sigurdson, K. 2015, *Physical Review Letters*, 115, 121301, doi: [10.1103/PhysRevLett.115.121301](https://doi.org/10.1103/PhysRevLett.115.121301)
- McCourt, M., Oh, S. P., O’Leary, R., & Madigan, A.-M. 2018, *Monthly Notices of the Royal Astronomical Society*, 473, 5407, doi: [10.1093/mnras/stx2687](https://doi.org/10.1093/mnras/stx2687)
- McKinnon, M. M. 2014, *Publications of the Astronomical Society of the Pacific*, 126, 476, doi: [10.1086/676975](https://doi.org/10.1086/676975)
- McLaughlin, M. A., Lyne, A. G., Lorimer, D. R., et al. 2006, *Nature*, 439, 817, doi: [10.1038/nature04440](https://doi.org/10.1038/nature04440)
- McQuinn, M. 2014, *The Astrophysical Journal Letters*, 780, L33, doi: [10.1088/2041-8205/780/2/L33](https://doi.org/10.1088/2041-8205/780/2/L33)
- Metzger, B. D., Berger, E., & Margalit, B. 2017, *The Astrophysical Journal*, 841, 14, doi: [10.3847/1538-4357/aa633d](https://doi.org/10.3847/1538-4357/aa633d)

- Metzger, B. D., Margalit, B., & Sironi, L. 2019, *Monthly Notices of the Royal Astronomical Society*, 485, 4091, doi: [10.1093/mnras/stz700](https://doi.org/10.1093/mnras/stz700)
- Mevius, M. 2018, RMextract: Ionospheric Faraday Rotation calculator. <http://ascl.net/1806.024>
- Michilli, D., Seymour, A., Hessels, J. W. T., et al. 2018, *Nature*, 553, 182, doi: [10.1038/nature25149](https://doi.org/10.1038/nature25149)
- Michilli, D., Masui, K. W., Mckinven, R., et al. 2021, *The Astrophysical Journal*, 910, 147, doi: [10.3847/1538-4357/abe626](https://doi.org/10.3847/1538-4357/abe626)
- Mingarelli, C. M. F., Levin, J., & Lazio, T. J. W. 2015, *The Astrophysical Journal Letters*, 814, L20, doi: [10.1088/2041-8205/814/2/L20](https://doi.org/10.1088/2041-8205/814/2/L20)
- Moustakas, J., Coil, A. L., Aird, J., et al. 2013, *The Astrophysical Journal*, 767, 50, doi: [10.1088/0004-637X/767/1/50](https://doi.org/10.1088/0004-637X/767/1/50)
- Newburgh, L. B., Addison, G. E., Amiri, M., et al. 2014, in *Society of Photo-Optical Instrumentation Engineers (SPIE) Conference Series*, Vol. 9145, *Ground-based and Airborne Telescopes V*, ed. L. M. Stepp, R. Gilmozzi, & H. J. Hall, 91454V, doi: [10.1117/12.2056962](https://doi.org/10.1117/12.2056962)
- Ng, C., Vanderlinde, K., Paradise, A., et al. 2017, arXiv e-prints, arXiv:1702.04728. <https://arxiv.org/abs/1702.04728>
- Nimmo, K., Hessels, J. W. T., Keimpema, A., et al. 2021, *Nature Astronomy*, doi: [10.1038/s41550-021-01321-3](https://doi.org/10.1038/s41550-021-01321-3)
- Niu, C.-H., Li, D., Luo, R., et al. 2021a, *The Astrophysical Journal Letters*, 909, L8, doi: [10.3847/2041-8213/abe7f0](https://doi.org/10.3847/2041-8213/abe7f0)
- Niu, C. H., Aggarwal, K., Li, D., et al. 2021b, arXiv e-prints, arXiv:2110.07418. <https://arxiv.org/abs/2110.07418>

- Ocker, S. K., Cordes, J. M., & Chatterjee, S. 2021, *The Astrophysical Journal*, 911, 102, doi: [10.3847/1538-4357/abeb6e](https://doi.org/10.3847/1538-4357/abeb6e)
- Olausen, S. A., & Kaspi, V. M. 2014, *The Astrophysical Journal Supplement Series*, 212, 6, doi: [10.1088/0067-0049/212/1/6](https://doi.org/10.1088/0067-0049/212/1/6)
- Parent, E., Chawla, P., Kaspi, V. M., et al. 2020, *The Astrophysical Journal*, 904, 92, doi: [10.3847/1538-4357/abbd6f](https://doi.org/10.3847/1538-4357/abbd6f)
- Pastor-Marazuela, I., Connor, L., van Leeuwen, J., et al. 2020, arXiv e-prints, arXiv:2012.08348. <https://arxiv.org/abs/2012.08348>
- Perera, B. B. P., DeCesar, M. E., Demorest, P. B., et al. 2019, *Monthly Notices of the Royal Astronomical Society*, 490, 4666, doi: [10.1093/mnras/stz2857](https://doi.org/10.1093/mnras/stz2857)
- Petroff, E., Hessels, J. W. T., & Lorimer, D. R. 2019, *The Astronomy and Astrophysics Review*, 27, 4, doi: [10.1007/s00159-019-0116-6](https://doi.org/10.1007/s00159-019-0116-6)
- Petroff, E., Barr, E. D., Jameson, A., et al. 2016, *Publications of the Astronomical Society of Australia*, 33, e045, doi: [10.1017/pasa.2016.35](https://doi.org/10.1017/pasa.2016.35)
- Petroff, E., Houben, L., Bannister, K., et al. 2017, arXiv e-prints, arXiv:1710.08155. <https://arxiv.org/abs/1710.08155>
- Pilia, M., Burgay, M., Possenti, A., et al. 2020, *The Astrophysical Journal Letters*, 896, L40, doi: [10.3847/2041-8213/ab96c0](https://doi.org/10.3847/2041-8213/ab96c0)
- Piro, A. L. 2016, *The Astrophysical Journal Letters*, 824, L32, doi: [10.3847/2041-8205/824/2/L32](https://doi.org/10.3847/2041-8205/824/2/L32)
- Piro, A. L., & Gaensler, B. M. 2018, *The Astrophysical Journal*, 861, 150, doi: [10.3847/1538-4357/aac9bc](https://doi.org/10.3847/1538-4357/aac9bc)

- Planck Collaboration, Ade, P. A. R., Aghanim, N., et al. 2016, *Astronomy & Astrophysics*, 594, A13, doi: [10.1051/0004-6361/201525830](https://doi.org/10.1051/0004-6361/201525830)
- Platts, E., Prochaska, J. X., & Law, C. J. 2020, *The Astrophysical Journal Letters*, 895, L49, doi: [10.3847/2041-8213/ab930a](https://doi.org/10.3847/2041-8213/ab930a)
- Platts, E., Weltman, A., Walters, A., et al. 2019, *Physics Reports*, 821, 1, doi: [10.1016/j.physrep.2019.06.003](https://doi.org/10.1016/j.physrep.2019.06.003)
- Pleunis, Z. 2020, PhD thesis, McGill University
- Pleunis, Z., Michilli, D., Bassa, C. G., et al. 2021, *The Astrophysical Journal Letters*, 911, L3, doi: [10.3847/2041-8213/abec72](https://doi.org/10.3847/2041-8213/abec72)
- Popov, S. B., & Postnov, K. A. 2013, arXiv e-prints, arXiv:1307.4924. <https://arxiv.org/abs/1307.4924>
- Posti, L., & Helmi, A. 2019, *Astronomy & Astrophysics*, 621, A56, doi: [10.1051/0004-6361/201833355](https://doi.org/10.1051/0004-6361/201833355)
- Price, D. C. 2016, arXiv e-prints, arXiv:1607.03579. <https://arxiv.org/abs/1607.03579>
- Prochaska, J. X., & Zheng, Y. 2019, *Monthly Notices of the Royal Astronomical Society*, 485, 648, doi: [10.1093/mnras/stz261](https://doi.org/10.1093/mnras/stz261)
- Qiu, H., Shannon, R. M., Farah, W., et al. 2020, *Monthly Notices of the Royal Astronomical Society*, 497, 1382, doi: [10.1093/mnras/staa1916](https://doi.org/10.1093/mnras/staa1916)
- Raby, S. 2016, *Physical Review D*, 94, 103004, doi: [10.1103/PhysRevD.94.103004](https://doi.org/10.1103/PhysRevD.94.103004)
- Rafei-Ravandi, M., Smith, K. M., Li, D., et al. 2021, arXiv e-prints, arXiv:2106.04354. <https://arxiv.org/abs/2106.04354>
- Rajwade, K. M., Mickaliger, M. B., Stappers, B. W., et al. 2020a, *Monthly Notices of the Royal Astronomical Society*, 493, 4418, doi: [10.1093/mnras/staa616](https://doi.org/10.1093/mnras/staa616)

- . 2020b, *Monthly Notices of the Royal Astronomical Society*, 495, 3551, doi: [10.1093/mnras/staa1237](https://doi.org/10.1093/mnras/staa1237)
- Ransom, S., Brazier, A., Chatterjee, S., et al. 2019, in *Bulletin of the American Astronomical Society*, Vol. 51, 195. <https://arxiv.org/abs/1908.05356>
- Ransom, S. M. 2001, PhD thesis, Harvard University
- Ravi, V. 2019, *Nature Astronomy*, 3, 928, doi: [10.1038/s41550-019-0831-y](https://doi.org/10.1038/s41550-019-0831-y)
- Ravi, V., & Loeb, A. 2019, *The Astrophysical Journal*, 874, 72, doi: [10.3847/1538-4357/ab0748](https://doi.org/10.3847/1538-4357/ab0748)
- Ravi, V., Catha, M., D'Addario, L., et al. 2019, *Nature*, 572, 352, doi: [10.1038/s41586-019-1389-7](https://doi.org/10.1038/s41586-019-1389-7)
- Remazeilles, M., Dickinson, C., Banday, A. J., Bigot-Sazy, M. A., & Ghosh, T. 2015, *Monthly Notices of the Royal Astronomical Society*, 451, 4311, doi: [10.1093/mnras/stv1274](https://doi.org/10.1093/mnras/stv1274)
- Schechter, P. 1976, *The Astrophysical Journal*, 203, 297, doi: [10.1086/154079](https://doi.org/10.1086/154079)
- Scheuer, P. A. G. 1968, *Nature*, 218, 920, doi: [10.1038/218920a0](https://doi.org/10.1038/218920a0)
- Scholz, F. W., & Stephens, M. A. 1987, *Journal of the American Statistical Association*, 82, 918, doi: [10.2307/2288805](https://doi.org/10.2307/2288805)
- Scholz, P., Spitler, L. G., Hessels, J. W. T., et al. 2016, *The Astrophysical Journal*, 833, 177, doi: [10.3847/1538-4357/833/2/177](https://doi.org/10.3847/1538-4357/833/2/177)
- Seta, A., Rodrigues, L. F. S., Federrath, C., & Hales, C. A. 2021, *The Astrophysical Journal*, 907, 2, doi: [10.3847/1538-4357/abd2bb](https://doi.org/10.3847/1538-4357/abd2bb)
- Seymour, A., Michilli, D., & Pleunis, Z. 2019, DM\_phase: Algorithm for correcting dispersion of radio signals. <http://ascl.net/1910.004>

- Shaffer, J. P. 1995, *Annual Review of Psychology*, 46, 561, doi: [10.1146/annurev.ps.46.020195.003021](https://doi.org/10.1146/annurev.ps.46.020195.003021)
- Shannon, R. M., Macquart, J. P., Bannister, K. W., et al. 2018, *Nature*, 562, 386, doi: [10.1038/s41586-018-0588-y](https://doi.org/10.1038/s41586-018-0588-y)
- Shen, S., Mo, H. J., White, S. D. M., et al. 2003, *Monthly Notices of the Royal Astronomical Society*, 343, 978, doi: [10.1046/j.1365-8711.2003.06740.x](https://doi.org/10.1046/j.1365-8711.2003.06740.x)
- Simha, S., Burchett, J. N., Prochaska, J. X., et al. 2020, *The Astrophysical Journal*, 901, 134, doi: [10.3847/1538-4357/abafc3](https://doi.org/10.3847/1538-4357/abafc3)
- Sokolowski, M., Bhat, N. D. R., Macquart, J. P., et al. 2018, *The Astrophysical Journal Letters*, 867, L12, doi: [10.3847/2041-8213/aae58d](https://doi.org/10.3847/2041-8213/aae58d)
- Spitler, L. G., Cordes, J. M., Hessels, J. W. T., et al. 2014, *The Astrophysical Journal*, 790, 101, doi: [10.1088/0004-637X/790/2/101](https://doi.org/10.1088/0004-637X/790/2/101)
- Spitler, L. G., Scholz, P., Hessels, J. W. T., et al. 2016, *Nature*, 531, 202, doi: [10.1038/nature17168](https://doi.org/10.1038/nature17168)
- Sridhar, N., Metzger, B. D., Beniamini, P., et al. 2021, *The Astrophysical Journal*, 917, 13, doi: [10.3847/1538-4357/ac0140](https://doi.org/10.3847/1538-4357/ac0140)
- Stappers, B. W., Hessels, J. W. T., Alexov, A., et al. 2011, *Astronomy & Astrophysics*, 530, A80, doi: [10.1051/0004-6361/201116681](https://doi.org/10.1051/0004-6361/201116681)
- Sun, H., Zhang, B., & Li, Z. 2015, *The Astrophysical Journal*, 812, 33, doi: [10.1088/0004-637X/812/1/33](https://doi.org/10.1088/0004-637X/812/1/33)
- Taylor, J. H. 1974, *Astronomy and Astrophysics Supplement*, 15, 367
- Tegmark, M., & Zaldarriaga, M. 2009, *Physical Review D*, 79, 083530, doi: [10.1103/PhysRevD.79.083530](https://doi.org/10.1103/PhysRevD.79.083530)

- Tendulkar, S. P., Bassa, C. G., Cordes, J. M., et al. 2017, *The Astrophysical Journal Letters*, 834, L7, doi: [10.3847/2041-8213/834/2/L7](https://doi.org/10.3847/2041-8213/834/2/L7)
- Thornton, D., Stappers, B., Bailes, M., et al. 2013, *Science*, 341, 53, doi: [10.1126/science.1236789](https://doi.org/10.1126/science.1236789)
- Tingay, S. J., Trott, C. M., Wayth, R. B., et al. 2015, *The Astronomical Journal*, 150, 199, doi: [10.1088/0004-6256/150/6/199](https://doi.org/10.1088/0004-6256/150/6/199)
- Totani, T. 2013, *Publications of the Astronomical Society of Japan*, 65, L12, doi: [10.1093/pasj/65.5.L12](https://doi.org/10.1093/pasj/65.5.L12)
- Trotter, A. S., Reichart, D. E., Egger, R. E., et al. 2017, *Monthly Notices of the Royal Astronomical Society*, 469, 1299, doi: [10.1093/mnras/stx810](https://doi.org/10.1093/mnras/stx810)
- Tumlinson, J., Peebles, M. S., & Werk, J. K. 2017, *Annual Review of Astronomy and Astrophysics*, 55, 389, doi: [10.1146/annurev-astro-091916-055240](https://doi.org/10.1146/annurev-astro-091916-055240)
- Vachaspati, T. 2008, *Physical Review Letters*, 101, 141301, doi: [10.1103/PhysRevLett.101.141301](https://doi.org/10.1103/PhysRevLett.101.141301)
- van den Bergh, S. 1999, *The Astronomy and Astrophysics Review*, 9, 273, doi: [10.1007/s001590050019](https://doi.org/10.1007/s001590050019)
- van Haarlem, M. P., Wise, M. W., Gunst, A. W., et al. 2013, *Astronomy & Astrophysics*, 556, A2, doi: [10.1051/0004-6361/201220873](https://doi.org/10.1051/0004-6361/201220873)
- van Straten, W., Demorest, P., & Osłowski, S. 2012, *Astronomical Research and Technology*, 9, 237. <https://arxiv.org/abs/1205.6276>
- Vedantham, H. K., & Phinney, E. S. 2019, *Monthly Notices of the Royal Astronomical Society*, 483, 971, doi: [10.1093/mnras/sty2948](https://doi.org/10.1093/mnras/sty2948)

- Walters, A., Weltman, A., Gaensler, B. M., Ma, Y.-Z., & Witzemann, A. 2018, *The Astrophysical Journal*, 856, 65, doi: [10.3847/1538-4357/aaaf6b](https://doi.org/10.3847/1538-4357/aaaf6b)
- Wang, J.-S., Yang, Y.-P., Wu, X.-F., Dai, Z.-G., & Wang, F.-Y. 2016, *The Astrophysical Journal Letters*, 822, L7, doi: [10.3847/2041-8205/822/1/L7](https://doi.org/10.3847/2041-8205/822/1/L7)
- Xu, J., & Han, J. L. 2015, *Research in Astronomy and Astrophysics*, 15, 1629, doi: [10.1088/1674-4527/15/10/002](https://doi.org/10.1088/1674-4527/15/10/002)
- Xu, S., & Zhang, B. 2020, *The Astrophysical Journal Letters*, 898, L48, doi: [10.3847/2041-8213/aba760](https://doi.org/10.3847/2041-8213/aba760)
- Yang, H., & Zou, Y.-C. 2020, *The Astrophysical Journal Letters*, 893, L31, doi: [10.3847/2041-8213/ab800f](https://doi.org/10.3847/2041-8213/ab800f)
- Yang, Y.-P., Luo, R., Li, Z., & Zhang, B. 2017, *The Astrophysical Journal Letters*, 839, L25, doi: [10.3847/2041-8213/aa6c2e](https://doi.org/10.3847/2041-8213/aa6c2e)
- Yao, J. M., Manchester, R. N., & Wang, N. 2017, *The Astrophysical Journal*, 835, 29, doi: [10.3847/1538-4357/835/1/29](https://doi.org/10.3847/1538-4357/835/1/29)
- Zackay, B., & Ofek, E. O. 2017, *The Astrophysical Journal*, 835, 11, doi: [10.3847/1538-4357/835/1/11](https://doi.org/10.3847/1538-4357/835/1/11)
- Zanazzi, J. J., & Lai, D. 2020, *The Astrophysical Journal Letters*, 892, L15, doi: [10.3847/2041-8213/ab7cdd](https://doi.org/10.3847/2041-8213/ab7cdd)
- Zhang, B. 2016, *The Astrophysical Journal Letters*, 827, L31, doi: [10.3847/2041-8205/827/2/L31](https://doi.org/10.3847/2041-8205/827/2/L31)
- Zhang, Y., Geng, J.-J., & Huang, Y.-F. 2018, *The Astrophysical Journal*, 858, 88, doi: [10.3847/1538-4357/aabaee](https://doi.org/10.3847/1538-4357/aabaee)

---

Zheng, Z., Ofek, E. O., Kulkarni, S. R., Neill, J. D., & Juric, M. 2014, *The Astrophysical Journal*, 797, 71, doi: [10.1088/0004-637X/797/1/71](https://doi.org/10.1088/0004-637X/797/1/71)

Zhu, W., Feng, L.-L., & Zhang, F. 2018, *The Astrophysical Journal*, 865, 147, doi: [10.3847/1538-4357/aadbb0](https://doi.org/10.3847/1538-4357/aadbb0)